# Spectroscopic studies on laser-induced plasma and surface characterization of copper in an externally applied static magnetic field at atmospheric pressure

*by*

**KHWAIRAKPAM SHANTAKUMAR SINGH**

**DEPARTMENT OF PHYSICS**

**INDIAN INSTITUTE OF TECHNOLOGY GUWAHATI**

**GUWAHATI-781039, INDIA**

**MARCH 2017**

# Spectroscopic studies on laser-induced plasma and surface characterization of copper in an externally applied static magnetic field at atmospheric pressure

*A Thesis submitted in partial fulfillment of the requirements for*

*the award of the degree of*

# DOCTOR OF PHILOSOPHY

*by*

**KHWAIRAKPAM SHANTAKUMAR SINGH**

**DEPARTMENT OF PHYSICS**

**INDIAN INSTITUTE OF TECHNOLOGY GUWAHATI**

**GUWAHATI-781039, INDIA**

**MARCH 2017**

*Dedicated to my Parents*

**Khwairakpam Shantakumar Singh**
**Roll No. 11612119**
**Department of Physics**
**Indian Institute of Technology Guwahati**
**Guwahati-781039, Assam, India**

# STATEMENT

I hereby declare that the matter embodied in this thesis is the result of investigations carried out by me at the Department of Physics, Indian Institute of Technology Guwahati, Guwahati, India, under the supervision of **Dr. Ashwini Kumar Sharma**. This thesis has not been submitted to any university/institute or elsewhere for the award of any degree, diploma or associateship.

**Date:** **Khwairakpam Shantakumar Singh**

भारतीय प्रौद्योगिकी संस्थान गुवाहाटी
**Indian Institute of Technology Guwahati**
**Department of Physics**
Guwahati-781039, Assam State, INDIA
Phone: +91 361 2582724
**Dr. Ashwini Kumar Sharma**
Associate Professor
E-mail: aksharma@iitg.ernet.in

---

Date:

# Certificate

This is to certify that work contained in the thesis entitled "**Spectroscopic studies on laser-induced plasma and surface characterization of copper in an externally applied static magnetic field at atmospheric pressure**", by **Mr Khwairakpam Shantakumar Singh** (Roll no. 11612119), a student of Department of Physics, Indian Institute of Technology Guwahati, for the award of degree of Doctor of Philosophy, has been carried out under my supervision and that the same has not been submitted elsewhere for a degree.

(Ashwini Kumar Sharma)

# *Acknowledgement*

***It would have never possible to complete my thesis without the generous and endless helping hand of many people. I am really happy to think that I am being blessed by the Almighty God who sent them close to me and I would like to bow down my head before Him. Also I would like to acknowledge each of them from the bottom of my heart.***

***First of all, I would like to extend my hearty appreciation to my thesis supervisor, Dr. Ashwini Kumar Sharma for his inspiration, constant motivation advice, precious guidance and supervision of the research. I feel lucky enough to be his Ph.D. student. I would like to acknowledge him for all his contributions of time, and ideas to make my Ph.D. experience productive and stimulating. The joy and enthusiasm he has for his research was contagious and motivational for me, even during tough times in the Ph.D. pursuit. I am also really indebted to my doctoral committee members, Dr. Malay Kumar Nandy, Prof. Alika Khare, and Dr. Shrikrishna N. Joshi for their valuable suggestions and motivation which has helped a lot to improve the research work. In particular, I am thankful to Dr. Malay Kumar Nandy for helping me to understand basic concepts related to my research. I would also like to acknowledge Prof. Alika Khare for her support to complete my thesis technically and morally. I am also thankful to Dr. Shrikrishna N. Joshi for his suggestions to improve my work on simulation.***

***I would like to extend my sincere gratitude to Prof. K. DarunKumar Singh, Department of Civil Engineering, IIT Guwahati and Mr. N. Thoiba Singh, Assistant Professor, Don Bosco University, Guwahati for introducing me to finite element method software (ANSYS). I would like to express my hearty gratitude to my maternal uncles, Dr. A Shyamkishore Singh, Assistant professor, Department of Political science, Mizoram University and Mr. A Amujao Singh for their valuable suggestions, advice, motivation, and encouragement.***

***I owe my sincere thanks to the present and former Head of the Department of Physics as well as CIF, Department of Mechanical engineering, IIT Guwahati. Also, I would like to extend my sincere thanks to Dr. S. Sarma, Mr A.C. Deka, Mr Aditya, and other staff members for their kind help with various instruments.I would like to thank IIT Guwahati for providing me financial assistance during my Ph.D. tenure through GATE fellowship.It was immense pleasure to work with my research lab members, Dr. Abu, Dr. Satchi, Dr. Poulami, Dr. Indrajeet, Partha, Gyan, Prahlad, Rahul, Eshita, Sasmita, Gobinda, Sumit, Sunderlal, and Nagendra who were always ready to assist me at any time to any extent. I would like to thank them for useful discussions, valuable suggestions, constant help to carry out the experiments, and kindness throughout my Ph.D. I am really thankful to Dr. Himanshu for valuable suggestions and motivation. I am deeply grateful to all my friends, Sandeep, Biplob, Charan, Debasish, Karthik, Priya, Sukumar, Sachidananda, Disco, my Ph.D. batch mates, seniors and juniors for their suggestions.***

***Last, but by no means the least, I would like to thank my parents as well as my family members for their love, blessings, moral support and understanding throughout my studies.***

## *Abstract*

*The objective of the present thesis is to investigate the laser ablation and laser produced plasma of copper in the absence and presence of magnetic field in air atmosphere. The optical emission spectroscopy is used to optimize the laser fluence and magnetic field for subsequent studies. The temporal evolution of copper transitions (neutral) studied showed multi-component structures. Without magnetic field and at 0.1 T the temporal profile of copper consists of two components and at higher magnetic field of 0.3 and 0.5 T, a third component is observed. The sample-to-focus distance of laser focusing lens affects the dynamical behavior of plasma in the presence of magnetic field. The optical emission enhancement is found to be maximum when the focus-to-sample distance is 5 mm. The increase in the ablated volume of laser induced craters in the presence of magnetic field is due to the increase in melt ejection as a result of increase in recoil pressure on the melted layer. The other possibility is the increase in plasma-target heat transfer which leads to further ablation. Therefore, to understand the dependence of laser ablation enhancement on the thermo-physical properties of the material, studies are reported on copper and aluminum. The increase in ablation is more pronounced in aluminum having low melting/vaporization temperature and high absorption coefficient of laser radiation. The investigation of the deposited particles on copper target shows the presence of Cu/CuO/$Cu_2O$ crystal nanoparticles. The transformation of $Cu_2O$ to CuO in the presence of magnetic field is in good agreement with X-ray diffraction, Raman, and photoluminescence studies. The laser ablation is further studied by creating the craters with higher number of laser shots in the presence of uniform and non-uniform magnetic field. The minimum size of droplets is estimated to be 0.68 μm. The droplet size increased (> 0.68 μm) in the presence of magnetic field as compared to without magnetic field. The percentage of large sized droplets increased in the presence of non-uniform magnetic field due to melt ejection and instability of liquid layer formed in the crater surface. It is attributed to an additional drift between the liquid layer and plasma which enhances Kelvin-Helmholtz instability. Finite element method is used to simulate laser heating in copper and aluminum targets using 2 dimensional heat conduction equation. The vapor pressure in the presence of magnetic field is estimated by adding magnetic pressure in the Clausius-Clayperon equation and results from this modified equation are found to be in close agreement with that obtained from the experiment. The dependence of laser ablation on thermo-physical parameters is also in good agreement with the experimental results. The ablated volume estimated experimentally is very close to the volume estimated from simulation signifying the validity of modelling used in present thesis. Therefore the reported work will be very useful to better understand the nanosecond laser ablation and laser plasma in the presence of magnetic field in air. The laser plasma with magnetic field can be used as a controllable atom source. It will be useful to improve the sensitivity in LIBS in the presence of magnetic field by increasing signal-to-noise ratio. An external magnetic field can be used to improve laser ablation and to transform the phase of copper oxide. The modeling introduced would be beneficial to understand the laser drilling and welding processes during the interaction of laser with the material.*

## *Contents*

## *List of Figures*

## *List of Tables*

## *Abbreviations*

| | |
|---|---|
| arb. unit | Arbitrary unit |
| CCD | Charge coupled device |
| DSO | Digital storage oscilloscope |
| EDX | Energy dispersive X-ray |
| EF | Enhancement factor |
| FEM | Finite element method |
| FESEM | Field emission scanning electron microscope |
| FWHM | Full width at half maximum |
| IB | Inverse Bremsstrahlung |
| IPLD | Inverse pulsed deposition |
| KH | Kelvin-Helmholtz |
| LIBS | Laser induced breakdown spectroscopy |
| LPP | Laser-produced plasma |
| LSC | Laser-supported combustion |
| LSD | Laser-supported detonation |
| LSR | Laser-supported radiation |
| LTE | Local thermodynamic equilibrium |
| LTSD | Lens-to-sample distance |
| Nd:YAG | Neodymium yttrium aluminum garnet |
| NU | non-uniform |
| NPs | Nanoparticles |
| PLD | Pulsed laser deposition |
| PMT | Photo multiplier tube |
| PL | Photoluminescence |
| OES | Optical emission spectroscopy |
| RT | Rayleigh-Taylor |
| SMB | Shifted Maxwell-Boltzmann |
| XRD | X-ray Diffraction |

## ***Symbols***

| | |
|---|---|
| $\alpha_{ab}$ | absorption coefficient |
| $\alpha_{th}$ | coefficient of thermal expansion |
| $\beta$ | ratio of plasma thermal pressure to magnetic pressure |
| $\beta_{1/2}$ | full-width at half maximum of X-ray diffraction peak |
| $\Delta\lambda_D$ | Doppler width |
| $\Delta\lambda_{1/2}$ | Full-width at half maximum |
| $\Delta E_{nm}$ | difference in energy between upper states of a transition |
| $\Delta H_{lv}$ | latent heat of vaporization |
| $\varepsilon$ | strain |
| $\theta$ | Bragg's angle |
| $\lambda$ | wavelength |
| $\mu_0$ | absolute permeability of free space |
| $\nu_p$ | Poisson ratio |
| $\pi$ | 3.14 |
| $\rho_s$ | density of solid |
| $\rho_l$ | density of liquid |
| $\rho_v$ | density of vapor |
| $\sigma_s$ | surface tension |
| $\sigma_{nm}$ | excitation cross-section |
| $\sigma_{th}$ | thermal stress |
| $\tau$ | pulse duration |
| $\tau_d$ | magnetic diffusion time |
| $\tau_{rel}$ | relaxation time |
| $a$ | size of crystallite |
| $A$ | ion broadening parameter |
| $A_{mn}$ | transition probability |
| $B$ | magnetic field |
| $C$ | specific heat |
| $C_f$ | focused laser diameter |
| $C_d$ | crater diameter |
| $D_{th}$ | thermal diffusivity |
| 2D | two dimensional |
| $D$ | diffusion coefficient |
| $d_n$ | measured inter-planar spacing of planes in crystal structure |
| $d_0$ | strain free inter-planar spacing of planes in crystal structure |
| $d$ | target surface-to-focus distance |
| $E_m$ | energy of upper state |
| $E_n$ | energy of lower state |
| $f$ | focal length of lens |
| $f_{nm}$ | oscillator strength |
| $h$ | Planck's constant |
| $h_{exp}$ | experimental ablation depth |
| $h_{th}$ | theoretical ablation depth |
| $H$ | enthalpy |
| $I_0$ | maximum laser intensity |
| $k_B$ | Boltzmann constant |
| $k_{mag}$ | thermal conductivity of plasma with $B$ |
| $k$ | thermal conductivity |
| K | kelvin |
| $L_{op}$ | optical penetration depth |
| $L_{th}$ | thermal diffusion length |
| $M$ | total ablated mass |
| $n_e$ | electron density |
| $n_i$ | ion density |
| $N_D$ | number of particles in Debye sphere |
| $P_{air}$ | air pressure |
| $P_0$ | ambient pressure |
| $P_{mag}$ | magnetic pressure |
| $P_{vap}$ | vapor pressure |
| $R$ | universal gas constant |
| $R_b$ | stopping radius |
| $R_{ref}$ | reflectivity |

| | |
|---|---|
| $R_L$ | radius of laser spot |
| $r_{RT}$ | size of particle generated due to RT instability |
| $r_{KH}$ | size of particle generated due to KH instability |
| $S_0$ | target position at $d$ = 0 |
| $S_1$ | target position at $d$ = 5 mm |
| $S_2$ | target position at $d$ = 10 mm |
| $S_{-1}$ | target position at $d$ = -5 mm |
| $S_{-2}$ | target position at $d$ = -10 mm |
| $T_e$ | electron temperature |
| $T_s$ | surface temperature |
| $T_i$ | ion temperature |
| $T_m$ | melting temperature |
| $T_v$ | vaporization temperature |
| $P_{rec}$ | recoil pressure |
| $v$ | plasma expansion velocity |
| $v_c$ | critical velocity |
| $v_e$ | velocity of electron |
| $v_t$ | tangential velocity |
| $V$ | volume of plasma plume |
| $V_d$ | plasma drift velocity |
| $w$ | electron impact parameter |
| $w_g$ | width of Gaussian function |
| $w_L$ | width of Lorentzian function |
| $Y$ | Young's modulus |
| $Z$ | partition function |
| $Z$(shock) | shock impedance |
| $\langle\bar{g}\rangle$ | Gaunt factor averaged over a Maxwellian velocity distribution |
| $\nabla p$ | pressure gradient |
| $\approx$ | approximately |

# Chapter 1

## *Introduction*

When a high power pulsed laser radiation is focused on a target, it may dissociate, excite, and/or ionize the constituent atoms of the target and eventually it is converted into plasma on further ionization by absorbing the incident laser radiation. As a result of laser-matter interaction, many kinds of processes such as emission of radiation from visible range to X-ray depending on the intensity of laser, high energy particle emission, excitation of instabilities, ablation of material, target acceleration may occur.[1] Laser ablation has been of great interest for fundamental studies and its application in pulsed laser deposition (PLD)[2–5], inverse pulsed laser deposition (IPLD)[6–8], welding and drilling[9–12], synthesis of nanoparticles (NPs)[13–19], laser cleaning,[20,21] and laser-induced breakdown spectroscopy (LIBS).[22–25] Laser ablation can change the surface morphology of a target and can bring about changes in its electrical, optical, and mechanical properties.[26] The micro- and nanostructured laser ablated surface has a wide-range of applications in industry, research, and medical science.[27]

Dynamical behaviour of laser-produced plasma (LPP) depends on the laser parameters like laser intensity, wavelength, pulse duration, repetition rate, size and shape of laser spot, and ambient gas which in turn strongly affects its application in PLD, IPLD, LIBS, synthesis of nanoparticles, etc.[28–32] Some of the frequently used techniques to study LPP plume dynamics are fast imaging method, optical emission

spectroscopy (OES), Thomson scattering, Langmuir probe, and numerical method, to name a few.[33–37]

Spectroscopic study of optical emission from LPP is known as LIBS. It was started around 1965 soon after the invention of high power laser and is still growing.[1] This spectroscopic technique has many advantages as it can be used in any type of sample (solid, liquid, and gas) and it does not require any sample preparation. It also has high spatial resolution due to small focal spot size and it can be used to analyse the sample in hostile environment and for remote detection. The sensitivity of the LIBS is dependent on the dynamical behaviour of the plasma. The condition of ambient atmosphere also affects the optical emission and plasma target interaction.[38] Owing to the dependence of LPP dynamics on ambient conditions, LPP in different ambient conditions like air, liquid, inert gas, etc. has been extensively investigated using time resolved OES.[15,39,40] The spectra of LPP at atmospheric air pressure are characterized mainly by discrete and intense peaks resulting in an increase in signal-to-noise ratio.[41]

In recent years, the studies on LPP in the presence of an external magnetic field (***B***) has attracted more attention as it gives rise to various interesting phenomena such as optical emission enhancement[42], plasma instabilities[43], astrophysical processes of stellar interiors[44], Joule's heating and plasma plume confinement.[45] It also has potential applications such as in thin film deposition[46], debris mitigation[47], nanoparticle synthesis[48], surface modification[49], etc. The increase in laser ablation and confinement of plasma in the presence of magnetic field in turn affects the characteristics of optical emission and plasma plume dynamics.[50] A few studies on the

effect of magnetic field on LPP for the practical application of LIBS are available in the literature. Rai et al. studied the LPP of solid/liquid sample in air in the presence of 0.5 T magnetic field and showed that the optical emission enhancement depends on the target material properties and laser energy.[42] The optical emission enhancement is mainly due to the confinement of plasma. It was also observed that the enhancement factor (EF) (i.e. EF is defined as the ratio of emission intensity with magnetic field to that without magnetic field) initially increased when the laser energy was increased from 10 to 50 mJ and then saturated when the laser energy increased beyond 50 mJ.[42] The saturation in line emission at higher laser energy was caused by reflection of laser radiation from the plasma, self-absorption, instability, and diffusion of particles. The enhancement was pronounced at moderate laser energy and the EF of 1.5 – 2 was achieved. Li et al. also observed improvement in EF of atomic/ionic transitions of Cu plasma in air at moderate laser energy of 30 mJ when the laser energy was increased from 13 to 85 mJ in the presence of magnetic field.[51] When the plasma is confined into a small region, the rate of collisional excitation and recombination gets larger and hence the emission intensity is increased. The optical emission from magnetically and spatially confined LPP has shown more intensity enhancement.[52] In the presence of magnetic field, Shen et al. studied the LPP of Al, Cu, and Co in air at different laser fluences. It was observed that the intensity EF for atomic lines of Al and Cu was in the range of 2-8 whereas Co atomic line showed a decrease in EF. The change in intensity is due to the change in effective density of the plasma in the presence of magnetic field and it depends on the material as well as its excitation properties.[53] Kim et al. investigated the effect of variation of laser energy on LPP of Cu in air and

demonstrated that the enhancement of LIBS signal of Cu plasma with magnetic field occured at 30 mJ.[54]

The behavior of LPP of different materials in the presence of magnetic field in different ambient gases (helium and argon)/vacuum has been studied in terms of plume confinement, diamagnetic effect, intensity enhancement, increase in electron temperature, and density.[17–19] The influence of the magnetic field (0.45 T) on LPP in vacuum has been investigated using time-of-flight OES and results showed temporally broadened atomic lines while ionic line showed more confinement in the presence of magnetic field at laser fluence higher than/equal to 24 $Jcm^{-2}$.[55] Owing to diamagnetic behavior of LPP in the presence of magnetic field, the temporal profiles of plasma species at 6 mm from the target were found to be independent of ambient (argon gas at low pressure ) conditions.[57] The dynamics of the laser-produced Cu plasma with non-uniform magnetic field (NU) in gas ambient has been studied using fast imaging and OES and showed cluster formation, stagnation, and oscillatory rotation of the plasma plume.[43,58,59] The investigation of LPP in the presence of NU magnetic field at low air pressure (0.1 mTorr) ambient has also been reported earlier.[60] The rotating Cu plasmoid in helium and argon gases has been studied using OES and fast photography. The experiments showed the Rayleigh-Taylor (RT) instability at the interface between the plasma and NU magnetic field (0.5 T at poles and 0.35 T in the middle of the poles of magnet).[43] RT instability was also observed in laser-produced carbon plasma at low air pressure (5 mTorr and 100 mTorr) and vacuum in the presence of NU magnetic field.[44,60] Patel et al. investigated the behavior of brass plasmoid in the NU magnetic field at different air pressures ($10^{-4}$

mbar, $10^{-1}$ mbar, and 1 atm.) and observed the splitting of the plume at lower pressure of $10^{-1}$ mbar.[59] Mostovych et al. reported the collimation and instability of LPP in the presence of variable transverse magnetic field (0 – 1T).[61] However, limited studies on LLP in the presence of magnetic field and air at atmospheric pressure are available in the literature.

Since LPP is highly transient, the temporal evolution of plasma has been investigated using time-resolved OES.[62–65] However, the effect of variation of magnetic field on temporal evolution is not well documented. Joshi et al. studied the temporal evolution of LPP in vacuum as a function of transverse magnetic field using temporal spectroscopic technique and observed that as the magnetic field was increased from 0 to 0.08 T, the intensity of atomic Li line initially increased and subsequently decreased at higher magnetic field of 0.3 T.[66] The effect of the external transverse variable magnetic field (0 - 0.2 T) on the laser-blow-off plasma plume emission at low air pressure as well as ambient gas condition has been studied. The intensity enhancement of atomic lines which varies with the magnetic field was discussed by invoking various atomic processes like electron-impact excitation, recombination, and diffusion of the ambient gas in the plasma plume in collisional and hydrodynamic regime.[67,68] It also reported the observation of different multi-component structures in the temporal atomic line profile with magnetic field. Using fast imaging technique the expansion and confinement of the LPP of Al, Cu, and brass in air was investigated by varying the magnetic field from 0 to 0.8 T. The recorded plasma images showed that the expansion of plasma plume along the magnetic field increased with magnetic field.[69] Similar phenomenon was also observed in LPP of glass in the presence of transverse variable magnetic field.[70]

Since the plasma evolves with space, the spatially-resolved optical emission spectroscopic study is employed to extract the quantitative information of plasma parameters of the localized region of LPP.[71] The optical emission of LPP in the presence of an external magnetic field investigated using optical fiber showed the intensity enhancement which is attributed to an increase in effective plasma density due to the magnetic confinement of plasma.[22] This spectroscopic study is useful to optimize the distance from target to get better sensitivity in LIBS for elemental composition analysis.[22] In the literature, several authors reported spatially-resolved optical emission spectroscopic study using optical fiber [24, 37, 72–74,] and observed a decrease in spectral line intensity, electron density, and temperature with distance from the target. This is attributed to the adiabatic expansion of plasma. Aguilera et al. studied LPP by spatially-resolved spectroscopy of atomic and ionic emissions and observed that the electron temperature determined locally was found to be identical to ionic temperature. However, in the case of integrated emission measurement they observed difference between the electronic and ionic temperatures which is due to the population-averages of the local electronic temperature.[76] Chen et al. studied the spatial evolution of laser induced SiC plasma in vacuum and estimated the dimension of the core and tail of the plasma.[77] The study on spatial evolution also helps to determine target-substrate distance in PLD to reduce debris or splashing.[78] Hermann et al. reported on PLD of TiN using spatially-resolved optical emission spectra collected with fiber and made various conclusions concerning vaporization, plasma formation and propagation, and the creation of reactive species leading to TiN formation.[4]

Laser ablation, laser material processing, and optical emission from LPP is also dependent on the geometrical factor like lens-to-sample distance (LTSD). The effect of LTSD on LPP of metals in air has been studied using spherical and cylindrical lenses indicating that the atomic emission intensity, electron temperature, and ablation mass depends on LTSD.[79] Aguilera et al. studied the effect of focusing distance on LPP in air and observed quadratic dependence of line intensities on laser energy.[80] The effect of LTSD on LPP during laser processing has shown that the reduction in intensity at laser tight focusing condition is due to saturation effect.[81] The spatial behavior of laser-produced iron plasma in air and argon ambient with different LTSD has been investigated and observed the change in intensity with LTSD attributed to the plasma shielding effect.[82] Chen et al. investigated the role of LTSD on laser induced damage on zinc target and observed a significant decrease in the damaged region when LTSD increased. It was also reported that the electron temperature follows the exponential growth with LTSD.[83] However, these studies are in the absence of magnetic field.

In recent years, laser ablation has been widely used in material science especially for depositing thin film/synthesis of nanoparticles using PLD/IPLD.[84] LPP parameters affect the quality of thin film deposited via PLD.[3,4,78,85,86] The synthesis and characterization of Cu oxide nanoparticles thin film using PLD (in air ambient/other gas/vacuum) have been studied extensively.[2,5,87] Brailovsky et al. showed that the formation of melt droplets is mainly due to the melt ejection. The other possibilities are RT and Kelvin-Helmholtz (KH) instabilities.[88] In IPLD, the backward motion of the ablated mass is utilized to deposit thin films on the target itself or substrate

mounted on the target and it solely depends on the condition of the ambient atmosphere.[48] The thin films deposited using IPLD contain less micron-sized particulates and exhibited dense structure compared with that deposited by PLD, especially, at high ambient pressure.[89] Pereira et al. studied the characterization of plasma dynamics and surface nanostructuring of target in air at atmospheric pressure and showed that the kinetic energy and density of plasma are the two key factors which control the nanoparticle formation on the target.[90]

The external magnetic field has been used to improve the quality of PLD thin film [91] and to control the nanoparticle size IPLD as well.[48] The magnetic field is also used to mitigate debris in PLD and extreme ultra violet lithography.[46,92] Musaev et al. investigated the laser ablation of gold in liquid ambient and observed the formation of short nanowires in the presence of magnetic field. It is attributed to the formation of aggregates of dispersed nanoparticles due to confinement of plasma.[93] The study on IPLD of Cu cluster in the presence of NU magnetic field and ambient gas (argon/helium) showed the dependence of nanoparticles shape on the ambient gas. It is due to the difference in backscattering of particles as a result of increase in collisions, temperature, and confinement of plasma in the presence of magnetic field and argon/helium ambient.[18] The effect of ambient gas pressure on the surface morphology of the deposited material has also been studied extensively[18,85] but the effect of magnetic field on IPLD of Cu in atmospheric air is not well documented. Since the IPLD depends on kinetic energy and plasma density, the understanding of plasma parameters in LPP is essential. The magnetic field can also control the quality and efficiency of welding and drilling.[49,94] The increase in depth and relatively less

residual in magnetic field assisted laser drilling is more likely due to an increase in the heat transfer from the magnetically confined plasma to the target.[49] By applying an external magnetic field, the aspect ratio of micromachining can be enhanced. The reason is that the magnetic field squeezes LPP and brings it closer to the target resulting in deeper drilling depth and hence the aspect ratio.[95] It is attributed to the magnetic confinement of the plasma.[96] Recent investigations showed that the presence of electromagnetic field results in small diameter, smooth surface, and less defects in the nanosecond laser drilling. Multi-shock effect which causes drilling defect can be minimized by the application of an external electromagnetic field.[97] In the presence of magnetic field the penetration depth was found to increase during $CO_2$ laser drilling. However, the drilling depth decreased at higher magnetic field.[94] Chao et al.[98] studied the magnetic field assisted laser percussion drilling and showed that the penetration depth can be increased by 87.7 %. The static magnetic field can improve the drilling efficiency of highly reflective metals.[99] It therefore emerges from these discussions that the morphological and spectroscopic characterization of laser-ablated Cu in air at atmospheric pressure in the presence of uniform/NU magnetic field is not reported in the literature.

The physical processes involved in laser ablation remain quite unclear though its application geared up in different fields. To get an exact solution using an analytical method of this phenomenon with the complex boundary condition is quite difficult. Finite element method (FEM) is a numerical method which is useful to solve a problem with the complex boundary conditions. The finite element simulation based on 2D heat conduction was investigated to predict the evolution of surface

temperature and the depth of the laser irradiated target like TiC, Si, $Al_2O_3$.[100,101] It was also observed that the simulated results based on temperature dependent thermo-physical parameters are very close to the experimentally measured ablation depth. In the light of above discussions, it is understood that similar studies for Cu and Al are not well documented so far. Also the finite element modeling to simulate laser ablation in the presence of magnetic field is not reported in the literature.

Laser ablation several of metals has been investigated for various applications. Amongst the various targets investigated in LPP, copper is one of the most exploited elements in various fields of industry and technology. Therefore, diagnostic techniques for this element are of particular interest in industrial laboratories. In recent years, the usage of drilled Cu foil is favored to design multi-level printed circuit boards (PCB) in which the connection of PCB between conducting layers is made by drilled holes or microvias.[11,102] Al is also used as electrodes in microsystems technology for biotechnology applications.[9] Al with micro-holes created by pulsed laser ablation enhances the light absorption that can be used in solar cell.[103] The micro-hole drilling by laser has many advantages including smaller size, faster drilling rate and high aspect ratio. The oxygen in air gets oxidized to form copper oxide nanoparticles/microparticles of different size. The copper oxide nanoparticles/microparticles of different size and shapes are used as sensors, catalysts, light emitting diode, anti-fungal and bacterial activities, and solar cells.[104,105]

The present thesis deals with the effect of static magnetic field on laser ablation of Cu and its LPP in air at atmospheric pressure. The LPP of Cu was studied experimentally using OES. The LPP of Cu plasma was investigated using time-

integrated OES by varying the laser fluence and magnetic field to obtain optimized laser fluence and the magnetic field for subsequent studies. Since the plasma is highly transient the temporal evolution of plasma was also studied by varying the magnetic field to better understand the dynamical behaviour of LPP in the magnetic field. It evolves not only with time but it also changes with space. Therefore, the spatially-resolved OES was employed to study the spatial evolution of plasma in the absence and presence of magnetic field. The lens focusing distance was also varied with respect to the target to study the dependence of LPP on LTSD in the presence of magnetic field. The effect of uniform magnetic field on laser ablation and the particles deposited on the Cu target was investigated. The craters were generated on Cu and Al targets in the presence and absence of magnetic field to study the dependence of laser ablation on thermo-physical parameters. The effect of magnetic field on laser ablation of Cu and its plasma was also extended by the application of NU magnetic field. The numerical method is a useful tool to model a complex process. Based on heat 2D conduction, the laser ablation was simulated using FEM to estimate the ablation depth generated due to vaporization/melt ejection. The simulation with the temperature dependent parameters of Cu/Al in the absence and presence of magnetic field leads to more realistic depth/volume which is not well documented. In the present thesis, the temperature dependent enthalpy is used to take into account the effect of phase transition during the laser ablation. The vaporization rate was estimated from the vapour pressure and target surface temperature. The melt ejection rate was calculated from the piston effect caused due to the recoil pressure of the ablated mass. The temporal evolution of vapour pressure is given by Clausius-Clapeyron equation. In the present thesis, the Clausius-Clapeyron equation was modified by introducing a

magnetic pressure term to calculate the vapour pressure in the presence of magnetic field. The ablation rate due to vaporization/melt ejection was compared with the experimentally measured values. The plasma is decelerated significantly in the presence of magnetic field and ideally it stops at a distance called stopping radius. The stopping radius was estimated by taking into account the effect of air pressure at different focusing distances.

The entire thesis is planned into seven chapters as follows. Chapter 1 gives a brief general introduction on laser matter-interaction and literature survey on the LPP in magnetic field. For studies on laser ablation and its subsequent generation of LPP, a better understanding of the basic physical process in plasma is one of the main requisites. In the present work, the OES was employed to diagnose the LPP in the absence and presence of magnetic field. Since the plasma involves various complex processes, the numerical method is widely used to model plasma processes. FEM is one of the numerical methods which can be used to solve the problem even in a complex geometry. Therefore, the ANSYS software based on FEM has been used to simulate laser ablation and physical processes in the plasma. The FEM (ANSYS) was employed to simulate laser ablation in this present thesis. The basic physical processes in LPP in the presence of magnetic field, experimental setup, and FEM are discussed in chapter 2. In the light of earlier discussions, it is understood that most of the previous studies on effect of magnetic field on plasma are mainly at a fixed laser fluence and magnetic field. In the present thesis, laser produced Cu plasma was studied by varying the laser fluence and magnetic field. The laser fluence and magnetic field at which the intensity of optical emission was maximum were fixed for

subsequent studies. Chapter 3 discusses the effect of variation of laser fluence and magnetic field on laser produced Cu plasma. Since, the plasma evolves with time and space, the temporal and spatial evolution of LPP was studied in the absence and presence of magnetic field. LPP is also significantly affected by LTSD and, therefore, the effect of LTSD on LPP in the presence of magnetic field was also investigated. The detailed results and discussion on studies on temporal and spatial evolution and the effect of lens focusing distance on Cu plasma in the presence of magnetic field is presented in chapter 4. The laser ablation is used to synthesize nanoparticles using PLD/IPLD technique for various applications. Both techniques are solely dependent on ambient condition. The presence of high pressure air ambient and magnetic field affects the dynamical behavior and eventually the deposited particles on the target surface. In order to study the effect of magnetic field on laser ablation and deposited particles on Cu target, the laser ablated target was characterized using surface characterization techniques discussed in chapter 2. The results and interpretation on the effect of magnetic field on laser ablation and deposited particles are described in chapter 5. FEM was used to simulate the evolution of surface temperature and the estimation of vapor pressure in the present thesis. The enhancement in laser ablation in the presence of magnetic field observed experimentally was justified by invoking the role of recoil pressure in melt ejection in the numerical studies. Chapter 6 deals with the numerical studies on the effect of magnetic field on laser ablation. The thesis is concluded in chapter 7.

# Chapter 2

## *Basic Physical Processes, Experimental Setup, and Finite Element Method*

Chapter 1 presented a brief account of the generation of LPP in the absence and presence of magnetic field. In this chapter, the basic physical processes and parameters used in plasma diagnostics are discussed. The experimental setup used for the experiments is discussed in detail. The basic FEM and its procedure to simulate laser heating are also presented at the end of this chapter.

### 2.1. Basic physical processes in plasma

#### 2.1.1. *Laser-matter interaction and plasma formation*

The removal of a portion of material by focusing a high power laser beam with the laser fluence greater than the ablation threshold is called laser ablation. The laser energy is absorbed by free electrons of the metal through inverse Bremsstrahlung (IB) process. The electron-electron and electron-phonon interaction time[84], respectively, can be estimated from $\tau_{ee} \approx 10^{-15}\left(\frac{\varepsilon_F}{\varepsilon-\varepsilon_F}\right)$ and $\tau_{eL} \approx \frac{\gamma_e T_e}{g_{ep}}$, where $\varepsilon$ is laser photon energy (2.3 eV for 532 nm laser wavelength), $\varepsilon_F$ is the Fermi level (7 eV for Cu), $\gamma_e$ is the electron specific heat constant (96.6 $Jm^{-3}K^{-2}$), $T_e$ is the electron temperature, and $g_{ep}$ is the electron-phonon coupling constant ($10^{17}$ $W/m^3K$ for Cu). Therefore, the electron-electron interaction time inside the metal is around 2.2 fs while that of the electron-phonon interaction is 3.9 ps. The laser pulse width is comparatively longer as compared with the time scale of interaction taking place inside the material. For nanosecond (ns) pulse laser-metal interaction, thermalization occurs within the pulse

duration through electron-electron collision and electron-lattice collision and subsequently their dynamics coincides (i.e. $T_e = T_L = T$, $T_L$ is temperature of lattice).[84] The thermal diffusion length of target is related to the thermal diffusivity by[17]

$$L_{th} = 2(D_{th}\tau)^{\frac{1}{2}} \tag{2.1}$$

where $D_{th}$ is the thermal diffusivity of the target and $\tau$ is the laser pulse duration. The heat generated on the target surface during laser pulse is confined within the thermal diffusion length ($L_{th}$). If the temperature $T$ is higher than the vaporization temperature, a part of the target gets vaporized. The free electrons present in the target vapour absorb incoming laser radiation through IB process when they collide with heavy particles, atoms and ions. The IB absorption coefficient is given by[1]

$$\alpha_{IB} = \left[\sigma n_e n_0 + \left(4e^6\lambda^3 n_e Z^2 n_i / 3hc^4 m_e\right)\times\left(2\pi / 3m_e k_B T_e\right)^{1/2}\right] \times\left[1-\exp\left(-hc / \lambda k_B T_e\right)\right] \tag{2.2}$$

where $\sigma$ is the photon absorption cross section by an electron during the collision with atoms, $c$ is the speed of light, $h$ is Planck's constant, $k_B$ is Boltzmann constant, and $Z$ is the charge on ion. $n_e$, $n_{0,}$ and $n_i$ are the density of electrons, atoms, and ions, respectively. The electrons with sufficient energy collide with atoms or molecules and further ionization occurs. As a result of this cascade breakdown, the electron concentration increases exponentially with time. The other possibility is multi-photon ionization in which an atom absorbs a sufficient number of photons simultaneously and causes its ionization. Eventually the generation of plasma occurs if the laser intensity is higher than the threshold intensity ($\approx 10^8$ W/cm$^{-2}$).

### 2.1.2. *Expansion of plasma*

The plasma expands isothermally during the laser pulse followed by adiabatic expansion after the termination of the laser pulse. At a supersonic velocity, the plasma expands normal to the target surface in an ambient gas or vacuum. The interaction between the hot expanding plasma and ambient is mainly due to two mechanisms: (i) the high pressure expanding plasma compresses the surrounding ambient gas and generates shock wave and (ii) the transfer of energy to ambient by the combination of thermal conduction, radiative transfer, and heating by shock wave. The laser ablation and its subsequent plasma evolution is a very complex process. It depends on the laser parameters like laser intensity, wavelength, pulse duration, repetition rate, and laser spot size. It is also dependent on the thermo-physical properties of the target and the nature of the ambient gas. The extensively used ambient gases include helium, argon, air, oxygen, nitrogen, etc.[58,106,107]

During the initial fraction of ns laser pulse, the vaporization and ionization occurs. The rest of the laser pulse is absorbed by vapour and expanding plasma plume. This absorption of laser in the plasma induces three different types of waves[1] due to different mechanisms of propagation of the absorbing plasma plume front into the ambient gas. These waves are strongly dependent on the laser intensity. These waves are (i) laser-supported combustion (LSC) wave (ii) laser-supported detonation (LSD) wave, and (iii) laser-supported radiation (LSR) wave. LSC is produced at low laser intensity and it comprises of a precursor shock which is separated from the absorption zone and the plasma. The shock wave leads to an increase in ambient gas density, temperature, and pressure. However, the shock edges are transparent to the

incident laser radiation. The front edge of the plasma expanding in an ambient and the laser absorption region propagates into the shocked gas resulting in LSC. The heat conduction and radiative transfer are the primary propagation mechanisms from hot plasma to the high pressure gas in the shock wave. The precursor shock is sufficiently strong at the intermediate laser intensity resulting in shocked gas hot enough to initiate the absorption of laser radiation. It does not require the additional heating by energy transport from the plasma. The laser absorption zone follows behind the shock wave and propagates at the same velocity. The propagation of this wave is entirely due to the absorption of laser energy and this regime is the LSD. At high laser intensity, since the plasma is so hot, the ambient gas is heated to a temperature at which the absorption of laser begins. The laser absorption occurs before the arrival of the shock wave. If this regime is considered in the ideal gas, laser absorption begins without any change in the density, and the pressure profile is mainly generated from the strong local heating of the gas rather than a propagating shock wave. The LSR wave velocity increases much more rapidly with laser intensity compared with the LSC and LSD waves.

When the plasma is generated by focusing a high power laser, it induces shock wave in the target as well as in the surrounding medium. It has been reported that the impulse of shock wave of plasma on the irradiated target in the presence of confined geometry (i.e. spatial confinement by transparent medium) is higher and the duration of shock impulse is longer.[108] The plasma pressure generated in air ambient can be calculated using Hugoniot relation[108]

$$P(kbar) = 0.1\left[\frac{1}{5}\left(Z(shock)I_0\right)\right]^{1/2} \qquad (2.3)$$

where $Z$ (shock) is the shock-impedance of the target-ambient system in (g/cm$^2$ s) and $I_0$ (GW/cm$^2$ ) is the incident laser intensity. The shock impedance of the target ambient-system is given by $\frac{2}{Z(shock)} = \sum_i \frac{1}{Z_i}$ , where $Z_i$(shock), $i$ = 1, 2 is the shock impedance of each material (target and confining layer). The shock impedance $Z_i$(shock) is equal to the shock velocity times the density of the material.

### 2.1.3. *Spectral emission from plasma*

The emission spectrum of LPP is mostly composed of continuum emission near the target surface where the electron density and temperature is very high. The continuum radiation is emitted by the LPP as a result of free-free and free-bound transitions. Free-free transitions are Bremsstrahlung emissions caused due to the interaction of free electrons with ions. In free-bound transition, a free electron is combined with an ion. As the plasma expands from the target, the electron temperature and density decreases and eventually the emission is dominated by the atomic lines. The line emission is due to the transitions of atom from an excited energy state to a lower excited state/ground state. Study of optical emission from the LPP gives the characteristic information of LPP and target. Various atomic processes that take place in the plasma are shown in Fig. 2.1. The optical emission strongly depends on these processes. The electron-impact excitation rate of the metals is not easily available in the literature. The electron impact excitation rate of atomic transition can be obtained from the collisional cross-section using the relation[109] $R_{nm} = n_e \langle \sigma_{nm} v_e \rangle$, where $\sigma_{nm}$ and $v_e$ are semi-empirical relation of electron impact excitation cross section for optically allowed transitions, and electron velocity, respectively. The excitation rate co-efficient $<\sigma_{nm} v_e>$ is given by[110]

$$\langle \sigma_{nm} v_e \rangle = 1.60 \times 10^{-5} \frac{f_{nm} \langle \bar{g} \rangle}{\Delta E_{mn} (k_B T_e)^{1/2}} e^{-\Delta E_{mn}/k_B T_e} cm^3 s^{-1} \qquad (2.4)$$

where $f_{nm}$ is the absorption oscillator strength and where $\langle \bar{g} \rangle$ is the Gaunt factor averaged over a Maxwellian velocity distribution.

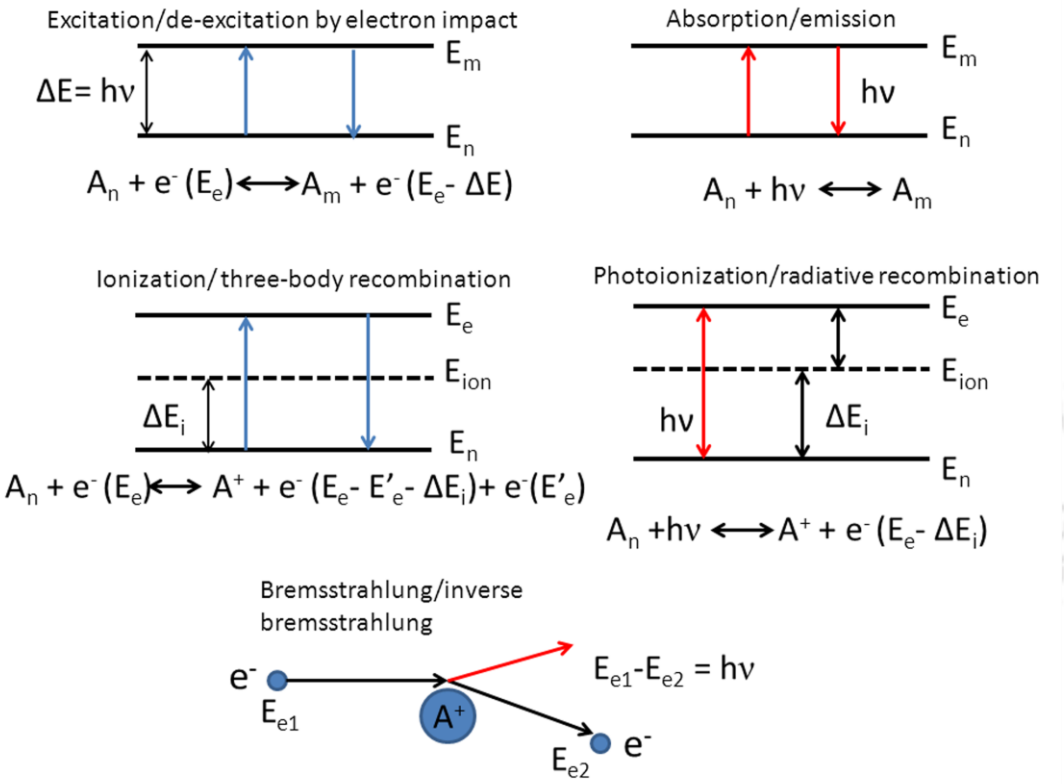


**Fig. 2.1.** Simplified representation of atomic processes in LPP.[29]

The size, expansion speed, stability, and emission properties of the plasma strongly depend on the ambient surrounding the plasma. In vacuum/low pressure ambient condition the plasma expands linearly.[111] At high ambient pressure, the plasma expansion follows the drag model whereas at moderate pressure its expansion follows the shock model.[34] The ambient gas attenuates laser energy reaching the target due to the breakdown of ambient gas. However, if the laser intensity is less than

the breakdown threshold of the ambient gas, it increases the intensity of plasma emission by confining the expanding plasma plume resulting in signal-to-noise ratio. In the presence of ambient gas the collisional excitation of an atom or ion increases as a result of confinement of the plasma by an ambient gas. The properties of surface morphology of the target generated due to the laser ablation also depend on the amount of mass backscattered which in turn depends on the ambient conditions.[58]

### 2.1.4. *Particle formation by ablation*

The particle formation occurs from direct laser ablation, condensed vapour, and melted layer ejection. The total ablated mass is not excited vapour and a significant quantity of the ablated mass is in the form of particles. The ablated particles do not contribute in LIBS signal unless these can be re-atomized and excited by LPP plume itself. [1] As the plasma expands, the temperature of plasma is reduced resulting in ion-electron recombination. When the ablated plasma plume cools down to the boiling point of ablated target, the atoms begin to condense and generate nanoparticles. The particles are also generated from the ejection of molten layer due to the recoil pressure of ablated mass exerted on the liquid layer. The melt ejection and instability of molten layer generates the micro-sized particles/droplets.[112] Depending on ambient conditions, a significant amount of ablated mass gets back-scattered and deposits on the target itself. This phenomenon is known as IPLD. The thin film deposited using IPLD shows less content of large micron-sized particulates and exhibits dense structure especially at high ambient pressure.[58]

The particles/droplets formed can be analyzed on the basis of the discussion by Kelly and Rothenberg[113] and the vapor pressure relation discussed in section 2.3.3.[114]

The surface droplets are formed when the laser pulse interacts with the target. These droplets are accelerated from the liquid layer during each laser pulse due to the volume change in melting, subsequent thermal expansion of the liquid and radial motion of the melted liquid. The separation of the droplets from the melted liquid surface is opposed by a force $f_s = 8\pi r\gamma$, where $r$ is the droplet (spherical shape) radius and $\gamma$ the liquid surface energy.[113] Therefore, the droplets are expelled out after a sufficient number of laser pulses when the total momentum taken away by the droplet from the liquid surface is greater than $f_s\Delta t$ i.e. $\left(\frac{4}{3}\pi r^3\rho_l\right)\left(\frac{\Delta L}{\Delta t}\right) > \left(8\pi r\gamma\right)\Delta t$, where $\Delta L = 2r\alpha\Delta T + 2r\left(\rho_s - \rho_l\right)/3\rho_s$, $\rho_s$ is the density of the solid, $\rho_l$ is the density of liquid, $\Delta T$ is the difference between melting temperature and maximum surface temperature, and $\Delta t$ is the difference between pulse duration and time at which surface temperature reaches the melting point. From the above relation, the minimum droplet size that can be expelled out is given by

$$r > \left[3\gamma\left(\Delta t\right)^2 / \left(\rho_l\alpha_{th}\Delta T + \rho_l\left(\rho_s - \rho_l\right)/3\rho_s\right)\right]^{1/3} \qquad (2.5)$$

As mentioned above, instability of melted layer is also a process which generates large size of particles/droplets. KH instability is excited when the two different density fluids have relative tangential velocity.[115] In laser ablation, it is excited mainly by the lateral expansion of plasma and the motion of liquid layer due to recoil pressure. The recoil pressure of ablated mass destabilizes the liquid layer while the surface tension, viscosity, and gravity tend to stabilize the same layer. Therefore, unstable perturbation grows in the liquid layer if the tangential velocity ($v_t$) exceeds some critical velocity ($v_c$)[116],

$$v_t > v_c \approx \left( \frac{4\sigma_s g \rho_l}{\rho_v^2} \right)^{1/4} \tag{2.6}$$

where $\sigma_s$ is the surface tension, $\rho_l$ is the density of liquid, $\rho_v$ is the density of vapor, and $g$ is the acceleration due to gravity. Here the mass density of the liquid is higher than that of vapor. The tangential velocity of the liquid can be determined by considering piston effect,[117]

$$v_t = \left( \frac{2\Delta P}{\rho_l} \right)^{1/2} \tag{2.7}$$

where $\Delta P = P_{vap} - P_0$, $P_{vap}$ = vapour pressure and $P_0$ = ambient pressure. The droplet or particle size produced by KH instability is approximately given by[116]

$$r_{KH} \approx \frac{3\sigma_s}{P_{rec}} \tag{2.8}$$

where $P_{rec}$ is recoil pressure equal to $0.54P_{vap}$. RT instability which assists in the formation of droplets in laser ablation arises at the interfaces between fluids (liquids or gases) of different densities that are superimposed over one another and which are in an external field (gravity, centrifugal forces, etc.). The external force is directed from the high density fluid towards the fluid of low density. RT instability at the crater boundary produces large sized particles.[118] The size of particle generated by RT instability is given by[116]

$$r_{RT} \approx 3\left( \frac{\sigma_s}{g_{RT}\rho_l} \right)^{1/2} \tag{2.9}$$

where $g_{RT}$ is the acceleration due to RT instability which gives rise by recoil pressure, thermal expansion, and different densities between vapor and liquid layer. The instability growth rate $g_{RT}$ due to vapor pressure is given by[116]

$$g_{RT} = \frac{k v_t T_v}{R_L{}^2 \Delta H_{lv}} \qquad (2.10)$$

where $k$ is thermal conductivity, $T_v$ is the vaporization temperature, $R_L$ is the laser spot radius, and $\Delta H_{lv}$ is the latent heat of vaporization.

### 2.1.5. *Local thermodynamic equilibrium*

In local thermodynamic equilibrium (LTE) the collision processes determines the distribution of electron population densities among the energy states. The collisional processes occur in a very short time and the distribution responds instantaneously to any change in the plasma condition. Each forward process is followed by its inverse process and occurs at equal rate by detailed balance. Therefore, the distribution of electron population densities of energy states is the same as it would be in a system in complete equilibrium. In this condition, it is considered that the plasma has a single temperature $T_i = T_e$. However, the plasma density and temperature vary in time and space, therefore, the distribution of population densities at any instant of time and space entirely depends on the local values of density and temperature of the plasma. The equilibrium condition is possible locally and for specific time segment. In order to justify plasma in LTE using McWhiter's criterion[119]

$$n_e \geq 1.6 \times 10^{12} T_e^{\frac{1}{2}} (\Delta E_{mn})^3 \qquad (2.11)$$

where $T_e$ is in kelvin and $\Delta E_{mn}$ in eV is the difference in energy between the states which are expected in LTE, the lower limit of the electron density ($n_e$) is calculated. To validate the LTE condition strictly, the transition with largest $\Delta E_{mn}$ must satisfy the above relation and the upper level of the transition should be close to ground state. The more precise condition obtained with quantum mechanical correction is given by the relation[109] $n_e > \frac{2.55\times10^{11}}{\langle \bar{g} \rangle} T_e^{1/2} (\Delta E_{mn})^3$. The McWhiter's condition is necessary but not sufficient. Since the plasma is transient, the electron density varies with time and evolves spatially as discussed above. If the variation of electron density is sufficiently slow, the above conditions are safely applicable to verify the LTE of plasma. However, if the evolution of plasma is too fast, the atoms and electrons would be unable to get time to attain LTE. The plasma is strictly in LTE if the above two conditions are satisfied and the relaxation time $\tau_{rel}$ is shorter than the time of variation of plasma parameters[120] i.e.

$$\frac{n_e(t+\tau_{rel})-n_e(t)}{n_e(t)} < 1; \frac{T_e(t+\tau_{rel})-T_e(t)}{T_e(t)} < 1 \qquad (2.12)$$

where the $\tau_{rel}$ of the plasma is given by[121] $\tau_{rel} = \frac{6.3\times10^4}{\langle \bar{g} \rangle f_{mn} n_e} \Delta E_{mn} (k_B T_e)^{1/2} \exp(\Delta E_{mn} / k_B T_e)$.

### 2.1.6. *Plasma diagnostics*

The factors which mainly influence the light emission by plasma are the temperature of plasma, density of the radiating species (i.e. atoms and ions), and electron density. The density of the radiating species depends on the total ablated mass, plasma temperature, and degree of the excitation and/or ionization of LPP. The ablated mass depends on the absorption of laser by the target, laser fluence, and the

shielding of plasma which in turn depends on the electron density of LPP. Therefore, for the better understanding of the atomic processes such as dissociation-atomization, excitation, and ionization occurring in LPP, the knowledge of plasma temperature and density is vital. This is also equally important to optimize the experimental parameters for the quantitative use of LIBS. The optical emission spectroscopic method generally known as LIBS can be employed to determine the electron temperature and density of LPP. LIBS is one of the widely used plasma diagnostic techniques. It has many advantages. The main advantage is that it can be used with the sample in any state of matter (solid, liquid, gas), no sample preparation is required, and the quantity of sample is also not restricted. One of the important limitations of LIBS is the sensitivity of the signal. Some methods frequently employed to enhance the sensitivity of LIBS are purging the ambient gas, oblique incidence of laser, double pulse excitation, and the application of magnetic field.[42,79,122,123]

**(i)** ***Electron temperature***

If LPP is in LTE, the intensity of the spectral line is related to the population in the excited level by the relation[37] $I_{mn} = \frac{hc}{4\pi\lambda_{mn}} \frac{n_n g_m A_{mn}}{Z} \exp\left(-\frac{E_m}{k_B T_e}\right)$, where $\lambda_{mn}$, $A_{mn}$, $g_m$, and $E_m$ are, respectively, wavelength, the transition probability, statistical weight factor, and the energy of the excited state; $n_n$, and $Z$ are total number density and the partition function, respectively. These parameters are available in the literature.[124] Thus, the two main factors influencing the intensity of the emitted spectral line are number density and the plasma temperature. After rearranging above equation,

$$\ln\left(\frac{I_{mn}\lambda_{mn}}{A_{mn}g_{mn}}\right) = \ln\left(\frac{n_n hc}{Z}\right) - \left(\frac{E_m}{k_B T_e}\right) \qquad (2.13)$$

if $\ln\left(\frac{I_{mn}\lambda_{mn}}{A_{mn}g_{mn}}\right)$ is plotted against $E_m$, we get a straight line whose slope is $-1/k_B T_e$. which gives the electron temperature. In the present work, the electron temperature is estimated from the measurement of same kind of transitions (i.e. either atomic or ionic lines).

**(ii)** ***Line broadening and electron density***

The electron density of LPP can be estimated from the width of line broadening of spectral line profile. The broadening usually considered in the plasma are Stark broadening, resonance, and van der Waal's interactions. Stark broadening in LPP is due to the collisions of the radiating atom with electrons or ions. The charged species can perturb the energy levels of the radiating atom, which results in broadening the spectral line. The electron density can be determined from the Stark broadening of the well isolated spectral line. The full-width at half maximum (FWHM) of the Stark broadened spectral line profile consist of two terms (electron-impact and ion-impact) which is given by an empirical relation[119]

$$\Delta\lambda_{1/2} = 2w\left(\frac{n_e}{10^{16}}\right) + 3.5A\left(\frac{n_e}{10^{16}}\right)^{1/4} \times\left(1-1.2N_D^{-1/3}\right) w\left(\frac{n_e}{10^{16}}\right) \qquad (2.14)$$

where $w$ is the electron impact parameter, $A$ is the ion broadening parameter and $n_e$ is in $cm^{-3}$. Both the parameters $w$ and $A$ are the weak functions of temperature and their values are available in the literature.[125] $N_D$ is the number of particles in the Debye sphere, given by $N_D = 1.72\times10^9 \frac{[T_e(eV)]^{3/2}}{\left[n_e(cm^{-3})\right]^{1/2}} cm^{-3}$. The above eqn. (2.14) is applicable only when the following criteria are satisfied (i) $N_D \geq 1$ and (ii) $0.05 \leq An_e^{1/4}10^{-4} \leq 0.5$.

The electrons mainly contribute to the collisions with neutral atom.[126] Therefore, the second term (ion impact term) can be safely neglected.[35] After neglecting the second term, eqn. (2.14) becomes

$$\Delta\lambda_{1/2} = 2w\left(\frac{n_e}{10^{16}}\right) \qquad (2.15)$$

In the present work, the experimental line profiles are fitted with Voigt profile (convolution of Lorentzian and Gaussian functions). The Lorentzian profile is due to Stark broadening whereas Gaussian profile is due to instrumental broadening and Doppler broadening. The width of the experimental spectral line ($\Delta\lambda_{1/2}$) is corrected using the relation[127]

$$\Delta\lambda_{1/2} = \left(\left(w_g\right)^2 + \left(w_L{}^2/2\right)\right)^{1/2} + w_L/2 \qquad (2.16)$$

where $w_g$ and $w_L$ are widths of Gaussian and Lorentzian function, respectively. The Doppler broadening arises due to thermal motion of the radiating atom. The Doppler width depends on the temperature of the plasma and it is given by[128] $\Delta\lambda_D = 7.16\times10^{-7}\lambda_{mn}\left(\frac{T}{m}\right)^{1/2}$, where, $m$ is the atomic mass of the radiating atom, $\lambda_{mn}$ is in nm and $T$ is in kelvin (K).

The other important mechanisms contributing to the spectral line broadening are self-absorption, resonance process, Van der Waal's interaction, Zeeman effect, and natural broadening[129] ($\approx10^{-5}$ nm). Self-absorption is a phenomenon in which a photon emitted by a radiative atom at one point in a LPP is absorbed by a different atom before it escapes from the plasma. It affects the line profile and intensity of atomic and ionic transition. The fastest and straightforward method involves the ratio

calculation of the observed strongest to the weakest transition intensity and to compare with the theoretical value. The theoretical line ratio is calculated using the equation[130]

$$S(a.u.) = \frac{g_{m1}(\lambda_{mn1})^3 A_{mn1}}{g_{m2}(\lambda_{mn2})^3 A_{mn2}} \tag{2.17}$$

where the subscript 1, 2 denotes the two lines, respectively. The interaction of atom with same kind results in resonance broadening if either upper or lower energy level of the emission line is connected to ground state by allowed dipole transition. The resonance broadening is directly proportional to ground state number density and oscillator strength. The interaction of radiating atom with unlike atom is Van der Waal's interaction. The ratio of the Stark effect due to mean electric micro field to the Zeeman effect due to an external magnetic field is given by the relation[37],

$$\tau_{Zeeman} = \frac{3}{2} n A_0 \tag{2.18}$$

where $A_0 = \frac{3.43\times10^{-7} n_e^{2/3}(cm^{-3})}{B(gauss)}$ and $n$ is upper principal quantum number. If $\tau_{Zeeman}$ is greater than one, the contribution of Zeeman effect on the line broadening is negligible.

### 2.1.7. *Plasma in the presence of magnetic field*

When the plasma expands in a transverse magnetic field, the electrons and ions experience the Lorentz force. As a result, the electrons and ions are gyrated in opposite direction and confined about the magnetic field. The gyro-radius or Larmor radius ($r_L$) of the charged particles is inversely proportional to magnetic field and is given by

$$r_L = \frac{v_\perp m_q}{qB} \qquad (2.19)$$

where $q$ is charge, $m_q$ is mass of charged particle, and $v_\perp$ is the velocity of charged particle perpendicular to magnetic field. As the gyro-radius of ion is much larger than that of electron, the ions overshoot the electrons and the positive charged layer is formed at the boundary of the plasma plume. The electrons tend to pull ions back and eventually the radially inward electric field is generated. Consequently, it induces the inward diamagnetic current which decelerates the plasma. This diamagnetic current generates magnetic field which expels out the external magnetic field and diamagnetic cavity is produced. The diamagnetism first increases with time and reaches a peak value (at cavity radius). The electron density and temperature decreases rapidly with time in the expanding plasma resulting in a decrease in diamagnetic current (i.e. amount of magnetic field displaced). The external magnetic field begins to penetrate the plasma.[45]

The stopping radius or cavity radius is the distance at which the plasma is considered to be decelerated (confinement occurs) considerably and it stops in the ideal case. In other words, the plasma thermal pressure is equal to the magnetic pressure ($P_{mag} = B^2/2\mu_0$ where $\mu_0$ is the absolute permeability of air) at the stopping radius. It can be estimated from the conservation of energy. The confinement of plasma is indicated by a dimensionless quantity called $\beta$-parameter which is the ratio of thermal and magnetic pressure[131]

$$\beta = \frac{n_e k_B T_e}{B^2 / 2\mu_0} \qquad (2.20)$$

The consideration of ambient pressure in $\beta$-parameter is not discussed in most of the earlier studies. In the present thesis, the correction is made in eqn. (2.20) by adding the magnetic pressure as ($B^2/2\mu_0 + P_0$). When $\beta$ is equal to one the plasma stops at stopping radius i.e. it stops when the magnetic energy is approximately equal to kinetic energy of plasma expansion.[43,58,59] The stopping radius ($R_b$) was also calculated from the conservation of energy by introducing the contribution of ambient air pressure and is given by [132]

$$E_L = \frac{1}{2}Mv^2 + \left(\frac{B^2}{2\mu_0}\right)V + \int P_{air}\,dV\,, \qquad (2.21)$$

where $E_L$ is the laser energy absorbed in the target, $V$ is the volume of the plasma, $v$ is the velocity, $P_{air}$ is air pressure, and $M$ is the total mass of plasma plume. By assuming $v = 0$ at stopping radius and plasma as hemi-spherical in shape, $R_b$ is given by

$$R_b = \left(\frac{3E_L}{2\pi}\frac{1}{P_{air}+B^2/2\mu_0}\right)^{1/3} \qquad (2.22)$$

The estimation of stopping radius of plasma by considering the ambient air pressure is not documented. The stopping radius estimated from eqn. (2.22) in the present thesis is found to be in good agreement with spectroscopic results discussed in chapter 4. When the plasma is confined by magnetic field and air ambient, the electron density of plasma becomes higher. The electron temperature of plasma is also increased due to Joule's heating and adiabatic compression.[66] The other possibility is the gain of energy by electrons from collisional de-excitation and recombination process. As a result, the collisional processes (excitation, ionization, and electron-ion

recombination) of plasma get enhanced leading to more excitation/ionization of atoms are excited/ionized which in turn improves the intensity of atomic or ionic transitions. The presence of an external magnetic field during laser ablation causes significant changes in plasma-target interaction. In the presence of magnetic field, more particles in plasma plume get backscattered towards target and deposit on the target. The heat transfer from plasma to target is also improved by frequent collisions of electrons/ions with the target which enhances the laser ablation.[133]

## 2.2. Experimental setup

### 2.2.1. *Optical emission spectroscopy and characterization of magnetic field*

Fig. 2.2(a) shows the schematic of experimental setup for OES. A Q-switched Nd:YAG (Quanta: HYL 101) laser pulse was focused onto a Cu target (99.99 %) using a convex lens (Len 1, $f$ = 15 cm) to generate Cu plasma in air in the absence and presence of magnetic field. The pulse duration and repetition rate of the laser pulse are, respectively, 10 ns and 10 Hz. The laser is capable of producing pulses of maximum energy 200 mJ per pulse when it is operated at second harmonic ($\lambda$ = 532 nm). All measurements in this work are reported at this laser wavelength. An energy meter (Coherent FieldMAX II) was used to measure the pulse energy. A monochromator (SPEX 750M) coupled with photomultiplier (PMT) was used to record the spectra of LPP optical emission. The exit slit is coupled with PMT which detects optical radiation collected from the plasma through entrance slit. The incident radiation is dispersed using reflective grating. The resolution and dispersion of the monochromator are 0.01 nm and 1.1 nm/mm, focal length 0.75 m, and grating of 1200 grooves/mm, respectively. The size of entrance and exit slit of the monochromator was fixed at 50 $\mu$m each.

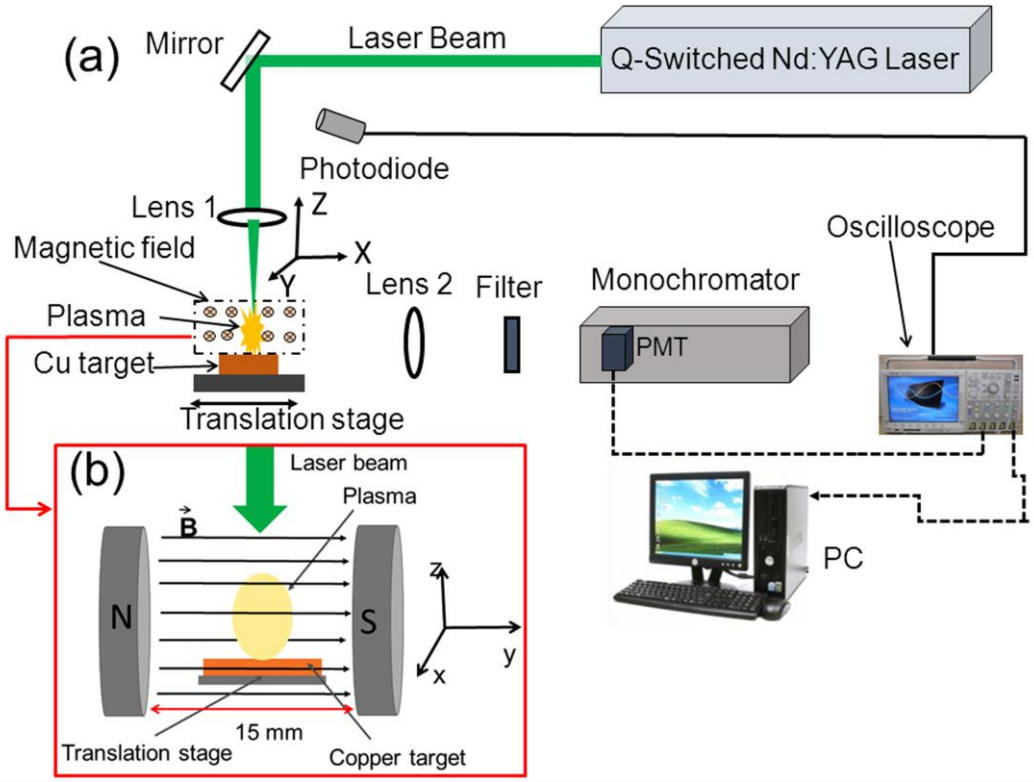


**Fig. 2.2.** (a) Schematic of experimental setup of optical emission spectroscopy. (b) Geometry of magnetic field with respect to plasma expansion.

An electromagnet was used to generate an external magnetic field in plasma. The magnetic field profiles of the electromagnet along the *Y*- and *Z*-axes (origin of the co-ordinate system is taken at the center of the gap), were recorded by gaussmeter. Fig. 2.2(b) shows geometrical arrangement of the electromagnet with respect to LPP expansion. The gap between the poles of the electromagnet was maintained at 15 mm. The magnetic field profiles along *Y*- and *Z*-axes, and calibration curve fitted with linear function are, respectively, shown in Fig. 2.3. The magnetic field along *X*-axis was similar to that in *Z*-axis. The uniformity of magnetic field spans up to 4 cm along *Z*-axis. The magnetic field along *Y*-axis is constant. The magnetic field was varied by

changing the current in the coils. The LPP was allowed to expand in this region of uniform transverse static magnetic field.

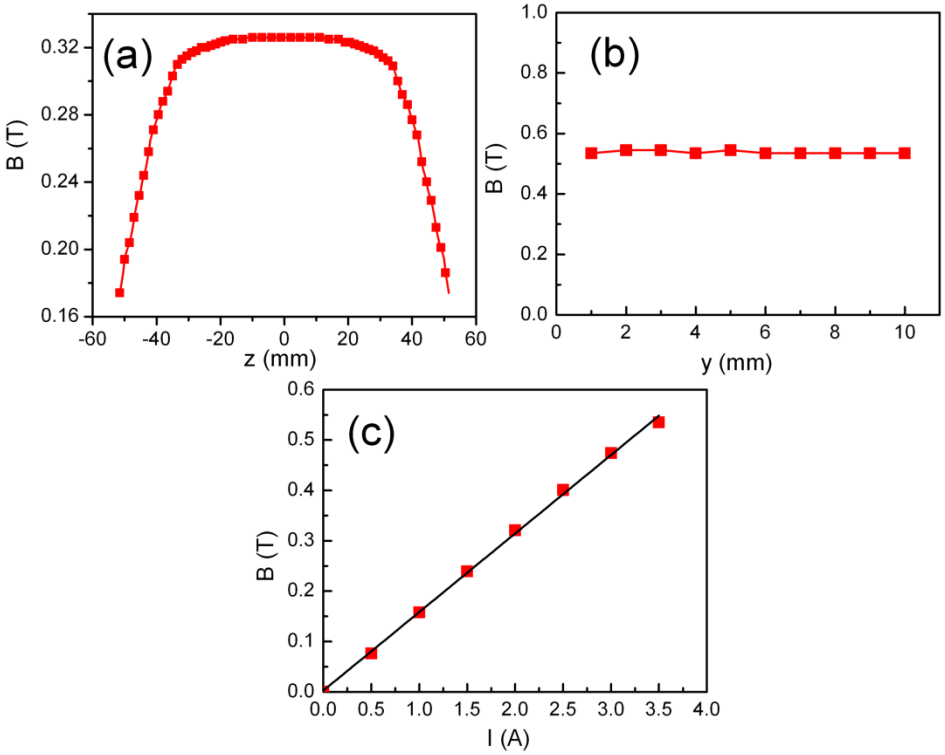


**Fig. 2.3.** Magnetic field profiles along (a) *Z*, (b) *Y*-axes, and (c) calibration curve with linear fit.

To record the temporal profile of atomic/ionic transitions, an oscilloscope (Tektronix DPO 3040) was used. The output of the PMT was fed to the oscilloscope through the scanner. The oscilloscope was triggered with laser signal using a photodiode.

For spatially-resolved spectroscopy, an optical fiber was coupled with the entrance slit of the monochromator (SPEX 750M) and the output was fed to PMT (photomultiplier tube) (Fig. 2.4(a)). The spatial resolution of the measurement along the plasma expansion direction (i.e. *z* direction) was 0.4 mm. The PMT output was connected to the computer to analyze the data. The emission from plasma was

collected using a convex lens (Lens 2) of 10 cm focal length in 1:1 optical geometry and it was imaged on the optical fiber of 400 $\mu$m diameter. By displacing the position of the optical fiber head (mounted on translation stage) along the plasma expansion direction (z), the emission spectra of the copper plasma were collected in the absence and presence of magnetic field. Each spectrum was averaged over three scans.

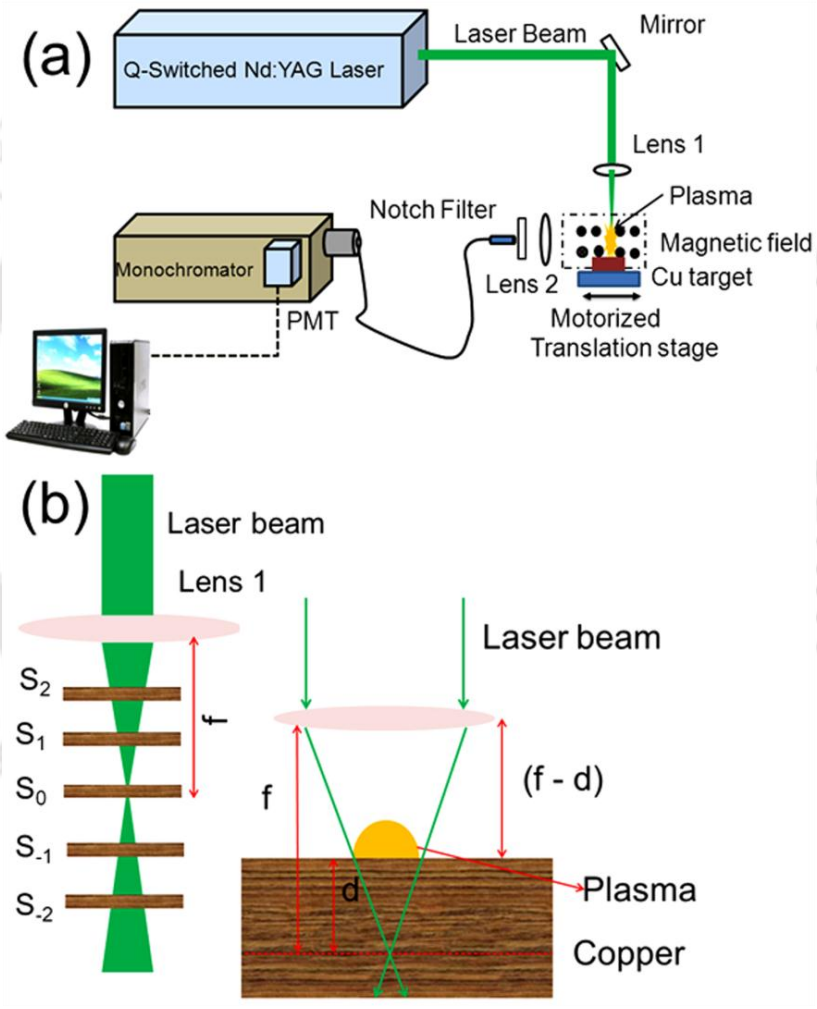


**Fig. 2.4.** (a) Schematic of experimental setup with fiber for spatially-resolved spectroscopy. (b) Position of targets at different lens focusing conditions.

In order to study the effect of lens focusing distance in the presence of magnetic field, the target was kept at different distances from the laser focusing lens

(Lens 1) as shown in Fig. 2.4(b). The five locations from $S_2$ to $S_{-2}$ through $S_0$ correspond to $d$ = 10, 5, 0 -5, and -10 mm, respectively. Here $d$ is the separation between the focal point of focusing lens and target surface. The negative sign signifies that the location of target was below the focus of the lens (Lens 1).

### 2.2.2. *Characterization of post-laser ablated target*

The laser beam profile was extracted from the laser burn pattern image recorded using surface profilometer (Taylor Hobson). A single shot laser burn pattern on photo-paper (inset in Fig. 2.5) was recorded to measure the dimension of laser spot and to extract the beam profile.

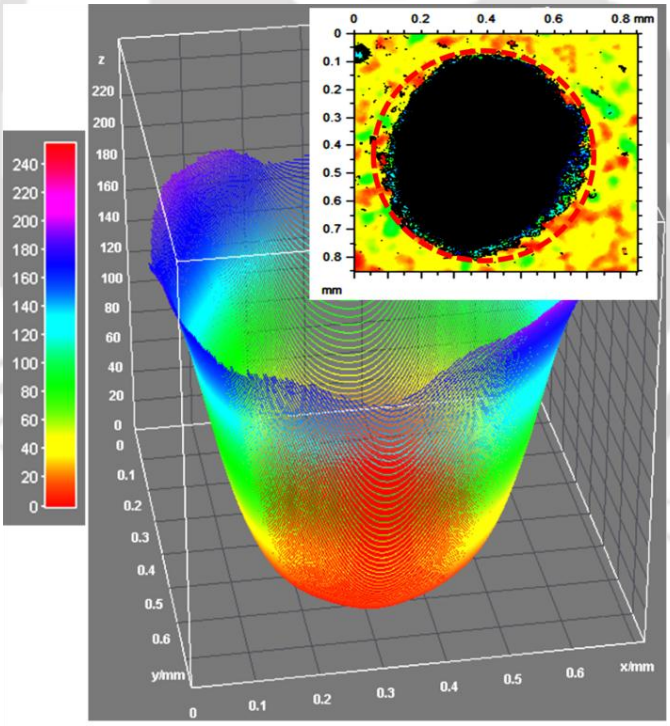


**Fig.2.5.** Laser beam profile and laser burn pattern (inset).

The corresponding beam profile of the laser spot was extracted by selecting the laser burn spot (red circle) and is shown in Fig. 2.5. This spatial profile of the laser

beam is Gaussian in nature. By assuming the profile of the laser beam as Gaussian, the width of the crater formed on the target by laser ablation can be estimated from the relation[13]

$$C_d = \sqrt{2} C_f \left[ \ln\left(\frac{F}{F_{th}}\right) \right]^{1/2} \qquad (2.23)$$

where $F$, $F_{th}$ , $C_d$ , and $C_f$ are laser fluence, threshold fluence, crater diameter, and diameter of laser focused on the target, respectively.

The laser ablated copper target was characterized to discuss the effect of magnetic field on the surface morphology, crystallographic structures, optical properties of deposited particles and depth, diameter, and ablated volume of the crater formed on the target by various techniques: Field emission scanning electron microscope (FESEM), X-ray diffraction (XRD), energy-dispersive X-ray (EDX) spectroscopy, Raman and photoluminescence (PL) spectroscopy, surface profilometer, and optical microscopy.

XRD (Seifert 3003TT) patterns of deposited particles on target in the absence and presence of magnetic field were recorded using CuK$\alpha$ radiation of 1.54 Å. The mean crystallite size ($a$) was also calculated using Debye-Scherrer formula[134]

$$a = \frac{0.9\lambda}{\beta_{1/2} \cos\theta} \qquad (2.24)$$

where $\lambda$ is the wavelength of X-ray radiation, $\theta$ is the Bragg's angle and $\beta_{1/2}$ is the FWHM of the X-ray diffraction. The strain within a material was also estimated by measuring the $d$-spacing between the planes using X-ray diffraction

$$\varepsilon = \frac{(d_n - d_0)}{d_0} \qquad (2.25)$$

where $d_n$ and $d_0$ are measured and strain free $d$-spacing, respectively.

The surface morphology of the laser ablated target was analyzed using FESEM (Sigma, Zeiss) and optical microscopy (Sigma, Zeiss). The volume, depth, and diameter of laser ablated crater were determined using non-contact high resolution surface profilometer. The size of droplets generated during laser ablation was also estimated from FESEM images using ImageJ 1.14. The elemental compositions of the deposited mass on target were identified by EDX equipped with the FESEM.

The post irradiated Cu target was also characterized by micro laser Raman spectroscopy (Horiba Jobin Yvon, LabRam HR800). Ar-ion laser of 514 nm wavelength was used as an excitation source to record Raman spectra of the deposited particles on Cu target. In Raman spectroscopy, a photon from an excitation source of light excites the molecule from a ground state to a virtual state. The excited molecule relaxes from the virtual state to a vibrational/rotational state emitting a photon. The difference in photon energy between the excitation photon and emitted photon results in Raman shift which provides the information of the sample. PL spectroscopy (Horiba, Fluoromax-4) with an excitation source of 405 nm wavelength was carried out to study the optical emission of the particles deposited on copper in the absence and presence of magnetic field.

## 2.3. Finite element method

### 2.3.1. *Numerical method*

Numerical method is employed to obtain the approximate solution for the physical problem whose analytical solution is quite complex. The inability to obtain an analytical solution of such problem is attributed to either the complex nature of differential equation (DE) representing the problem or the difficulties in handling the boundary or initial conditions. An analytical solution is true at any point in the domain of the problem whereas the numerical solution approximates exact solution only at discrete points called nodes. Numerical methods are broadly grouped into two classes: (i) finite difference method (FDM) and (ii) finite element method (FEM). The Finite Element Analysis (FEA) method was originally introduced by Turner et al. in 1956. In FDM, the DE of the problem is written for each node and the derivatives are replaced by difference equations. It uses the difference equation formulation. This method is easy to understand and it is useful for simple problems. However, it is difficult to employ it in a problem with complex geometry or complex boundary conditions. The situation is also true for the problems with non-isotropic material properties. FEM is based on the integral formulation and it is useful in dealing with complex geometries and complex boundaries.[135] A continuous function representing the approximate solution for each element in FEM is known as shape function. The complete solution of the physical problem is obtained by assembling the individual solutions allowing for continuity at the inter-elemental boundaries. ANSYS (13) is a finite element based software package containing more than 100,000 lines of computer program code. It is a very powerful tool which may be used to solve a

variety of problems in physics and engineering like heat transfer, fluid flow, electromagnetism, stress and strain analysis, etc.

### 2.3.2. *Procedures of finite element analysis*

(a) **Preprocessing regime:** (i) Create and discretize the solution domain into a number of small sub-regions (elements) i.e. subdivide the solution domain into nodes and elements. (ii) Assumption of a continuous function to represent an approximate solution of an element is the second step of finite element analysis. (iii) Develop equations representing desired problem for an element. (iv) Assemble the elements to present the entire problem and construct the global stiffness matrix. (iv) Provide boundary, initial conditions, and loading.

**(b) Solution regime:** Solve a set of simultaneous linear or nonlinear algebraic equations to obtain nodal solution such as temperature in heat transfer problem.

**(c) Post processing regime:** Extraction of other important information such as heat flux, principal stresses, etc.

The discretized target model and the flowchart of step by step procedures of the FEM analysis are shown in Fig. 2.6(a) and 2.6(b), respectively. Fig. 2.7 shows the discretized target model generated by Ansys. The enlarged view of more refined region of the target is shown in the figure bounded by red color rectangular region.

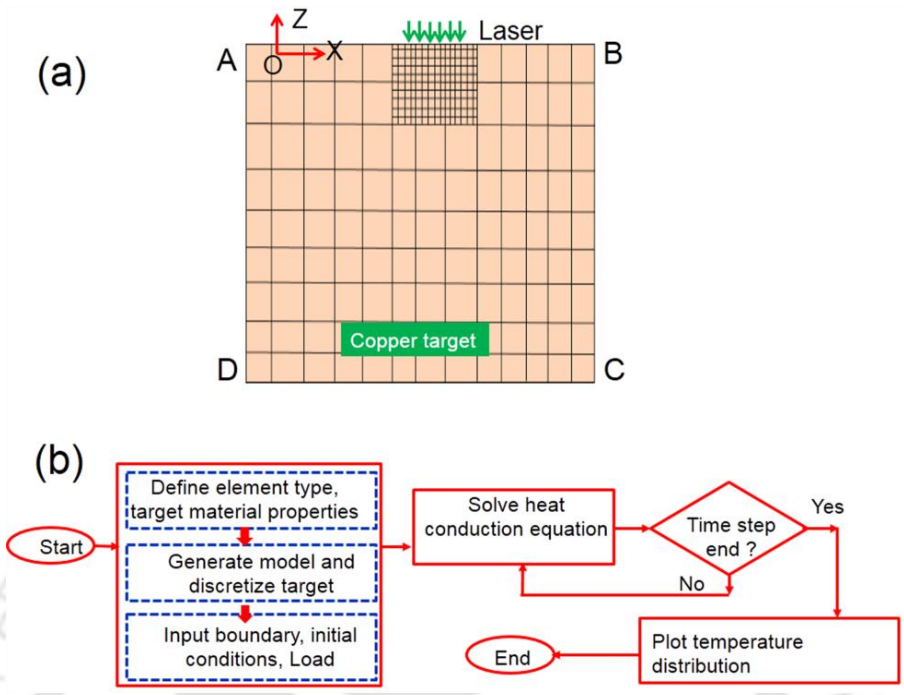


**Fig. 2.6.** (a) Schematic of discretized target model. (b) Flowchart of finite element analysis.

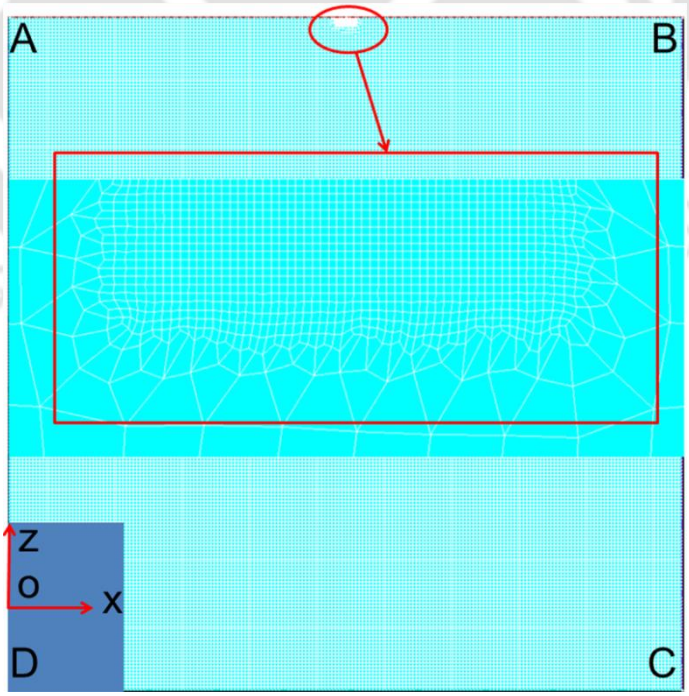


**Fig. 2.7.** Discretized target model generated by ANSYS software and enlarged view of more refined region where the laser radiation focused.

### 2.3.3. *Modeling of laser ablation*

In order to model the laser ablation, the FEM was employed using Ansys code. The mathematical formulation is based on the 2D heat conduction equation[100]

$$\rho C\frac{\partial T(x,z,t)}{\partial t}-k\nabla^2 T(x,z,t)=Q(z,t) \qquad (2.26)$$

where $\rho$ is the density, $C$ is the specific heat, $T$ is the temperature, and $Q(z, t)$ is the heat source, respectively. The heat source term $Q(z, t)$ is provided by the absorbed laser intensity given by

$$Q(z,t)=I_0(t)(1-R)\alpha\exp(-\alpha z);\ I_0(t)=I_0\exp\left[-\frac{(t-t_0)^2}{\tau^2}\right] \qquad (2.27)$$

where $R_{ref}$ is the reflectivity, $\alpha_{ab}$ is the absorption coefficient of target, $\tau$ is the pulse duration, and $t_0$ is the time at which laser intensity is maximum. In order to take into account the effect of energy loss due to the evaporation of the target material, the heat conduction equation along with the energy balance[136] ($\rho_v \Delta H_{lv} u=-k\frac{dT}{dz}$), where $u$ is the rate of vaporization, was solved in this model. The vaporization rate was calculated using the relation[137]

$$u=\frac{\alpha}{\rho(2\pi RT)^{1/2}}\left(P_{vap}-P_0\right) \qquad (2.28)$$

where $\alpha$ is the correction for the backscattering of evaporated atoms (i.e. 1 for metals) and $R$ is the universal gas constant. The vapour temperature ($T_{vap}$) is approximately related to surface temperature ($T_s$) by the relation[138] $T_{vap}$ = 0.65 $T_s$. The ablation depth due to vaporization during a pulse is given by $h_{vap}= u\tau$. In this model, the vapor pressure of the evaporating surface acts as a piston, exerting pressure on melted layer at the bottom of the crater, causes the liquid to move in radial direction out of the

pressure zone.[139] From the surface temperature, the vapor pressure was determined using Clausius-Clapeyron equation[138] in the absence of magnetic field

$$P_{vap}\left(T_S\right) = P_0 \exp\left[\frac{\Delta H_{lv}\left(T_s - T_v\right)}{RT_sT_v}\right] \qquad (2.29)$$

where $T_v$ is the vaporization temperature of the material.

Laser ablation has been studied extensively using experimental and numerical methods as discussed in chapter 1. However, the simulation on laser ablation in the presence of magnetic field is not documented. In the present thesis, the magnetic pressure was considered and accordingly the Clausius-Clapeyron equation was modified as discussed in the next paragraph. An attempt was also made to explain the experimentally observed ablation rate in the magnetic field on the basis of modified Clausius-Clapeyron equation[114] as discussed in chapter 6, as per our knowledge for the first time.

In the presence of magnetic field, the ambient pressure is assumed to be contributed by combined effect of air and magnetic pressure. The change in pressure with respect to temperature ( $\frac{dP}{dT}$ ) in phase transformation is given by Clausius-Clapeyron equation, $\frac{dP}{dT} = \frac{\Delta H_{lv}}{TdV}$ where $dV$ ($V_{vap}$ - $V_l$, where $V_{vap}$ and $V_l$ are the volumes of vapour and liquid, respectively) is the change in volume. Normally since the volume of vapour is much higher than the volume of liquid, $dV \approx V_{vap} = RT/P$. Therefore, the above equation can be expressed as $\frac{dP}{dT} = \frac{\Delta H_{lv}}{RT^2}dT$ . For vaporization in air, at $T = T_v$ the vapour pressure is $P = P_0$ (atmospheric pressure). The vapour pressure at any temperature other than $T_v$ is obtained by integrating above equation from $T = T_v$ to $T = T_s$ (say) and $P = P_0$ to $P = P_{vap}$. In the presence of magnetic field at

$T = T_v$, the target material vaporizes and the vapour particles experience the atmospheric pressure and magnetic pressure as well i.e. at $T = T_v$, $P = (P_0 + P_{mag})$. Because, the vaporized mass contain ions and electrons which interact with magnetic field. Therefore, the plasma experiences both magnetic and air pressure. The vapour pressure at any temperature ($T_s$) is given by integrating the above equation[140] from $T = T_v$ to $T_s$ and $P = (P_0 + P_{mag})$ to $P_{vap}$ i.e.

$$\int_{P_0+P_{mag}}^{P_{vap}} \frac{dP}{P} = \frac{\Delta H_{lv}}{R}\int_{Tv}^{T_s}\frac{dT}{T^2} \text{ i.e. } P_{vap}(T_s) = (P_0 + P_{mag})\exp\left[\frac{\Delta H_{lv}(T_s - T_v)}{RT_sT_v}\right] \qquad (2.30)$$

Therefore, $P_0$ is replaced by $P_0 + P_{mag}$. The melted layer of the target experiences the recoil forces exerted by the vaporized mass. The recoil pressure is close to the half of the vapour pressure[138] i.e. $P_{recoil} = 0.54P_{vap}$. The total force on the irradiated target is given by $\int P_{recoil}\, ds \approx P_{recoil}\, \pi R_L^{\,2}$, where $ds$ is the area element. The melt ejection rate was estimated using piston effect using eqn. (2.7). Here, the pressure profile is approximated as a "top hat" with constant pressure ($P_{vap}$ (max)). The melted expulsion depth ($h_{melt}$), during the laser pulse, is given by the relation[139] $h_{melt} = v\tau = \left(\frac{2\Delta P}{\rho}\right)^{1/2}\tau$. The assumptions made in the simulation are (i) energy loss due to radiation and convective transport phenomenon is neglected as the heating process is very fast and (ii) for simplicity, the effect of target surface roughness on laser absorption is neglected. It has been reported that the solution of the heat conduction equation with temperature dependent thermo-physical properties is more accurate as compared with temperature independent properties.[141,142] The temperature dependent thermo-physical properties of the material (i.e. enthalpy, $H$ (T)) were also considered in the present work to estimate the surface temperature which is not well documented, especially,

for Cu and Al. The temperature dependent thermo-physical properties of the material takes into account the latent heat required during phase transformation.[143] By assuming the crater as paraboloid with radius equal to spot radius and height (≈ total ablation rate times pulse duration), the ablated volume of crater was estimated both in the absence and presence of magnetic field.

# Chapter 3

## *Effect of Variation of Laser Fluence and Magnetic Field on Laser-Produced Copper Plasma*

The presence of magnetic field affects the electron density and temperature of LPP which in turn changes the optical emission intensity of LPP. This change in the intensity is affectively used to investigate the sensitivity of LIBS.[42,52,53] The optical emission of LPP depends on various laser parameters. Laser fluence is one of them which strongly affects the dynamical properties of plasma. However, most of the previous studies on effect of magnetic field on laser-produced Cu plasma in air are at a fixed magnetic field and laser fluence.[50–52,59] Therefore, the optimized laser fluence and magnetic field are required for systematic studies on the effect of magnetic field on LPP. In this chapter, the laser fluence and magnetic field are optimized which are then kept fixed for subsequent studies. These optimized parameters may be useful as prerequisite for further investigations on the effect of magnetic field on LPP especially at high pressure air ambient.

### 3.1. Experimental details

The detailed experimental setup used in this study is discussed in chapter 2. To generate Cu plasma in air, a high power second harmonic pulsed laser of 10 ns pulse duration and 10 Hz repetition rate was focused onto a Cu target. The optical emission spectra of Cu plasma were recorded at different laser fluences and magnetic fields, respectively. In the first part of the study (section 3.2.), the laser fluence was varied from 7 to 21 $Jcm^{-2}$ and the magnetic field was kept constant at 0.5 T. The magnetic

field was fixed at maximum value of 0.5 T as it improved the intensity of LPP significantly.[42] It was observed that the intensity of spectral lines, electron density and temperature achieved were relatively more pronounced at 14 $Jcm^{-2}$. Therefore, with the laser fluence fixed at 14 $Jcm^{-2}$, the effect of variation of magnetic field was investigated by varying the magnetic field from 0 to 0.5 T and is discussed in section 3.3. The knowledge of the electron temperature and density is vital for better understanding of atomic processes like excitation and recombination which in turn affects the emission in LPP. Therefore, the electron temperature and density were estimated at each experimental condition.

## 3.2. Effect of variation of laser fluence on Cu plasma at a fixed magnetic field

### 3.2.1. *Intensity variation of spectral line with laser fluence*

The time integrated spectra of laser-induced Cu plasma in air at different laser fluence (7, 11, 14, 18, and 21 $Jcm^{-2}$) were recorded in the absence and presence of magnetic field (0.5 T). Fig. 3.1 shows the simplified energy level diagram of the prominent Cu I transitions which are Cu I (510.5 nm): $4p\ ^2P_{3/2} \rightarrow 4s^2\ ^2D_{5/2}$, Cu I (515.3 nm): $4d\ ^2D_{3/2} \rightarrow 4p\ ^2P_{1/2}$, Cu I (521.8 nm): $4d\ ^2D_{5/2} \rightarrow 4p\ ^2P_{3/2}$. Cu I (570.0 nm): $4p\ ^2P_{3/2} \rightarrow 3d^9\ ^2D_{3/2}$, and Cu I (578.2 nm): $4p\ ^2P_{3/2} \rightarrow 3d^9\ ^2D_{5/2}$. Table 1 lists the atomic transition parameters [124,144] which are used to estimate the plasma parameters. The spectra of Cu plasma recorded at different laser fluences in the absence and presence of magnetic field are shown in Fig. 3.2. In the absence of magnetic field, as the laser fluence increased from 7 to 21 $Jcm^{-2}$, the integrated intensity of all Cu atomic spectral lines increased. It is attributed to an increase in ablation which in turn increases the electron temperature and density. In the presence of magnetic field also, it followed the same trend.

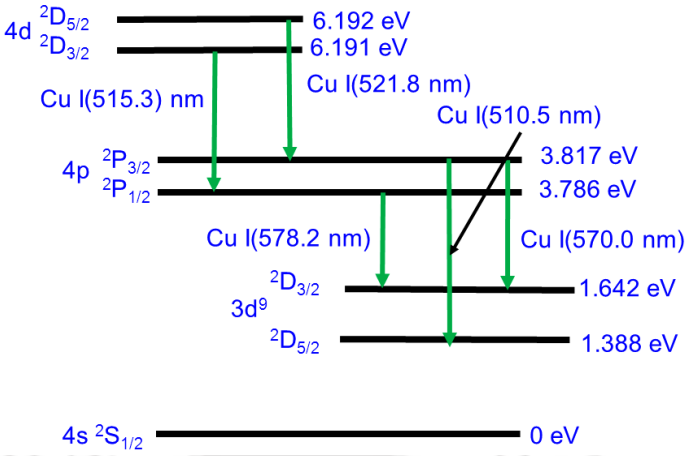


**Fig. 3.1.** Energy level diagram of Cu I transitions.

**Table 3.1.** Atomic Cu transition parameters.

| Wavelength (nm) | $g_m$ | $g_n$ | $A_{mn}$ ($10^8$ $s^{-1}$) | $E_m$ (eV) | $E_n$ (eV) |
|---|---|---|---|---|---|
| 510.5 | 4 | 6 | $2.0 \times 10^{-2}$ | 3.817 | 1.389 |
| 515.3 | 4 | 2 | $6.0 \times 10^{-1}$ | 6.191 | 3.786 |
| 521.8 | 6 | 4 | $7.5 \times 10^{-1}$ | 6.192 | 3.817 |
| 570.0 | 4 | 4 | $2.4 \times 10^{-3}$ | 3.816 | 1.642 |
| 578.2 | 2 | 4 | $1.6 \times 10^{-2}$ | 3.786 | 1.642 |

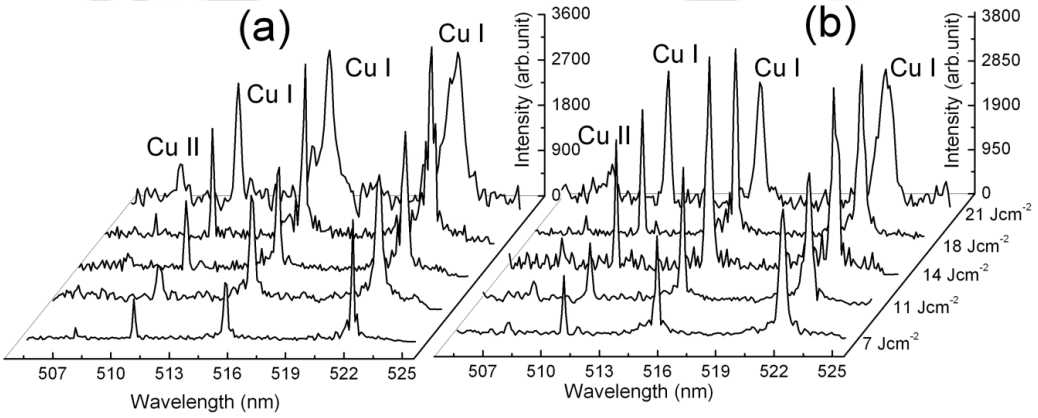


**Fig. 3.2.** Spectra of Cu plasma at (a) $B$ = 0 T and (b) 0.5 T at laser fluences (7, 11, 14, 18, and 21 Jcm$^{-2}$).

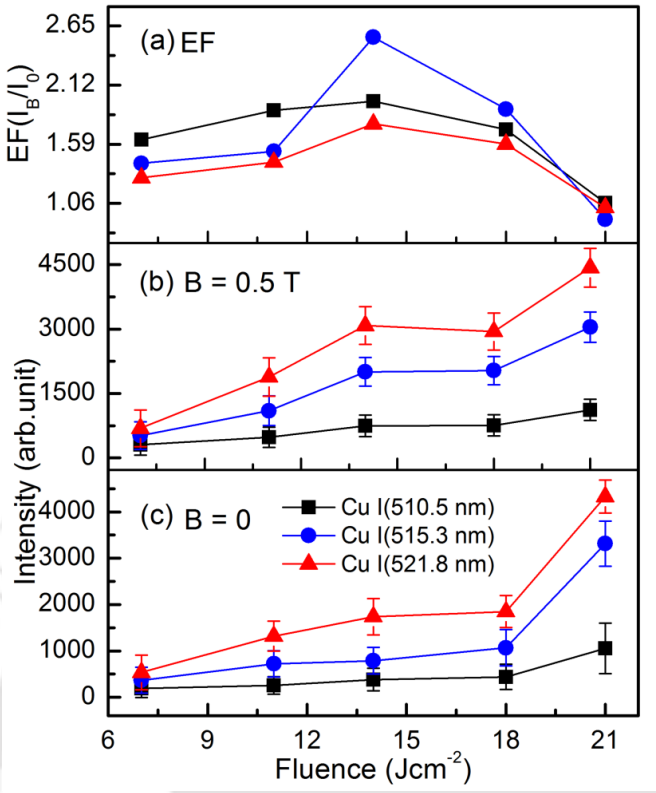


**Fig. 3.3.** (a) Enhancement factor. Intensity variation of Cu I lines with laser fluence at (b) $B$ = 0.5 T and (c) $B$ = 0 T.

However, the intensity was more pronounced than that without magnetic field. It is due to the generation of large number of charged particles at higher laser fluence which resulted in an increase in the plasma-magnetic field interaction. Consequently, the magnetic field confinement of the plasma increased. As a result of an increase in magnetic confinement, the plasma density is higher at higher fluence which in turn leads to an increase in the excitation rate. However, the decrease in intensity of atomic spectral lines at the laser fluence of 21 Jcm$^{-2}$ in the presence of magnetic field is more likely due to an increase in the collisional ionization of Cu atom. Fig. 3.3(b) and (c) shows the variation of the Cu I line intensity as a function of laser fluence at $B$ = 0.5

and $B$ = 0 T, respectively. The enhancement in the intensity can also be looked at from EF point of view. The EF was maximum at 14 $Jcm^{-2}$ irrespective of the nature of spectral lines. The maximum EF of atomic Cu transitions at 14 $Jcm^{-2}$ varied from 1.8 to 2.5 (Fig. 3.3(a)). A relatively weaker ionic line Cu II at 507.2 nm was also observed in the spectra (Fig. 3.2). The intensity of Cu II (507.2 nm) increased as laser fluence was increased.

At the lower laser fluence *viz*. 7 and 11 $Jcm^{-2}$ at $B$ = 0 T, the intensity of Cu II (507.2 nm) is quite low. However, the intensity increased with an increase in the laser fluence from 11 to 21 $Jcm^{-2}$. In the presence of magnetic field, this ionic line appeared with higher intensity even at lower fluence of 7 $Jcm^{-2}$. It is due to an increase in the collisional ionization of plasma as the temperature and density of the plasma is increased in the presence of magnetic field. Here, the lowering of ionization is discussed as follows. The ionization of the atom is significantly lowered by the presence of micro-electric field created in the plasma.[145] The lowering of ionization ($\Delta\chi$) can be obtained from the relation[37] $\Delta\chi(eV) = 6.9\times10^{-7} n_e^{1/3}$ where $n_e$ is in $cm^{-3}$. This relation is valid in the first ionization state dominated plasma. The first ionization energy (7.7 eV) is lowered as the electron density is increased. Since the electron density is higher in the presence of magnetic field, the ionization energy is lower than that without magnetic field. Therefore, the ionization rate of atom is more pronounced at higher laser fluence in the presence of magnetic field. Accordingly, the population of atom in the excited state is decreased and hence the intensity of Cu I transition is lower at higher laser fluence (beyond 14 $Jcm^{-2}$) in the presence of magnetic field. Fig. 3.4 shows the intensity variation of ionic line Cu II (507.2 nm).

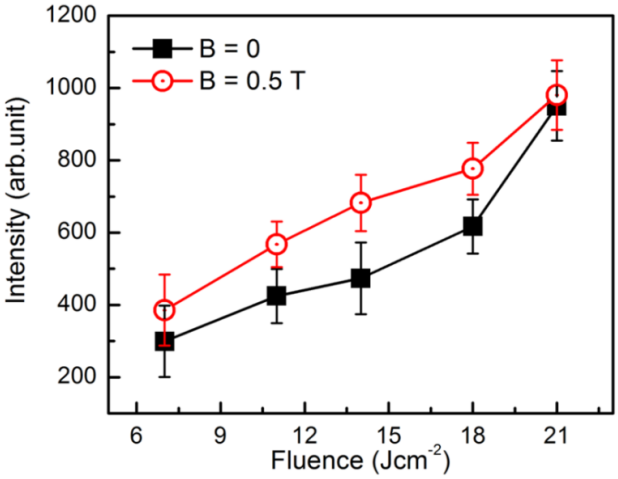


**Fig. 3.4.** Intensity variation of Cu II (507.2 nm) as a function laser fluence in the absence and presence of magnetic field.

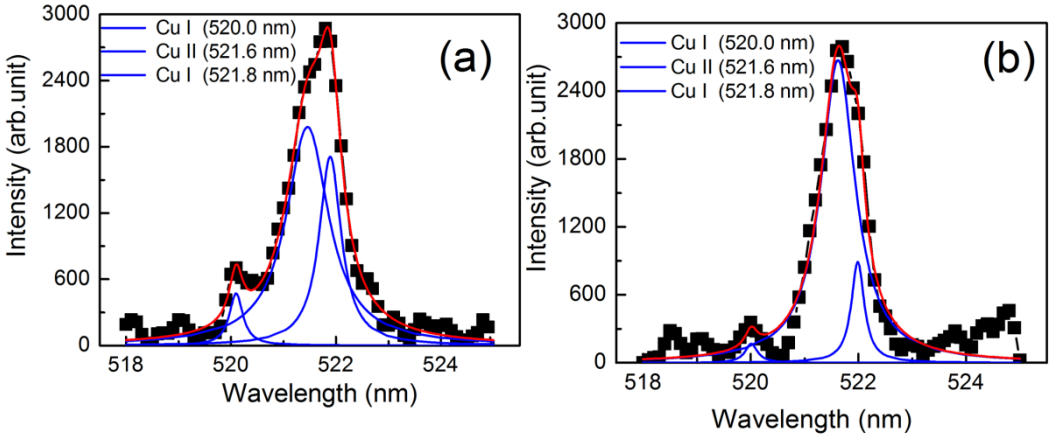


**Fig 3.5.** Multiple fitted spectral line Cu I (521.8 nm) at (a) *B* = 0 T and (b) *B* = 0.5 T.

In the case of ionic transition Cu II (507.2 nm) also, the EF initially increased as the laser fluence increased up to 14 Jcm$^{-2}$, however, it is also observed that it decreased significantly beyond 14 Jcm$^{-2}$. It may be due to the excitation of ion to the higher excited energy state. EF of Cu II (507.2 nm) is 1.45. More interestingly, the spectral lines Cu I (515.3 nm) and Cu I (521.8 nm) at higher laser fluence (21 Jcm$^{-2}$) were significantly broad. The spectral line profile structure was different in the presence of magnetic field. The Cu I (521.8 nm) consists of only one peak at 7 to 18

$Jcm^{-2}$ but at the laser fluence of 21 $Jcm^{-2}$ the peak consists of three transitions at Cu I (520.0 nm), Cu II (521.6 nm), and Cu I (521.8 nm) (Fig. 3.5). The appearance of broadened peak at higher laser fluence of 21 $Jcm^{-2}$ is due to the convolution of these peaks. The intensity of Cu II (521.6 nm) is considerably increased in the presence of magnetic field. It is attributed to more collisional excitation of ion to the excited state i.e. Cu II (521.6 nm) whose upper energy state is higher than that of Cu II (507.2 nm). This could have resulted in a decrease in the intensity of Cu II (507.2 nm) in the presence of magnetic field at higher laser fluence. At the same time, the intensity of Cu I at 520.0 and 521.8 nm was decreased in the presence of magnetic field at higher laser fluence which resulted in the decrease in EF of the atomic line. At 21 $Jcm^{-2}$, $\Delta\chi$ = 0.64 eV, therefore, the ionization potential (7.7 eV) is lowered by 0.64 eV i.e. the effective ionization state is 7.06 eV. The electron temperature at this laser fluence is 0.94 eV. The upper energy state of Cu I (521.8 nm) is 6.2 eV. Therefore, the Cu atoms in the excited state of Cu I (521.8 nm) can be ionized on collisions with the electrons.

### 3.2.2. *Determination of electron density and temperature*

To characterize the plasma, the electron density and temperature were determined. The electron density was calculated from spectral line profile width of Cu I (510.5 nm) using eqn. (2.15). The line width was obtained from the fitted Voigt profile (i.e. convolution of Lorentz and Gaussian functions). With the measured values of electron temperature (0.96 eV), density ($6.63\times10^{17}$ $cm^{-3}$), and ion impact parameter[125] ($A$ = 0.0204), the value of $N_D$ is 2 (>1) and $An_e^{1/4}10^{-4}$ is 0.06 which lies between 0.05 and 0.5. Therefore, the applicability of the eqn. (2.15) to measure

electron density is justified. The Doppler broadening arises due to the thermal motion of radiating atom. The Doppler broadening width [128] and natural broadening width of Cu I(510.5 nm) are, respectively, in the order of $10^{-3}$ nm and $10^{-5}$ nm.[129] These are very small in comparison with the experimentally measured line widths. The ratio ($\tau$) of Stark and Zeeman broadening is given by eqn. (2.18). For the experimental parameters ($B$ = 5000 G) and the measured value of electron density ($n_e$ = 8.65 × $10^{17}$ $cm^{-3}$), the value of $\tau$ is greater than one, therefore the contribution of Zeeman effect on the line broadening is negligible. The contribution of self-absorption is also insignificant which can be understood using eqn. (2.17) as follows. For instance, at $B$ = 0 T, the observed ratios, Cu I (510.5 nm)/Cu I (515.3 nm) and Cu I (510.5 nm)/Cu I (521.8 nm) at highest laser fluence in the present study (i.e. 21 $Jcm^{-2}$) are, respectively, 0.32 and 0.24. The corresponding theoretical ratios are 0.32 and 0.17, respectively. In the presence of 0.5 T magnetic field, the observed ratios are 0.37 and 0.25, respectively. The observed ratios are very close to the theoretical ratios which justifies that the contribution of self-absorption is insignificant in the present work. Further, the indication of self-absorption is the dip at the center of the spectral line profile which was not observed in the recorded spectra. The upper level of Cu I (510.5 nm) transition is connected to the ground state. The plasma was generated from pure copper (99.99 %), therefore the presence of atoms of other elements is negligible. Therefore, the Van der Waal's interaction in the present work is negligible. The resonance broadening is directly proportional to ground state number density and oscillator strength. The oscillator strength of this transition line is 5.2 × $10^{-3}$ $s^{-1}$ and therefore the pressure broadening is safely neglected. The instrumental line width was determined by measuring FWHM of the Hg emission line (435.8 nm) from mercury

vapor lamp. It was found to be $\Delta\lambda_{\text{instrumental}}$ = 0.04 nm when the size of entrance and exit slit of the monochromator was kept at 50 $\mu$m each. The experimentally recorded Cu I (510.5 nm) was fitted with Voigt function (Fig. 3.6).

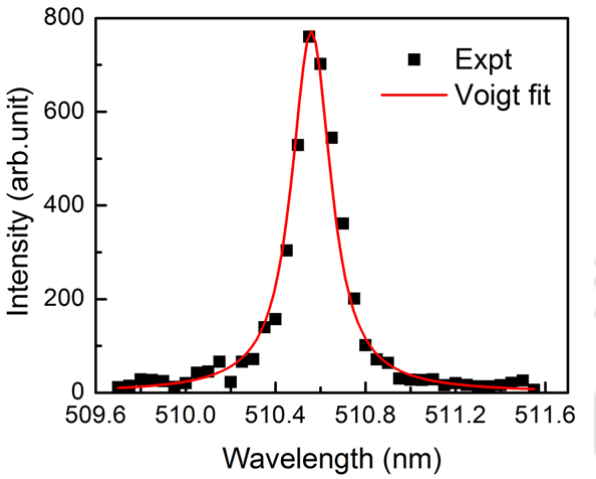


**Fig. 3.6.** Voigt fitted line profile of Cu I (510.5 nm) at 14 Jcm$^{-2}$ and 0.5 T.

The width of the experimental spectral line ($\Delta\lambda_{1/2}$) was corrected using eqn. (2.16). Fig. 3.7(a) shows the variation of electron density with the laser fluence, respectively. In the absence of magnetic field, the electron density increased linearly from (0.28 ± 0.09) × $10^{17}$ to (1.32 ± 0.41) × $10^{17}$ cm$^{-3}$ when the laser fluence increased from 7 to 18 Jcm$^{-2}$. It increased abruptly to (3.08 ± 0.33) × $10^{17}$ cm$^{-3}$ when the laser fluence was further increased from 18 to 21 Jcm$^{-2}$. In the presence of magnetic field, the electron density varied from (1.09 ± 0.29) ×$10^{17}$ to (4.85 ± 0.48) ×$10^{17}$ cm$^{-3}$ when the laser fluence was increased from 7 to 18 Jcm$^{-2}$. However, the electron density decreased slightly when the laser fluence was further increased from 18 to 21 Jcm$^{-2}$. The density is maximum at 14 Jcm$^{-2}$ and it was 3.5 times higher than the electron density in the absence of magnetic field. This is due to the fact that the

plasma is confined to the smaller region near the target surface in the presence of transverse magnetic field. The magnetic field interacts with charged particles through Lorentz force. At lower laser fluence the ablation rate is small generating less number of free electrons in the plasma by direct ablation. As a result, the magnetic field weakly interacts with the plasma. More charged species (electrons and ions) are produced at a higher laser fluence by direct ablation and these charged species strongly interact with the magnetic field and the confinement of plasma is enhanced. It is also reported that the electron density of laser produced Cu plasma in air is found to increase in the presence of magnetic field at 0.8 T.[146] The other possible reason is more heat transfer from plasma to the target in the presence of the magnetic field since the plasma is confined near the target surface. Because of this, more mass of copper was ablated and eventually led to an increase in the plasma density. It has been already shown that more material mass is removed from the silicon target via laser ablation in the presence of the magnetic field.[49]

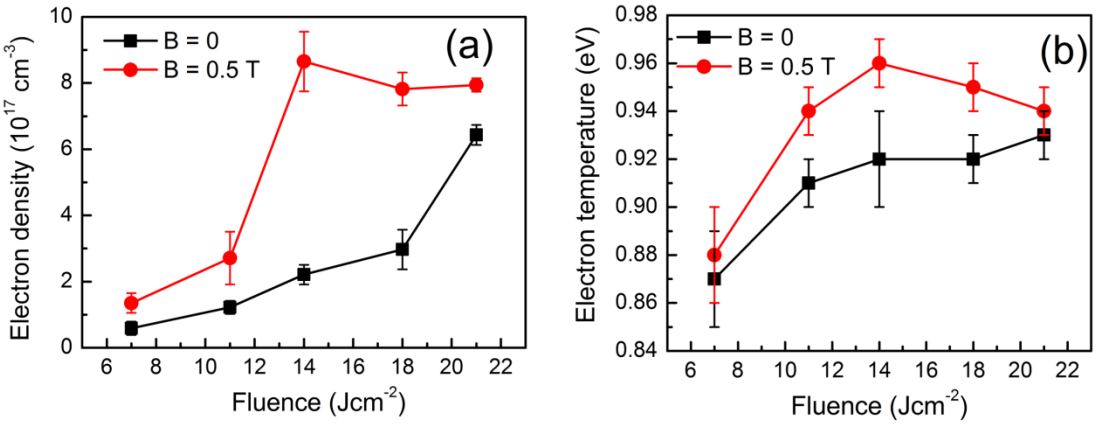


**Fig. 3.7.** Variation of (a) electron density and (b) electron temperature at $B$ = 0 and 0.5 T with laser fluence.

The LPP was assumed to be in LTE (discussed in section 4.4). Boltzmann plot (eqn. 2.13) was obtained using three prominent atomic transitions Cu I (510.5 nm), Cu I (515.3 nm), and Cu I (521.8 nm). Fig. 3.7(b) depicts the variation of electron temperature with the laser fluence. As the laser fluence was increased from 7 to 11 $Jcm^{-2}$, the electron temperature increased from (0.87 ± 0.02) to (0.91 ± 0.01) eV in the absence of magnetic field. Further increase in laser fluence from 11 to 18 $Jcm^{-2}$, the electron temperature remained at around (0.92 ± 0.02) eV. It was again marginally increased to (0.93 ± 0.01) at 21 $Jcm^{-2}$ laser fluence. Though the electron temperature in the presence of magnetic field followed nearly the same trend but has a higher value than without magnetic field. The higher electron temperature in the presence of the magnetic field could be due to two possible reasons: (i) Joule's Heating and (ii) adiabatic compression of the plasma.[68] The induced current in the plasma in the presence of magnetic field gives rise to Joule's heating. This energy comes at the expense of the magnetic field energy.The other possibility is the gain in energy by the electrons through collisional de-excitation and recombination of ions.[147] However, the electron temperature was found to decrease when the laser fluence was further increased from 18 to 21 $Jcm^{-2}$ in the presence of the magnetic field. During electron-neutral atom collision, the energy is transferred to atom, which reduces electron temperature at higher laser fluence. Raju et al.[55] also showed that decrease in electron temperature is due to an increase in collisions in the magnetically confined plasma.

If the frequency of the incident laser is less than the plasma frequency, the laser is reflected. The plasma frequency ($\nu_p$) is given by [71] $\nu_p = 8.9\times10^3\sqrt{n_e(cm^{-3})}$,

where $n_e$ is the electron density. In the present experiment, the maximum electron density of LPP occurs at 14 $Jcm^{-2}$ in the presence of the magnetic field. The electron density of the LPP in the presence of the magnetic field is $8.7 \times 10^{17}$ $cm^{-3}$. Therefore, the plasma frequency is $8.3 \times 10^{12}$ Hz whereas the incident laser frequency is $5.63 \times 10^{14}$ Hz, which is greater than the plasma frequency. This shows that the laser energy loss due to reflection from plasma is insignificant. Further, as discussed in chapter 5 on the laser ablation in the presence of the magnetic field, the rate of melt ejection and splashing of droplet increased in the presence of magnetic field. At higher laser intensity the ejection of droplets is high.[148] Therefore, at higher laser fluence and in the presence of magnetic field, the plasma is more likely to contain a large number of droplets or mass ejected in plasma which may cause scattering of laser radiation. This in turn reduces the laser-target coupling. As a result, the plasma density and temperature was slightly lowered at higher laser fluence in the presence of magnetic field.

## 3.3. Effect of variation of magnetic field on Cu plasma at a fixed laser fluence

### 3.3.1. *Intensity variation of spectral line with magnetic field*

The Cu emission spectra were recorded by varying magnetic field from $B = 0$ to 0.5 T. In this study, the laser fluence was fixed at 14 $Jcm^{-2}$. The laser-induced breakdown Cu plasma spectra recorded at $B = 0$, 0.1, 0.3, and 0.5 T are shown in Fig. 3.8. Fig. 3.9 shows the variation of the intensity of Cu I lines as a function of $B$. When $B$ is applied, the electron density and temperature undergoes a change which in turn affects the intensity of these transitions. As $B$ was increased, the intensity of all the five Cu I lines increased initially up to 0.3 T and then decreased slightly at 0.5 T. The intensity of the spectral lines depends on the density of electrons, atoms, ions,

coefficient of electron impact excitation, and radiative recombination. The radiative recombination rate depends on the temperature and is given by[68]

$R_r = 2.7\times10^{-19} n_e n_i Z^2 T_e^{-3/4}\,(m^{-3}s^{-1})$.

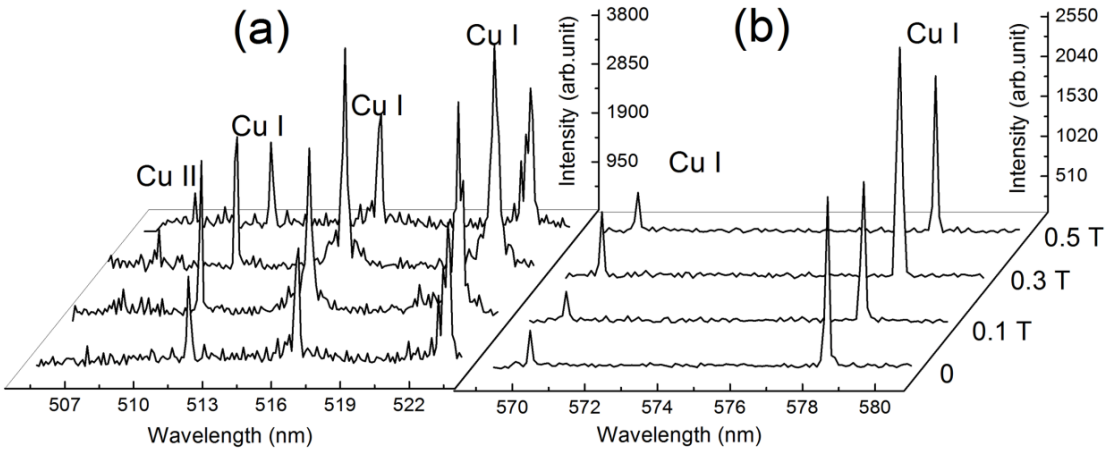


**Fig. 3.8.** Cu optical emission spectra at $B$ = 0, 0.1 0.3, and 0.5 T.

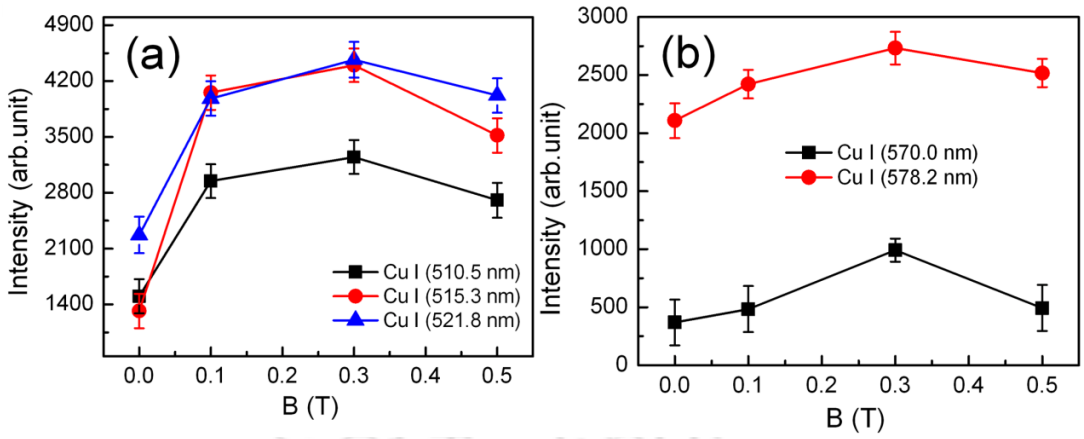


**Fig. 3.9.** Intensity variation of Cu I (510.5), Cu I (515.3), and Cu I (521.8) lines as a function of magnetic field.

Since the electron temperature is higher in the presence of $B$, the radiative recombination decreased whereas the electron impact excitation rate increased. The enhancement in the intensity of Cu atomic lines in the presence of $B$ is attributed to

the increase in electron impact excitation rate of Cu I due to the increase in the effective plasma density and temperature as a result of magnetic confinement of the plasma. At higher *B* the enhancement decreased due to an increase in the ionization of atom. The intensity EF is different for the different lines which is attributed to the difference in electron impact excitation rate.[126] The ionic line was more intense due to the increase in ionization as a result of increase in the electron temperature and collisional process.

### 3.3.2. *Determination of electron density and temperature*

Using the same approach as discussed in section 3.2.2., the electron density was calculated based on line broadening of spectral line. Fig. 3.11(a) shows the electron density variation as a function of magnetic field. The electron density varied from $(3.6 \pm 0.1) \times 10^{17}$ to $(6.1 \pm 0.3) \times 10^{17}$ $cm^{-3}$with the increase in *B* from 0 to 0.5 T. It was found to be maximum i.e. $(6.2 \pm 0.10) \times 10^{17}$ $cm^{-3}$ at 0.3 T magnetic field but reduced slightly at higher *B* = 0.5 T. When the laser-induced Cu plasma expands in the transverse magnetic field, due to magnetic Lorentz force, the plasma gets confined to a smaller region near the target. As a result, the electron density of Cu plasma increased. Since, the Lorentz force interacts with charged particle, the Cu atoms in the magnetically confined plasma gets decelerated due to increase in collisions with other plasma particles. The confinement of plasma by magnetic field is determined by the $\beta$-parameter. By taking the experimental parameters and results, the plasma thermal pressure was found to be $5.3 \times 10^4$ $Nm^{-2}$ and magnetic pressure at *B* = 0.3 T is $3.6 \times 10^4$ $Nm^{-2}$. Therefore, the $\beta$-parameter obtained by considering the effect of air pressure is 0.4 which signifies the confinement of plasma. At the laser fluence

of 5.5 $Jcm^{-2}$ the calculated stopping radius at $B$ = 0.3 T is 4 mm. Therefore, the electron density increased with magnetic field due to an increase in the confinement. The gyro-radius of charged species is inversely proportional to the magnetic field as given by eqn. (2.19). The increase in magnetic field decreases gyro-radius and eventually the confinement of plasma is enhanced. The increase in electron-neutral collisions decelerates the plasma considerably. However, a slight decrease in the electron density i.e. $(6.1 \pm 0.1) \times 10^{17}$ $cm^{-3}$ at $B$ = 0.5 T was observed. It could be due to an increase in the radial expansion along the field at higher magnetic field. It has been reported earlier that the radial expansion (along the magnetic field) of LPP in air increases with the increase in the magnetic field [69] and showed that it may be due to the spiral motion of the charge particles around the field lines. The other possibility is the increase in recombination which reduces the electron density. The electron temperature was determined using Boltzmann plot (Fig. 3.10). Fig. 3.11(b) shows the variation of electron temperature of the plasma as a function of magnetic field.

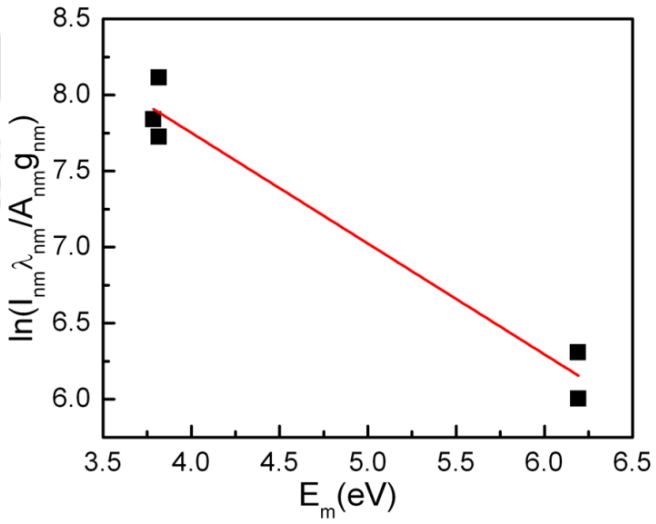


**Fig. 3.10.** Boltzmann plot at $B$ = 0.3 T.

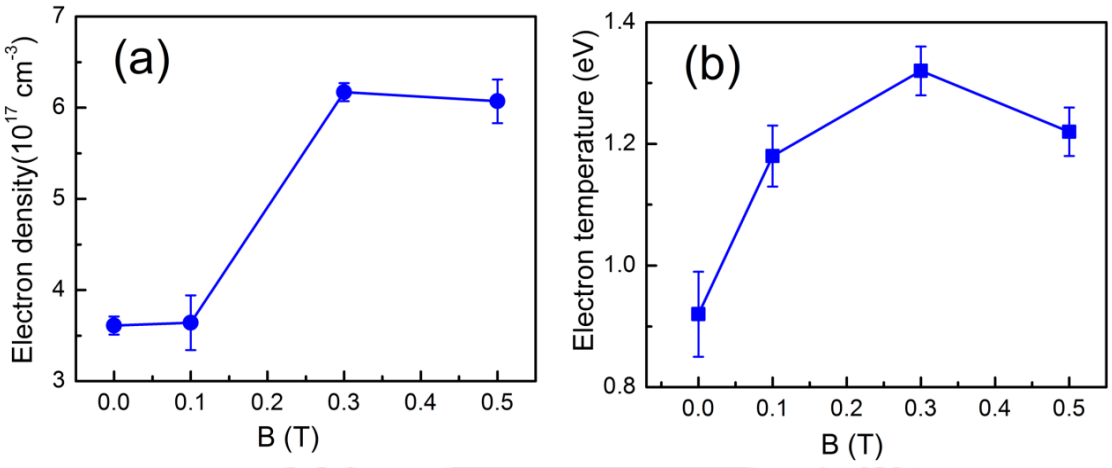


**Fig. 3.11.** Variation of (a) electron density and (b) electron temperature with magnetic field.

The electron temperature increased from (0.92 ± 0.07) eV up to (1.32 ± 0.04) eV with the increase in magnetic field from 0 to 0.3 T, respectively and then decreased to (1.22 ± 0.04) eV at higher value of $B$ = 0.5 T. The Joule's heating is directly proportional to the square of magnetic field.[149] As the magnetic field increased the Joule's heating also increased which in turn increased the electron temperature. The decrease in electron temperature at higher $B$ is due to an increase in the radial expansion along the field as well as more energy dissipation of electrons as a result of increased collisions with the atoms due to an increase in the plasma density.[55] The validity LTE of plasma is given by Mc Whirter's criterion (eqn. 2.11). In the present case, the value of $\Delta E_{mn}$ for Cu I (510.5 nm) is 2.43 eV and temperature is 15312 K at $B$ = 0.3 T. The lower limit of the plasma density satisfying the LTE condition is 2.84 × $10^{15}$ $cm^{-3.}$ The experimentally observed electron density of Cu plasma is of the order of $10^{17}$ $cm^{-3}$ which is greater than the lower limit of the validity condition of LTE. However, it is necessary condition but not sufficient. The validity

of LTE of copper plasma by considering the temporal and spatial evolution of plasma (sufficient conditions) is discussed in chapter 4.4

### 3.4. Conclusion

The time integrated OES of Cu plasma was investigated to estimate the optimized laser fluence and magnetic field. The laser fluence was varied from 7 to 21 $Jcm^{-2}$ at fixed 0.5 T magnetic field. The intensity of Cu I was enhanced in the presence of magnetic field. The enhancement is maximum at 14 $Jcm^{-2}$ at which the electron density and temperature is maximum. The intensity of Cu I decreased at higher laser fluence. The increase in electron temperature and density in the presence of magnetic field resulted in more ionization and hence the ion intensity. The magnetic field was then varied from 0 to 0.5 T at a fixed laser fluence of 14 $Jcm^{-2}$. The intensity enhancement of Cu I was also more pronounced at 0.3 T. The increase in electron density is attributed to the magnetic confinement of plasma. From this investigation, it is observed that the laser fluence and magnetic field play a key role in controlling the electron density and temperature of LPP in air. The intensity of spectral lines, irrespective of their nature, gets enhanced in the presence of magnetic field due to an increase in the collisional processes. Therefore, the laser fluence at 14 $Jcm^{-2}$ and magnetic field at 0.3 T were taken as optimized parameters which are also in good agreement with the results obtained from the studies on temporal evolution of plasma and laser ablation as discussed in chapter 4 and 5.

# Chapter 4

## *Studies on Temporal Evolution, Spatial Evolution, and Effect of Lens Focusing Distance on Cu Plasma in the Presence of Magnetic Field*

The dynamical behaviour of plasma studied by time integrated OES in chapter 3 was averaged over duration of one second. LPP is highly transient and it also evolves spatially. Most of the earlier studies on temporal evolution of plasma are in the vacuum or low pressure gas ambient and the temporal evolution of Cu plasma in the presence of magnetic field in air is not well documented. Therefore, the temporal evolution of Cu plasma produced was investigated by varying the strength of magnetic field. This method may be useful to make LPP as a controllable neutral beam source. The spatially-resolved OES of Cu plasma along the direction perpendicular to the target surface in the presence of both magnetic field and air is not available in the literature. It may be employed to improve the sensitivity of OES signal by optimizing the distance from target to reduce the continuum radiation in LIBS in air at atmospheric pressure. The continuum radiation generally occurs in the core region of plasma and it should be minimized to increase signal-to-noise ratio. The change in lens focusing distance leads to different behavior of plasma which in turn may change optical emission, PLD, drilling, and welding in the presence of the magnetic field. It is therefore imperative to study the effect of LTSD on LPP in the presence of magnetic field. This study may help in detailed understanding of the

effect of LTSD on emission of LPP and laser ablation in the presence of magnetic field in air at atmospheric pressure.

## 4.1. Experimental details

The detailed experimental setup was discussed in chapter 2. The laser fluence was fixed at 14 $Jcm^{-2}$ (optimized) to generate Cu plasma in air. The strength of magnetic field was varied from 0 to 0.5 T to study the temporal evolution of Cu I transitions and observed the maximum enhancement at 0.3 T. Therefore, further studies on the spatial evolution of plasma along the plasma expansion direction and the effect of lens focusing distance on plasma were done at a fixed magnetic field of 0.3 T and laser fluence of 14 $Jcm^{-2}$. For investigation of spatially-resolved plasma, the optical fibre was used to collect the radiation from plasma. With the help of translation stage the position of fibre was displaced from target surface along the plasma expansion direction at a step size of 1 mm to collect the radiation from different part of the plasma. The laser focusing lens was kept at different distances $d$ = -10, -5, 0, 5, and 10 mm, where $d$ is the distance between the target surface and the focal point of the lens.

## 4.2. Temporal evolution of Cu I transitions

### 4.2.1. *Determination of electron density and temperature*

The electron temperature was calculated from the Fourier transformed profile (wavelength domain) of the Cu I temporal profile using eqn. (2.13). The electron density was also calculated using FWHM of the Fourier transformed profile via line broadening method (eqn.2.15). The variation of electron density and temperature with magnetic field are shown in Fig. 4.1(a) and (b).

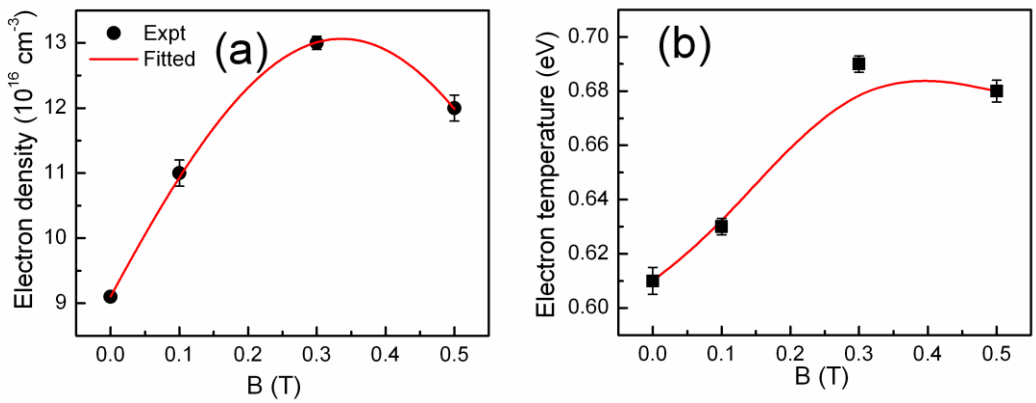


**Fig. 4.1.** Variation of (a) electron density and (b) electron temperature with magnetic field.

The electron density of LPP at 0, 0.1, 0.3, and 0.5 T are respectively, (9.1, 11.0, 13.0, and 12.0) × $10^{16}$ $cm^{-3}$. The corresponding electron temperatures are 0.61, 0.63, 0.69, and 0.68 eV, respectively. The increase in electron density and temperature can be understood as follows. The effective value of $\beta$ at lowest magnetic field of 0.1 T is 0.11 which indicates the confinement of plasma. However, it has been observed earlier that the plasma is considerably slowed down but it is not fully stopped by the magnetic field. It is attributed to incomplete exclusion of magnetic field from the plasma.[43,59] The confinement of plasma results in an increase in the plasma density. As mentioned in chapter 3, the increase in electron temperature in the presence of the magnetic field is due to adiabatic compression and Joule's heating. The increase in electron temperature is more likely due to increase in Joule's heating with magnetic field as it is directly proportional to the square of magnetic field.[149]

### 4.2.2. *Multi-structured temporal profile of Cu I transitions*

Three prominent Cu atomic lines, Cu I (510.5 nm), Cu I (515.3 nm), and Cu I (521.8 nm) were used to investigate the effect of the magnetic field on temporal

behavior of Cu I line. The experimentally recorded temporal profiles at magnetic field $B$ = 0, 0.1, 0.3, and 0.5 T are shown in Fig. 4.2(a), (b), and (c), respectively. The temporal profile showed multi-structure of each Cu I transitions. As observed from temporal profiles, each transition responds to the magnetic field differently. A remarkable difference in the structures of the Cu I profile was observed when the magnetic field was increased to 0.3 and 0.5 T. To gain more insight about the processes involved in the formation of the multi-structure of the experimentally observed temporal Cu I profile, further analysis was also done by using multiple-peak fitting (deconvolution). The temporal profile of atomic transition of LPP in vacuum (or low pressure) is usually fitted with the shifted Maxwell-Boltzmann (SMB) distribution.

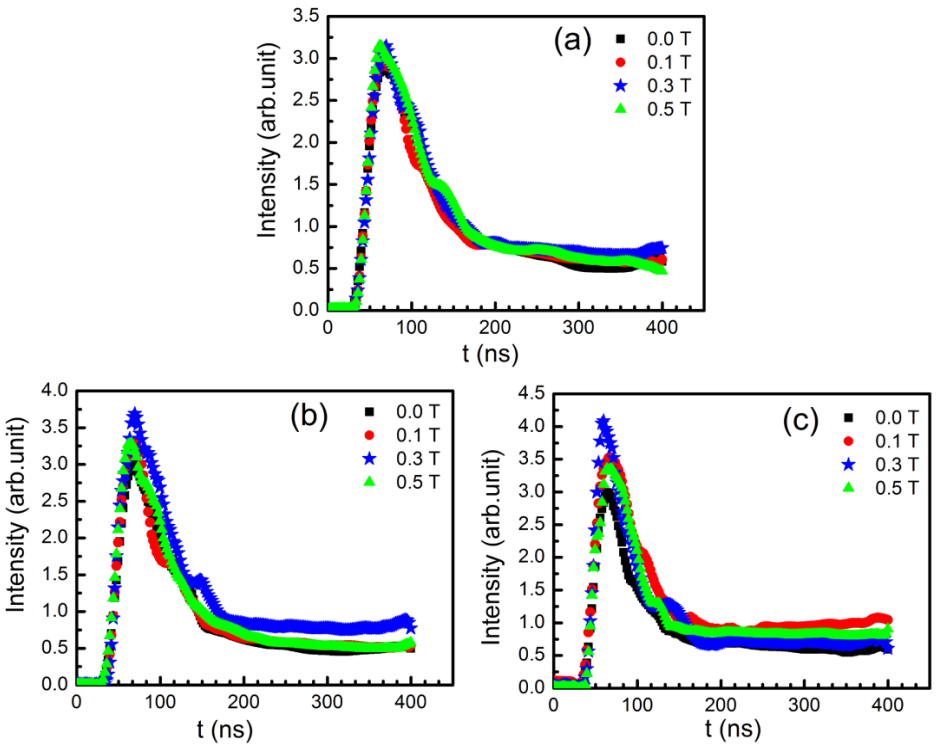


**Fig. 4.2.** Cu I temporal profiles with $B$ = 0 - 0.5 T: (a) 510.5 nm, (b) 515.3 nm, and (c) 521.8 nm.

However, Singh et al. reported that at high background pressure the kinetic distribution of the neutral species transforms from SMB to Gaussian distribution.[150] Experiments have already shown earlier that at low pressure the kinetic distribution of the plasma species deviates from the Maxwell – Boltzmann distribution due to less collision. However, at atmospheric or higher pressure the distribution is given by Boltzmann distribution.[37] Fig. 4.3(a) – (d) show multiple-fitted Cu I (510.5 nm) temporal profiles at $B$ = 0, 0.1, 0.3, and 0.5 T, respectively. Similarly, Fig. 4.4 and 4.5 show the multiple-fitted Cu I (515.3 nm) and Cu I (521.8 nm) at $B$ = 0, 0.1, 0.3, and 0.5 T, respectively. The evolution of Cu I temporal profile is attributed to the electron-impact excitation of atom.

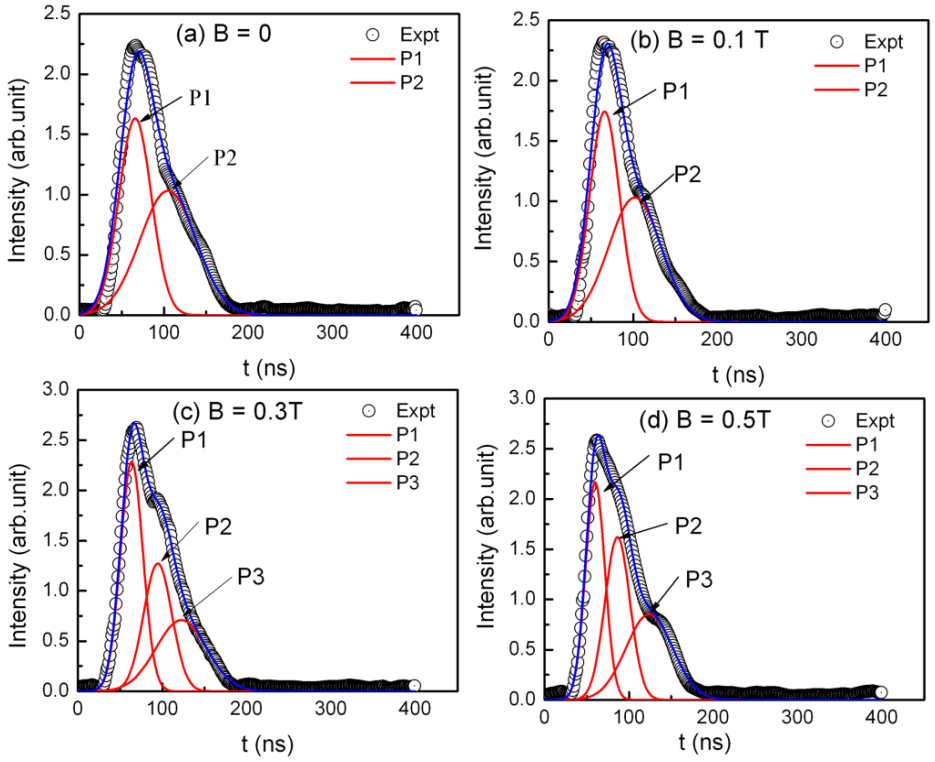


**Fig. 4.3.** Multiple-fitted temporal Cu I (510.5 nm) profiles at (a) 0 T, (b) 0.1 T, (c) 0.3 T, and (d) 0.5 T.

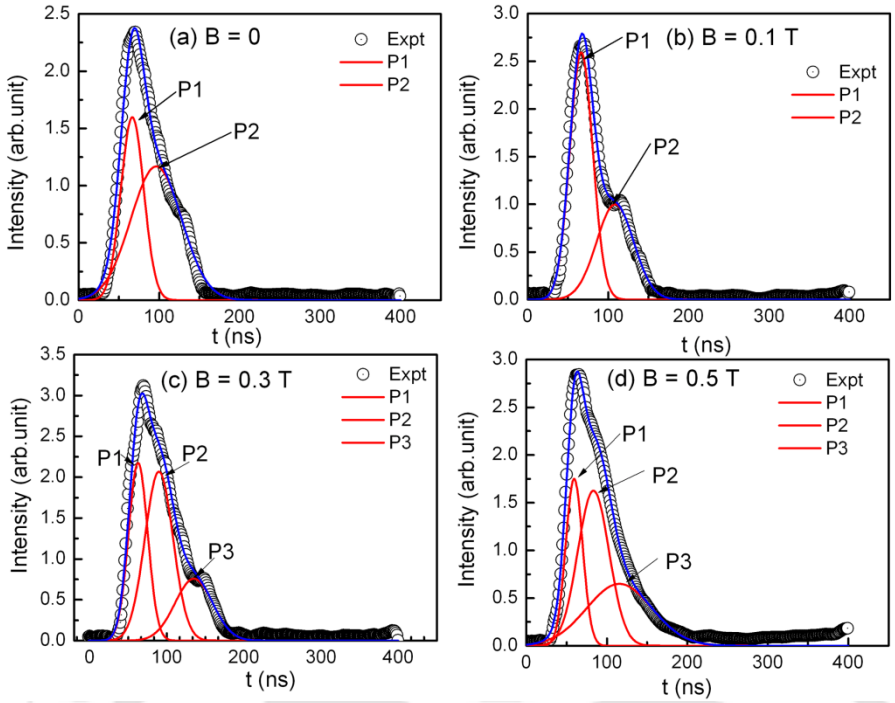


**Fig. 4.4.** Multiple-fitted temporal Cu I (515.3 nm) profile at (a) 0 T, (b) 0.1 T, (c) 0.3 T, and (d) 0.5 T.

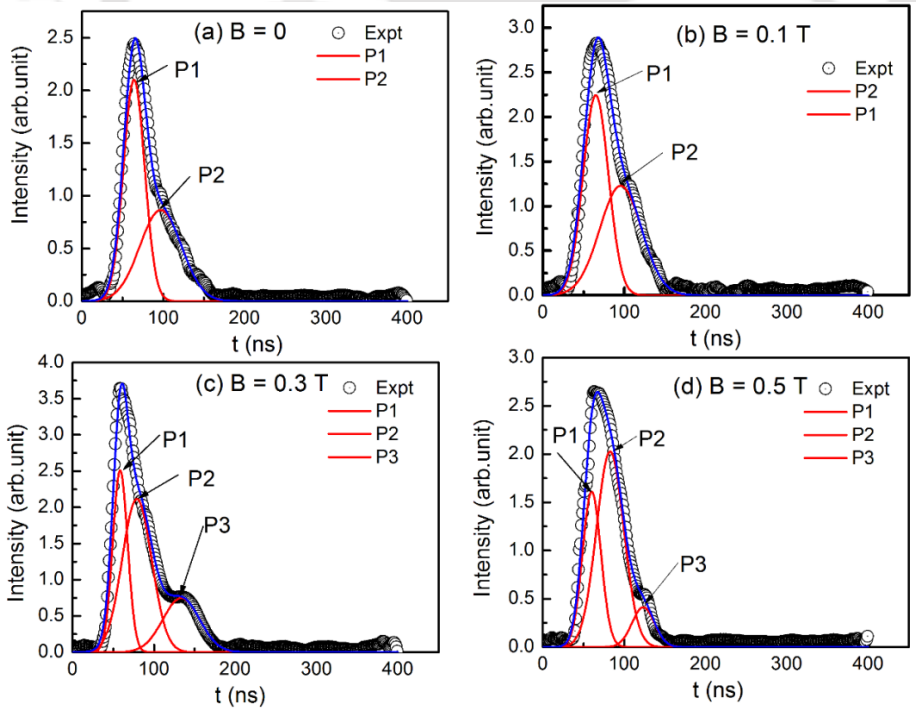


**Fig. 4.5.** Multiple-fitted Cu I (521.8 nm) temporal profile at (a) 0 T, (b) 0.1 T, (c) 0.3 T, and (d) 0.5 T.

In addition to electron impact excitation, other phenomena of interest such as (i) backflow of particles towards the target as a result of collapse of diamagnetic cavity, and (ii) instability in plasma which may likely contribute to the generation of multiple-structure of temporal profile are also discussed as follows. Harilal et al. reported the appearance of Al I temporal profile twin structures in laser-produced Al plasma in vacuum in the presence of magnetic field of 0.6 T and attributed to the back flow of particles towards the target as a result of collapse of diamagnetic cavitation.[45] The formation of diamagnetic cavitation in LPP in the presence of magnetic field has also been reported earlier.[17, 25–27] The formation of the diamagnetic cavitation can be seen as follows. The initial laser impact on the target creates immediate ionization of surface atoms and the produced electrons and ions expand abruptly. In the presence of magnetic field, the electrons and ions gyrate in opposite directions with different Larmor radii. Since the Larmor radius of the ion is much larger than that of electron, the ions overshoot the electrons and form a layer of ion in the boundary of the plasma plume. The electrons are pulled back across the magnetic field to neutralize the ions creating radially inward electric field which in turn produces an electron drift **E**×**B** which expels out the magnetic field. The diamagnetic cavity expands until the excluded magnetic energy is comparable to the total plasma energy. By assuming the plasma expansion to be hemispherical, a typical diamagnetic cavity or stopping radius ($R_b$) can be determined from the conservation of energy and is given by eqn. (2.22). The plasma is decelerated strongly near the stopping radius. The average deceleration of the plasma plume is given by ($g = v^2/2R_b$), where $v$ is the expansion velocity of plasma. The expansion velocity was determined from the relation[153] $v \propto I_L^{0.2}$ where $I_L$ is the absorbed laser intensity and it was found to be around $10^6$ cm/s. The

deceleration at $B$ = 0.1, 0.3, and 0.5 T is (1.3, 2.7, and 3.9) $\times 10^{12}$ cm/s$^2$, respectively. The backflow of particles happens when the splitting of temporal profile appears at longer time than the diamagnetic cavitation bubble time.[45] The bubble radius was estimated and found to be 9.7 mm at $B$ = 0.1 T. Therefore, the bubble time ($2R_b/v$) is approximately 1200 ns. Similarly, the bubble time at $B$ = 0.3 and 0.5 T is, respectively, 580 and 412 ns. The components (P1, P2, and P3) of all three Cu lines originated before the bubble time in all magnetic field conditions. Therefore, the contribution of particles back flow due to collapse of diamagnetic cavity in the generation of multi-structure is ruled out. It is reported that emission profiles of neutrals and ions show distinct structures when the magnetic field is introduced in LPP. It is attributed to the plasma instabilities.[154,155] The self-generated magnetic field estimated from the relation[34] $B \leq (kT_e / ezv)$ at $z$ = 9 mm is found to be 22 G which is much less than the applied lowest magnetic field 0.1 T (1000 G). Therefore, the instability due to interaction between the self-generated magnetic field and applied magnetic field cannot be correlated to the formation of multi-structure formation. In the case of high plasma pressure (high-$\beta$), the plasma "punches" its way across the magnetic field (RT instability).[44,156–158] It is also shown that the RT instability requires the magnetization of ions.[159,160] The Larmor radius of ion and electron at $B$ = 0.5 T is $1.8 \times 10^5$ and 2.1 cm, respectively. The Larmor radius of ion is larger than the plume dimension (approximately 6 mm), the ion is not magnetized. From the plasma snapshot images captured using CCD (Fig. 4.6), the dimension of the plasma plume at $B$ = 0.5 T was measured to be approximately 6 mm. The RT instability growth at the interface between the plasma (density = $\rho_1$) and ambient gas (density = $\rho_2$), is given

by $\omega^2 = -kg_{RT}\frac{(\rho_1-\rho_2)}{(\rho_1+\rho_2)}$, where $g_{RT}$ is the acceleration of the contact boundary. The plasma boundary is stable if $\omega^2 > 0$ and if $\omega^2 < 0$, the perturbation grows exponentially.[44]

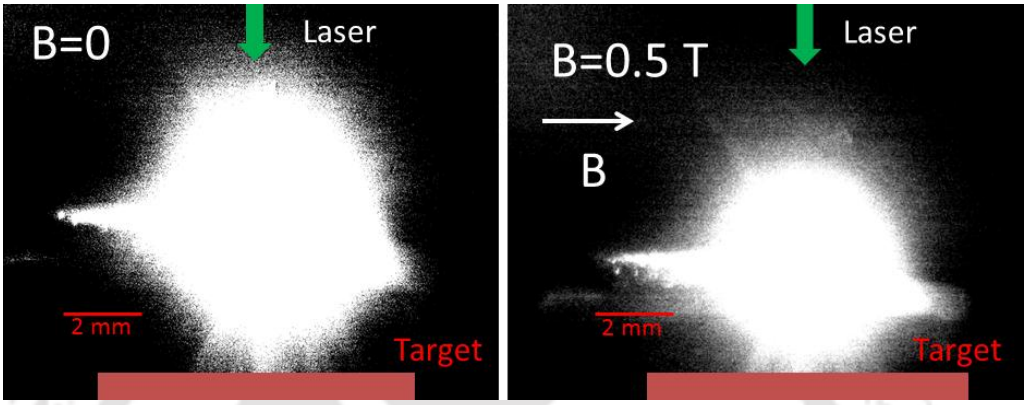


**Fig. 4.6.** CCD image of laser produced copper plasma at (a) $B$ = 0 and $B$ = 0.5 T.

The plasma density was found to be around $10^{16}$ $cm^{-3}$ and the air ambient corresponds to around $10^{19}$ $cm^{-3}$, therefore, it satisfies the stable condition. From the overall discussion, the contribution of RT instability (or density fluctuation) in generation of the multi-structure of temporal profile is not validated. It has also been reported earlier that the oscillatory structure is not observed in LPP though it is observed in laser-blow-off plasma.[161] Therefore, the formation of multi-structure of Cu I line in the presence of magnetic field is more likely due to electron impact excitation as discussed later. When the plasma kinetic energy is equal to the magnetic energy, the instability is generated in the plasma and this instability reduces spectral line intensity. From this study, it can be concluded that in the presence of magnetic field and air at 1 atm pressure, the instability can be reduced which will help to enhance the spectral line intensity in LIBS. Kim et al. also observed, recently, that at

air pressure (760 torr), the intensity enhancement of spectral line in LPP is observed at low energy (30 mJ).[72] From Fig. 4.3, 4.4, and 4.5, it was observed that at $B$ = 0 and 0.1 T, each temporal atomic profile consists of two components P1 and P2. During laser pulse, the plasma consists of significant fraction of high-lying excited atoms due to direct ablation. The first component P1 is generated by either direct laser ablation or the radiative cascade from the highly excited states which populates the low lying radiative excited states. At $B$ = 0 T, the plasma expands in air ambient by pushing out the air molecules. As plasma plume expands, the kinetic energy of the plasma decreases and eventually the plasma is decelerated by air pressure and confined into smaller region. Also due to adiabatic compression, the temperature of the plasma is increased. The higher electron density and temperature favours the increase in electron-impact excitation which generates the component P2 (around 100 ns after the laser pulse) at $B$ = 0. It has also been shown earlier that at low pressure the temporal profile of Al plasma species is described by a single distribution. But as the pressure increases, the temporal distribution showed twin structure.[30] In the presence of lower magnetic field of 0.1 T, the temporal atomic profile consists of only two peaks (P1 and P2). In the presence of magnetic field, the effect of magnetic field appears in the LPP in addition to confinement effect of air pressure (as mentioned above). As the plasma plume expands, the plasma temperature decreases and eventually at a delayed time (in non-diamagnetic limit) e.g. 580 ns at $B$ = 0.3 T the magnetic field diffuses across the plasma boundary. The diffusion coefficient ($D$) of the plasma perpendicular to the magnetic field is given by $D \propto 1/B^2T^{1/2}$.[162] The increase in temperature and magnetic field will reduce the diffusion across the magnetic field and eventually the

plasma plume expansion is decelerated. The magnetic diffusion time ($\tau_d$) is given by[163] $\tau_d = \frac{4\pi\sigma_{spitz}R_b^2}{c^2}$ where $\sigma_{spitz}$ is the Spitzer conductivity of the plasma. The magnetic diffusion time ($\tau_d$) was essentially the time required to convert field energy into Joule's heating. It can also be interpreted as time for annihilation of magnetic field. The magnetic diffusion time is calculated for the magnetic field $B$ = 0.1, 0.3, and 0.5 T as shown in table 4.1. As the magnetic field was increased, the diffusion time decreased. Therefore, the time required to convert the magnetic energy into Joule's heating is lower in higher magnetic field. The diffusion time at $B$ = 0.1 T was 180.4 ns. The Joule's heating due to presence of magnetic field occurred 102 and 58 ns after the generation of components P1 and P2, respectively. Therefore, these two components are least affected by 0.1 T magnetic field. It was also observed that at $B$ = 0 and 0.1 T, the P3 component was not observed.

**Table 4.1.** Magnetic diffusion time.

| Sl. No. | B (T) | $\tau_d$(ns) |
|---|---|---|
| 1 | 0.1 | 180.4 |
| 2 | 0.3 | 41.5 |
| 3 | 0.5 | 21.0 |

Since $T_e$ and $n_e$ are proportional to the $t^{-1}$ and $t^{-2}$ respectively[67], the electron temperature and density at delayed time of 122 ns were decreased to $T_e$/122 and $n_e$/(122)$^2$ which essentially leads to decrease in electron-impact excitation rate considerably. However, when the magnetic field was increased from 0.1 to 0.3 T, the component P3 e.g. P3 of Cu I (521.8 nm) was generated at 122 ns. The generation of

third component at $B$ = 0.3 T was a very significant observation. This P3 of Cu I (521.8 nm) position was shifted to 123 ns when the magnetic field was increased to 0.5 T. This shows that the appearance of third component P3 at delay time 122 ns was purely induced by magnetic field as the magnetic field does not affect the initial plasma formation processes.[55] When the magnetic field was increased, the confinement was more pronounced due to increase in magnetic pressure. As the magnetic field increased, the Larmor radius (eqn. (2.19)) was smaller and eventually the frequency of electron-atom collision was increased.[55] The increase in electron-atom collision rate and plasma temperature results in increase in electron-impact excitation rate. The magnetic diffusion time at $B$ = 0.3 T was 41.5 ns i.e. the Joule's heating on plasma due to magnetic field started within 41.5 ns. Within the time delay of 41.5 ns (i.e. initial stage of plasma expansion), the density of plasma was very high. The heating on high density plasma provides more electron-atom interaction than the low density plasma (i.e. 180.4 ns) which eventually generates the third slow component P3. Therefore, the P3 appeared at higher magnetic field of 0.3 and 0.5 T but not at 0.1 T. The component P3 of Cu I (510.5 and 515.3 nm) was also generated by the same process. Kumar et al. reported the multiple structures of neutral line of laser-produced lithium plasma in the presence of magnetic field in vacuum or gas ambient condition and attributed to atomic processes.[67] Raju et al. reported that the fast component P1 originates due to the radiative cascade from the highly excited states which populates the low lying radiative excited states and the slow components is attributed to the collisional excitation, mainly due to the electron-impact excitation from low lying states.[55]

### 4.2.3. *Intensity variation of Cu I temporal profiles with magnetic field*

Fig. 4.7(a) shows the variation of the integrated intensity of Cu I line as a function of magnetic field. It was observed that as magnetic field was increased the intensity of the Cu I transition initially increased up to 0.3 T and then decreased on further increased in magnetic field to 0.5 T. In order to understand this variation with magnetic field, the intensity variation of each component of all three transitions with magnetic field was studied. Fig. 4.7(b), (c), and (d) shows the intensity variation (P1, P2, and P3) of Cu I (521.8, 515.3 and 510.5 nm), respectively. The fast component P1 intensity of all three Cu I transitions was almost constant when the magnetic field was increased from 0 to 0.3 T (insignificant effect of magnetic field). However, P1 intensity of Cu I (510.5 and 515.3 nm) decreased when the magnetic field was further increased to 0.5 T while the component P1 of Cu I (521.8 nm) increased. The component P2 intensity of Cu I (521.8, 515.3 and 510.5 nm) was slightly increased when the magnetic field was increased from $B$ = 0 to 0.1 T. The P2 intensity of Cu I (515.3 and 510.5 nm) increased abruptly when the strength of magnetic field was switched to 0.3 T and then decreased when on further increased in magnetic field to 0.5 T. The P2 intensity of Cu I (521.8 nm) decreased gradually when the magnetic field was increased from 0.1 to 0.5 T. It was clear that the slow component P2 is more affected by magnetic field as compared to the fast component P1 in all cases of the three transitions. The component P3 appeared at $B$ = 0.3 and 0.5 T. However, the P3 intensity of Cu I (515.3 and 510.5 nm) increased when the magnetic field increased from 0.3 to 0.5 T while P3 intensity of Cu I (521.8 nm) decreased. The increase in intensity of P3 for low excited energy states (510.5 nm and 515.3 nm) is due to increase in electron-impact excitation rate from lower states and the decrease in P3

intensity of Cu (521.8 nm) is due to increase in ionization of atom lying in the upper state of Cu (521.8 nm). Fig. 4.8 shows the enhancement factor (EF) of P1, P2, and integrated intensity (P1+ P2 + P3) with magnetic field. The EF of P1 of all three Cu I transitions remained almost constant up to 0.3 T which is attributed to least affected by magnetic field on P1. As the magnetic field was increased from 0.3 to 0.5 T, the confinement of plasma plume and Joule's heating was increased and the magnetic diffusion time was also lowered from 41.5 to 21.0 ns. It resulted in an increase in the electron-impact excitation rate which in turn increased the excitation of low-lying excited atoms to high-lying excited state.

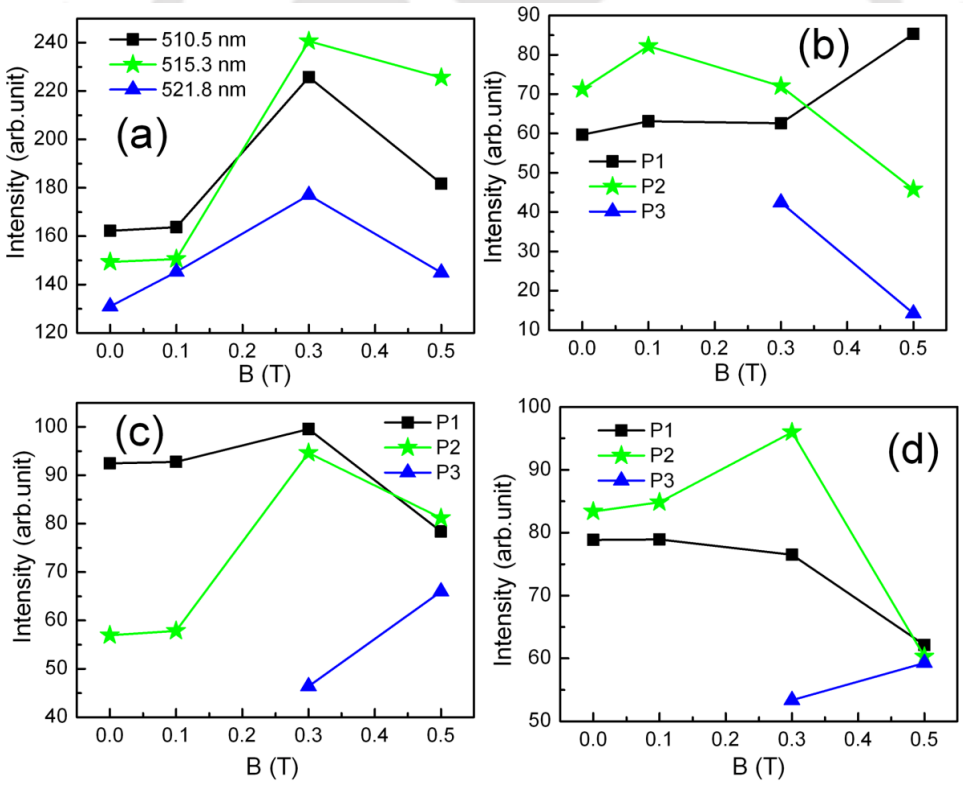


**Fig.4.7.** Variation of Cu I intensity with magnetic field: (a) integrated intensity (510.5 , 515.3, 521.8 nm), component peaks (b) 521.8 nm, (c) 515.3 nm, and (d) 510.5 nm.

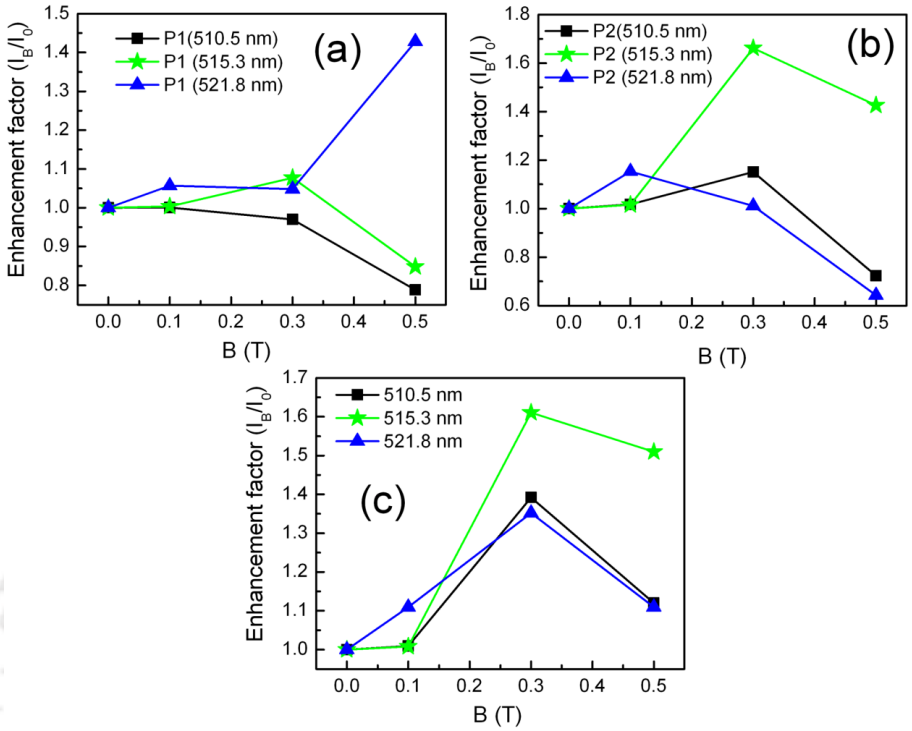


**Fig 4.8.** Variation of EF with magnetic field: (a) P1 (510.5, 515.3, 521.8 nm), (b) P2 (510.5, 515.3, 521.8 nm), and (c) P1+P2+P3 (510.5, 515.3, 521.8 nm).

It explains the increase in EF of high lying excited atom transition P1 (521.8 nm) while that of low-lying excited atom transitions P1 (515.3 and 510.5 nm) decreased at higher magnetic field. It has been reported earlier that the generation of high energy-excited Cu atoms is at the expense of the low energy excited atoms through collisional excitation process by hot electrons.[164] The EF of P2 was found to increase when the magnetic field was increased from 0 to 0.3 T and then decreased on further increase in the magnetic field. The EF in integrated intensity of each transition increased with the magnetic field up to 0.3 T and then decreased on further increase in the magnetic field (0.5 T). The decrease in EF (P1+P2+P3) at higher magnetic field is due to overall decrease in total intensity contributed by each fractional component.

The different EF is due to different rate of electron-impact excitation of copper atom. The excitation rate coefficient is obtained from eqn. (2.4). The electron density times the excitation coefficient gives the rate of electron impact excitation of copper atom. The variation $n_e$ with $B$ is fitted with the function $n_0 e^{a+bB-cB^2}$ (i.e. $n_e = n_0 e^{a+bB-cB^2}$ ), where $a$, $b$, and $c$ are parameters and found to be $a$ =2.2, $b$ =2.1, and $c$ = 3.2 and $n_0$ = $10^{16}$ $cm^{-3}$. By inserting the value of $n_e$ in eqn. (2.4), the electron impact excitation rate can be calculated in terms of $B$.

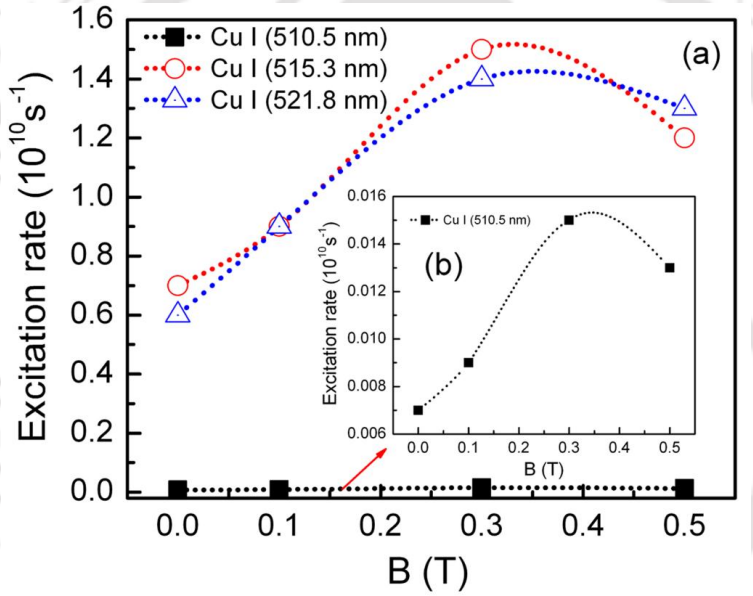


**Fig. 4.9.** Variation of electron impact excitation with magnetic field: (a) Cu I (510.5 nm), Cu I (515.3 nm), Cu I (521.8 nm), and (b) Enlarged view of Cu I (510.5 nm).

Fig. 4.9 shows the electron impact excitation rate of Cu I as a function of magnetic field. At $B$ = 0.3 T, the electron impact excitation rate of Cu I (515.3 nm) was highest which resulted in highest enhancement factor among three neutral lines in the presence of magnetic field. This shows that the difference in enhancement factor is due to different electron impact excitation rate for each transition. The oscillator

strength of the three transitions is taken from NIST database.[124] Owing to large collisional excitation rate of Cu I (515.3 nm), more electrons are populated to higher state $^2D_{3/2}$ via electron-impact excitation. The Cu I (515.3 nm) is more enhanced at $B$ = 0.3 T as a result of excitation of more electrons due to confinement of plasma by the magnetic field to the small region. However, Cu I (521.8 nm) has minimum EF though its electron impact excitation rate is larger than Cu I (510.5 nm). It is attributed to an increase in the ionization of Cu I (521.8 nm) due to increase in temperature and density as a result of magnetic confinement of the plasma.

## 4.3. Spatial evolution of Cu plasma along the expansion direction in the presence of magnetic field

### 4.3.1. *Spatial evolution of Cu plasma and calculation of stopping radius*

The emission spectra of the laser-produced copper plasma were recorded in the wavelength range 506 – 523 nm at axial distance from $z$ = 0.5 to 6.5 mm from the target in the absence and presence of the magnetic field. Fig. 4.10 shows the spatially-resolved optical emission spectra of laser-produced Cu plasma in the absence and the presence of magnetic field of 0.3 T, respectively. The Cu I and Cu II transitions were observed in the emission spectra but higher ionized line (Cu III) was not observed. The three strong atomic lines: Cu I (510.5 nm), Cu I (515.3 nm), and Cu I (521.8 nm) and one ionic line Cu II (508.8 nm) were used to study the spatial behavior of plasma along expansion direction in the absence and presence of magnetic field. Fig. 4.11 shows the emission spectra at $B$ = 0 and 0.3 T at the axial distance $z$ = 3.5 mm from the target. From the spectra recorded it was observed that in the presence of 0.3 T

magnetic field the intensity of both Cu I and Cu II transition is higher than that of without magnetic field.

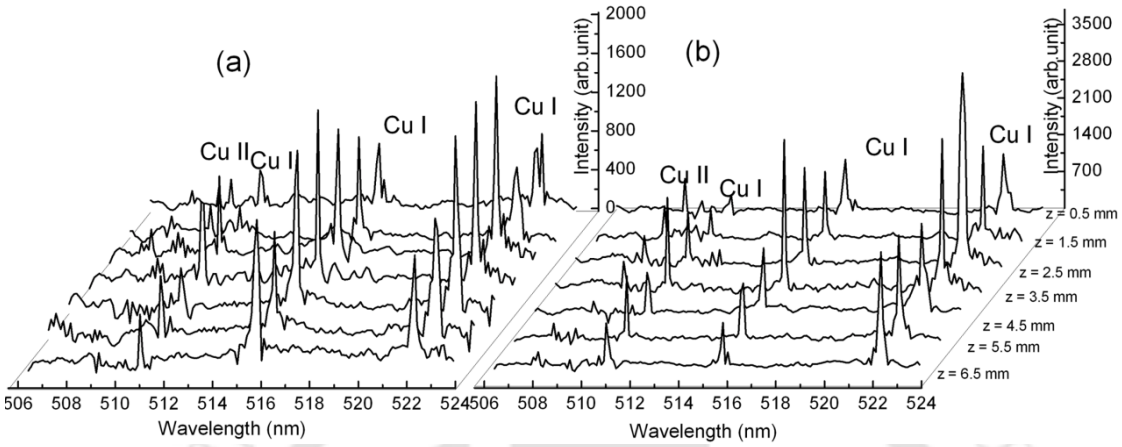


**Fig. 4.10.** Spatial evolution of copper plasma optical emission spectra at (a) $B = 0$ and (b) $B = 0.3$ T.

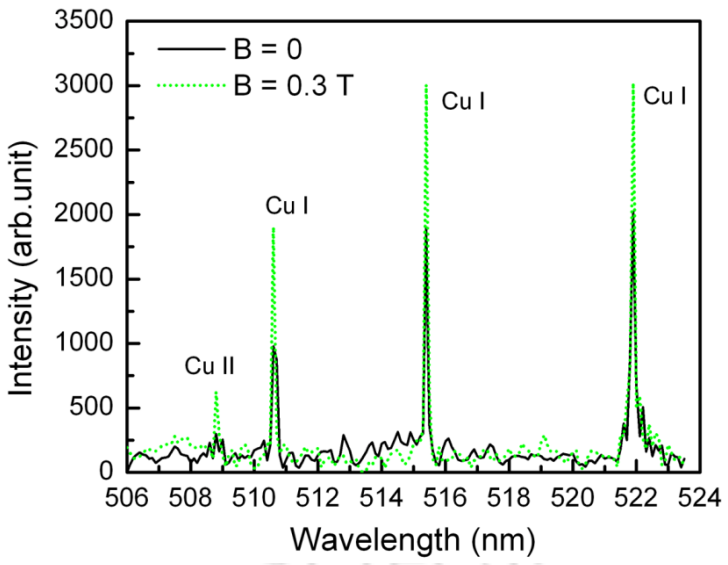


**Fig. 4.11.** Optical emission spectra of copper plasma at $B = 0$ (smooth line) and $B = 0.3$ T (dotted line) at a distance of 3.5 mm from the target surface.

The increase in intensity is discussed later. Cristoforetti et al. have reported that at laser intensity less than $8 \times 10^8$ Wcm$^{-2}$, the plasma produced is from the target

only and not from ambient gas[73] and the plasma expansion follows the laser-supported combustion wave (LSC). The laser intensity on the target was $6.0 \times 10^8$ $Wcm^{-2}$ (after considering the reflectance of copper). The plasma generated was only copper plasma and it expands like a piston pushing out the air molecules.The plasma expansion is considered to be as LSC. In this regime, the compressed (shocked) ambient air remains transparent for laser and air breakdown does not occur. At this condition there is no intermixing between copper and air plasma in initial stage of plasma formation.

When the plasma expands in an external magnetic field, its expansion is decelerated due to magnetic pressure. Eventually, it stops when the magnetic energy is approximately equal to kinetic energy of plasma expansion.[43,58,59] The stopping radius ($R_b$) was estimated from eqn. (2.22). The reflectance of Cu at 532 nm laser wavelength is 61 %.[165] Therefore, the absorbed laser energy is 15.6 mJ for 40 mJ laser energy impinging on the target. In the presence of magnetic field of $B$ = 0.3 T and $E_L$ = 15.6 mJ, the calculated value of $R_b$ is 4 mm which is in good agreement with the experimentally recorded spectrum at $z$ around which the intensity is more pronounced. The initial velocity of expansion under the same experimental parameters condition of present work is discussed elsewhere [126] and it is approximately $1.6 \times 10^6$ cm/s. Therefore, the deceleration of plasma in the combined effect of magnetic field and air pressure is $3.2 \times 10^{12}$ $cm/s^2$. The atomic spectral line was observed even beyond 4 mm which shows that the plasma is decelerated considerably by magnetic field but not fully stopped at the stopping radius. It could be due to incomplete exclusion of magnetic field inside the plasma and assumption of the plasma as having spherical shape[43]. At axial distance $z$ = 3.5 mm from Cu target, the electron density and

temperature were $6.09 \times 10^{16}$ $cm^{-3}$ and 0.85 eV, therefore, the thermal pressure of the plasma was $8.3 \times 10^{3}$ $Nm^{-2}$ whereas the magnetic pressure was $3.6 \times 10^{4}$ $Nm^{-2}$ which is larger than the thermal plasma pressure ($\beta < 1$). Since the magnetic pressure is larger than the thermal plasma pressure, the plasma is decelerated and confined which is in good agreement with the discussion in section 4.2.1.

### 4.3.2. *Spatial evolution of electron density and temperature along z*

Fig. 4.12 shows the electron density variation as a function *z* (axial distance) from the copper target. The electron density varies from (9.9 ± 0.3) to (4.9 ± 0.1) × $10^{16}$ $cm^{-3}$ when the distance (*z*) varied from 0.5 to 6.5 mm. In the presence of magnetic field, it varied from (10.9 ± 0.4) to (4.8 ± 0.1) × $10^{16}$ $cm^{-3}$. The electron density decreased as *z* was increased from 0.5 to 6.5 mm. The electron density determined from experimental spectral line is fitted with power law ($n_e = bz^a$ where *a* and *b* are fitting parameters). In the absence of magnetic field, the electron density varied as $n_e = 9.2z^{-0.33}$ and in the presence of 0.3 T magnetic field, it varied as $n_e = 7.9z^{-0.27}$. The electron density in laser-produced zinc and cadmium plasma in the absence of magnetic field followed the same trend as observed in present work.[166,167] However, in the presence of magnetic field the electron density decayed slowly than without magnetic field. At larger *z* from the target, due to decrease in temperature, the electron-ion recombination increased which resulted in decrease in the electron density and hence plasma-magnetic field interaction. The electron density is more or less the same within the distance between 4.5 to 6.5 mm. The electron density gradient is very high near the target surface and it is less in the presence of magnetic field. It is attributed to the magnetic confinement of plasma which decelerates the expansion of the plasma. Harilal et al.[45] reported that the expansion laser-produced Al

plasma is decelerated significantly in the presence of magnetic field using imaging and spectroscopy technique. It is attributed to increase in collisions in magnetically confined plasma which causes slowing of atomic species though it is not directly affected by the magnetic field.

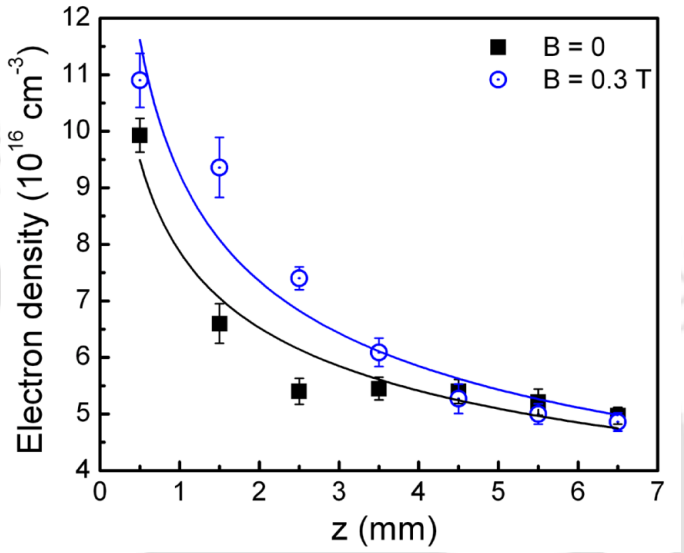


**Fig. 4.12.** Electron density variation with *z* at *B* = 0 and 0.3 T.

Fig. 4.13 shows the electron temperature variation along the plasma expansion direction (*z*). The electron temperature varied from (1.10 ± 0.02) to (0.61 ± 0.01) eV when the distance (*z*) was increased from 0.5 to 6.5 mm. But it varied from (1.20 ± 0.02) to (0.67 ± 0.02) eV when the magnetic field of 0.3 T was applied. The temperature near the target was higher. The region near the surface absorbs laser energy during the laser pulse through IB process. In the presence of magnetic field, the electron temperature was higher up to distance 4.5 mm due to confinement of plasma and beyond 4.5 mm it was comparable with that of without magnetic field. In confined state of plasma, due to adiabatic compression of plasma and Joule's heating, the electron temperature is higher. The electron temperature decreased when the *z*

increased due to expansion of the plasma. Similar to the electron density variation, the variation of electron temperature with $z$ was fitted with power law. At $B$ = 0 T, the electron temperature varied as $T_e = 1.1z^{-0.23}$ whereas it varied as $T_e = 0.9z^{-0.18}$ in the presence of the magnetic field. Similarly, Shaikh et al. reported that the electron density along the plasma expansion direction in laser-produced zinc plasma in air varies as $T_e \sim z^{-0.20}$. This shows that the electron temperature in the absence of magnetic field decreases faster than in the presence of magnetic field.

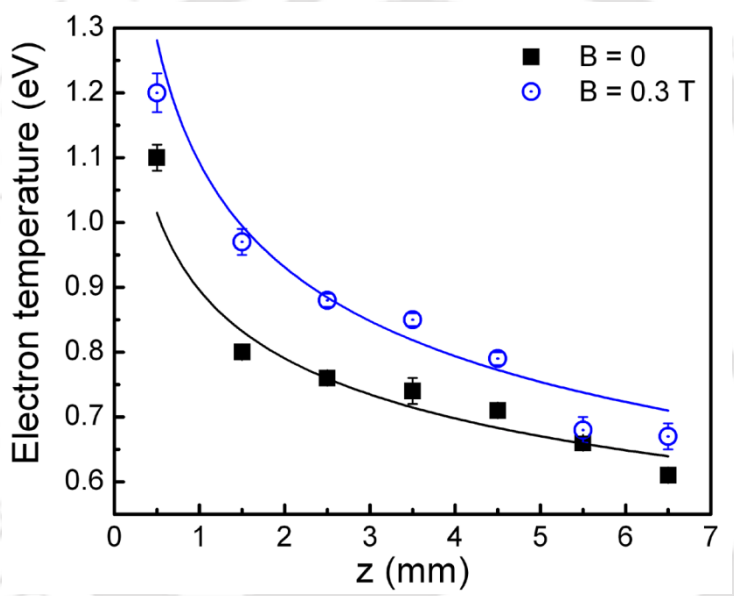


**Fig. 4.13.** Electron temperature variation with $z$ at $B$ = 0 and 0.3 T.

The magnetic field threading through the plasma was also determined at different region of the plasma along the direction of plasma expansion using the relation[131] $p + \frac{B_0^2}{2\mu_0} = \frac{B^2}{2\mu_0}$ where $p$ is plasma thermal pressure, $B$ is magnetic field at plasma boundary, and $B_0$ is magnetic field diffusing in plasma, respectively. Fig. 4.14 shows the variation of $B_0$ with $z$. As the plasma expands the plasma density and

temperature decreases which results in decrease in plasma thermal pressure. Therefore, the magnetic field diffuses into the plasma and it approaches the non-diamagnetic regime as the distance from the target increased. From the spatial evolution of plasma electron density and temperature, the approximate dimension of core and tail of the LPP can be determined.[77] Within core region the electron density and temperature decreases rapidly with distance from the target surface and the region where electron density and temperature decreases slowly is known as tail of the plasma.

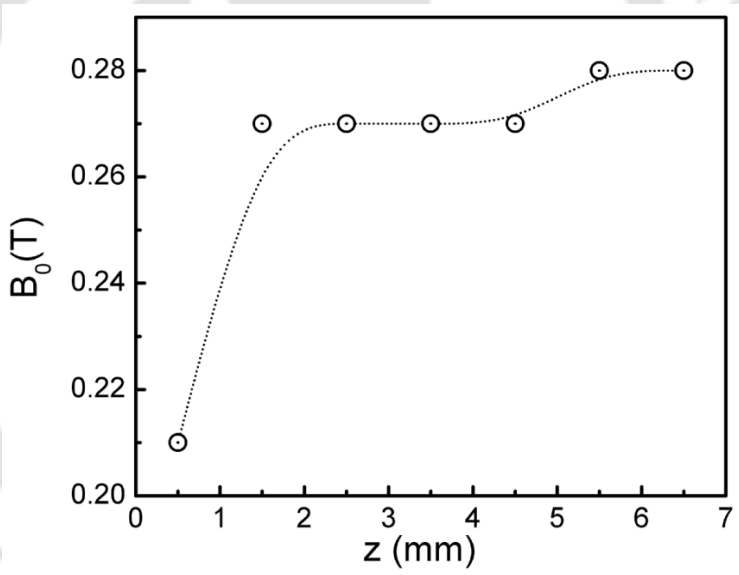


**Fig. 4.14.** Variation of magnetic field threading inside plasma ($B_0$) with $z$.

It was observed that in the absence of magnetic field, the electron density and temperature decreased rapidly up to 2.5 mm with distance from target surface and then decreased slowly beyond 2.5 mm. Therefore, the approximate dimension of the core is taken 2.5 mm. Interesting observation was the change in core dimension in the presence of magnetic field of 0.3 T. The dimension of the core in the presence of

magnetic field of 0.3 T was found to be around 4.5 mm and thereby decreased the size of the tail of LPP. The increase in size of core region in the presence of magnetic field is due to increase in temperature as a result of heating in plasma by Joule's heating effect, shock formation, and magnetic compression.[168] In the shock formation and magnetic compression, the electron temperature is proportional to $n_e^{2/3}$. The electron density in the presence of magnetic field of 0.3 T is higher than the absence of magnetic field which increases temperature in the presence of magnetic field. The increase in temperature leads to more ionization and thus increases the dimension of the core. The other possibility is the increase in thermal conductivity of plasma with magnetic field. The plasma thermal conductivity was determined in the absence and presence of magnetic field using the following relations[168], $k = 9.0\times10^{9}\left(\frac{Te^{5/2}}{Z}\right)$ and $k_{mag} = 1.1\times10^{-11}\left(\frac{n_e^{2}Z}{B_0^{2}T_e^{1/2}}\right)$, where $k$ and $k_{mag}$, are the plasma thermal conductivities in the absence and presence of magnetic field, respectively. In the presence of magnetic field, the conductivity is higher than the absence of magnetic field. For instance, plugging the values of $T_e$, $n_e$, and $B_0$ at $z$ = 3.5 mm in above equations, $k = 4.24 \times 10^{19}$ $cm^{-1}s^{-1}$ and $k_{mag} = 6.07 \times 10^{23}$ $cm^{-1}s^{-1}$. In the light of this example, thermal conductivity of LPP is increased in the presence of magnetic field. As a result of this, more heat is transferred from core to tail region of LPP which may increase the size of core in the presence of magnetic field.

### 4.3.3. *Variation of intensity of Cu I and Cu II transitions with z*

Fig. 4.15 shows the variation of intensity along axial distance $z$ in the absence and presence of magnetic field and is discussed as follows.

**A. In the absence of magnetic field**

(i) **Cu I (510.5 nm)**: As *z* was increased from 0.5 to 3.5 mm the intensity initially increased and then decreased at *z* = 4.5 mm. At z = 5.5 mm, the intensity again slightly increased and then decreased at *z* = 6.5 mm. The maximum intensity occurred at two spatial locations, *z* = 3.5 and 5.5 mm. The second maximum intensity observed at *z* = 5.5 mm was, however, weaker than that at *z* = 3.5 mm.

(ii) **Cu I (515.3 nm)**: The intensity of this transition increased almost linearly with *z* up to 3.5 mm and then decreased gradually up to *z* = 5.5 mm. At *z* = 6.5 mm the intensity was slightly increased.

(iii) **Cu I (521.8 nm)**: The intensity of this transition increased with *z* up to 2.5 mm and then gradually decreased up to *z* = 6.5 mm.

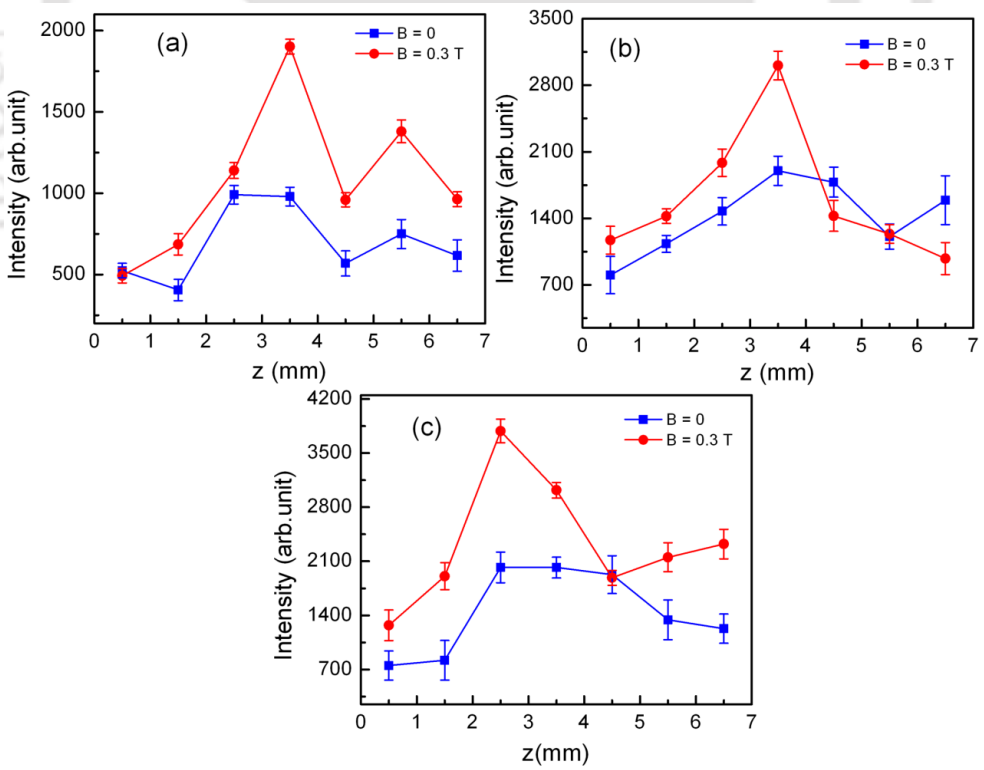


**Fig. 4.15.** Cu I Intensity variation as a function of *z* at *B* = 0 and *B* = 0.3 T: (a) Cu I (510.5 nm), (b) Cu I (515.3 nm), and (c) Cu I (521.8 nm).

**B. In the presence of magnetic field**

From Fig. 4.15, it is seen that the response of each Cu I transition in LPP to magnetic field is different with *z*. In the presence of magnetic field, the intensity was enhanced for each Cu I transition up to *z* = 3.5 mm and it showed different behavior at *z* beyond 3.5 mm. (i) Cu I (510.5 nm): The intensity variation showed similar trend as without magnetic field, however, the intensity was enhanced in the presence of magnetic field. (ii) Cu I (515.3 nm): The intensity enhanced up to *z* = 3.5 mm. The enhancement was not observed beyond *z* = 3.5 mm i.e. at larger distances. (iii) Cu I (521.8 nm): The intensity initially increased up to *z* = 2.5 mm and then decreased when *z* was increased from 3.5 to 4.5 mm. However, it increased from *z* = 4.5 to 6.5 mm. The overall enhancement was observed throughout at *z* = 0.5 to 6.5 mm.

The intensity of a transition line in LPP depends on electron density, neutral and ion density, and electron temperature which in turn affects the electron impact excitation and recombination rate.[68] Thus, the transition line intensity is contributed by the electron impact excitation and recombination processes. The spatial behavior observed in atomic and ionic transitions in the presence of magnetic field in air ambient can be looked at as follows. The main processes[68] occurring in plasma in the presence of magnetic field and ambient air are (i) increase in electron temperature due to the Joule's heating in the presence of magnetic field, (ii) increase in electron density due to combined effect of ambient air and magnetic field (iii), enhance in electron confinement by magnetic field, and (iii) increase in collision due to gyrated motion of electron about magnetic field. In the presence of magnetic field, the electron density and temperature increased which enhanced electron impact excitation rate. As *z* was increased, the electron temperature and density decreased. However,

the electron density remained higher than the minimum limit for occurrence of the recombination process.

**(a)** ***B* = 0**: At shorter distances from target the temperature of plasma was very high and this region (core of plasma) is highly ionized. Therefore, the neutral atom density is low and hence the intensity of atomic transition. As *z* was increased the electron temperature decreased and the electrons recombined with ions resulting in the generation of excited atoms. As a result of this, the intensity of atomic transition was found to be pronounced at farther distances. However, at relatively larger distances the intensity of neutral lines decreased considerably due to the significant decrease in electron density and temperature which in turn reduced the electron impact excitation and three-body recombination process.

**(b)** ***B* = 0.3 T**: The electron temperature and density was very high near the target i.e. (at shorter distances). The plasma pressure was very high which expelled out the external magnetic field. Therefore, the enhancement is small at shorter distances (*z*) due to the insignificant effect of magnetic field on plasma. However, as *z* was increased the electron temperature and density lowered which resulted in low plasma pressure. At a distance *z* equal to stopping radius where the plasma pressure is balanced by magnetic pressure, the plasma is decelerated considerably and confined. As a result, the electron density and temperature becomes larger resulting in an increase in electron impact excitation and recombination processes.

Interestingly, the behavior of each Cu I transition with *z* was found to be different in the presence of magnetic field which is discussed follows:

(I) **Cu I (510.5 nm)**: The intensity of an atomic transition depends on the number of atoms in the excited state of the transition which in turn depends on the populating

processes of the excited state. The populating processes of upper energy state (4p $^2P_{3/2}$) of the Cu I (510.5 nm) are (i) electron impact excitation from ground state (4s $^2S_{1/2}$) with relative contribution of 92 % (ii) radiative decay from 4d $^2D_{5/2}$ with relative contribution of 7.3 % (iii) electron impact excitation from $3d^9$ $^2D_{5/2}$ with relative contribution of only 0.1 %. The main populating process of this upper energy state is attributed to the electron impact excitation from the ground state and the radiative decay of Cu I (521.8 nm) from 4d $^2D_{5/2}$.[169] At *z* =3.5 mm, the intensity is quite improved in the presence of magnetic field. It is because of increase in collisional excitation of atoms as a result of increase in electron temperature and density. At farther distances, say beyond *z* = 4.5 mm, the electron impact excitation is decreased for all three transitions. However, the enhancement of this line was observed at *z* = 5.5 mm. The appearance of this may be due to the fact that the populating process for this transition at farther distances is more likely to be the radiative decay which is not involved in other transitions. It is seen that at larger *z* the electron temperature is reduced. The atom gains energy from electron through collisions. These low temperature electrons may excite the atom to the upper energy state of Cu I (510.5 nm) i.e. 4p $^2P_{3/2}$ but not to other higher excited states of Cu I (515.3 nm) i.e. 4d $^2D_{3/2}$ and Cu I (521.8 nm) i.e. 4d $^2D_{5/2}$ because of the depopulating process of the ground state is mainly by electron impact excitation to the higher levels 4p $^2P_{1/2}$ and 4p $^2P_{3/2}$.[169] Therefore, the other possibility of the enhancement in intensity at *z* beyond 4.5 mm may be due to the increase in electron impact excitation in the presence of magnetic field.

(II) **Cu I (515.3 nm)**: The populating processes of upper energy state (4d $^2D_{3/2}$) are[169] (i) electron impact excitation from ground state (4s $^2S_{1/2}$) with relative

contribution of 98.1 % (ii) electron impact excitation from 4p $^2P_{1/2}$ with relative contribution of 0.1 %. The electron impact excitation from the ground state is the main contribution to populate the upper energy state of Cu I (515.3 nm). The intensity was larger at $z$ = 3.5 mm in the presence of magnetic field. However, the effect of magnetic field was insignificant from $z$ = 4.5 to 6.5 mm. It is reported that the electron density is considerably lowered beyond stopping radius.[45] The electron temperature is also reduced at farther distances. The adiabatic expansion of plasma and collision with atoms of ambient air caused rapid reduction in electron temperature. The reduction in electron temperature and density at larger $z$ resulted in decrease in the electron impact excitation and hence the intensity.

(III) **Cu I (521.8 nm)**: The populating processes of upper energy state (4d $^2D_{5/2}$) of this transitions are [169] (i) electron impact excitation from ground state (4s $^2S_{1/2}$) with relative contribution of 98.1 % (ii) electron impact excitation from 4p $^2P_{3/2}$ with relative contribution of 0.2 % (iii) electron-ion three body recombination with relative contribution of 1.1 %. Therefore, the populating process for this transition is mainly due to the electron impact excitation and small contribution from the electron-ion three bodies recombination. The intensity of this transition was pronounced at distances between $z$ = 2.5 to 3.5 mm in the presence of magnetic field. It is more likely due to an increase in the electron temperature and density which favours the electron impact excitation from ground state. Beyond $z$ = 4.5 mm the intensity again increased slightly. It is attributed to the increase in three-body recombination process which populated the highest excited state (4d $^2D_{5/2}$). Owing to decrease in the electron temperature and density at these farther distances from the target the electron impact

excitation decreased while the recombination processes are enhanced. Therefore, the increase in intensity at farther distances is probably due to recombination process.

From above discussions, around $z$ = 2.5 to 3.5 mm the intensity enhancement of Cu I (510.5 nm) was maximum. It is attributed to an increase in the electron impact excitation of Cu I (510.5 nm) in the presence of magnetic field. The total relative contribution in populating the atoms to excited state of this transition was 99.5 % and that of Cu I (515.3 nm) and Cu I (521.8 nm) were, respectively, 98.2 and 98.3 %. The highest contribution in populating atoms to the excited state leads to maximum enhancement in intensity (Cu I (510.5 nm)) compared to Cu I (515.3 nm) and Cu I (521.8 nm). The small difference in enhancement between Cu I (515.3 nm) and Cu I (521.8 nm) is due to the small difference in populating contributions. The excitation rate coefficient between upper and lower energy state of Cu I (510.5 nm) is the smallest among three atomic transitions. The calculation of excitation rate coefficient is discussed in section 4.2.3. However, from the experimental observation it was found to be more pronounced in the presence of magnetic field which signifies the involvement of excitation process from other higher and lower states, and also recombination process.

In the presence of magnetic field, due to confinement of the plasma, the mean free path of electron and atom decreases. Since, the collision cross-section is inversely proportional to the mean free path the electron-atom collision increases which results in increase in electron-impact excitation rate and hence the intensity of the transition lines. It has been seen that the increase in intensity is mainly due to electron impact excitation rather than the radiative recombination.[45,126] However, three-body recombination occurs at farther $z$ where the electron temperature becomes lower. Fig.

4.16 shows the variation of Cu II (508.8 nm) as a function of plasma expansion direction distance (*z*). The intensity of Cu II near the target (at *z* = 0.5 mm) was high in the absence of magnetic field and it was almost constant up to 2.5 mm and decreased relatively fast when *z* increased to 3.5 mm. In the presence of magnetic field, the intensity is higher than that without magnetic field which is attributed to increase in absorption of laser photon near the target through inverse bremsstrahlung process due to increase in electron density in the presence of magnetic field which makes further heating of plasma and hence ionization.

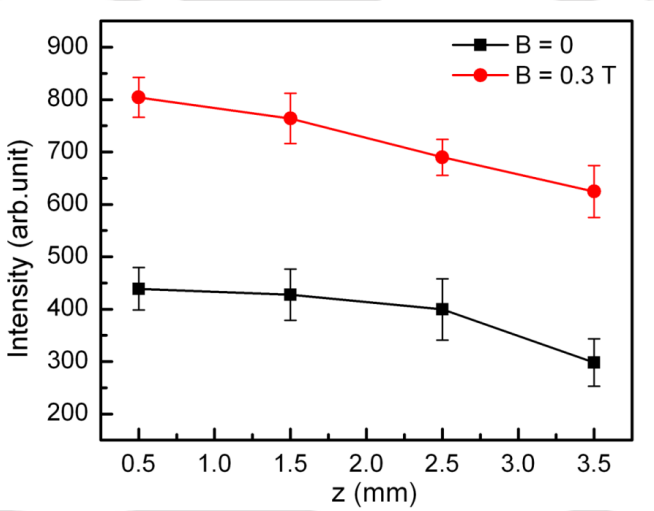


**Fig. 4.16.** Intensity variation of Cu II (508.8 nm) with *z* at *B* = 0 and *B* = 0.3 T.

The intensity of Cu II decreased gradually as *z* was increased from 0.5 to 3.5 mm. The other possibility is the higher in plasma temperature in the presence of the magnetic field which may increase further ionization. Beyond 3.5 mm, the Cu II line appeared in the absence and the presence of magnetic field but the intensity was quite small and negligible. It indicates the ionic emission is mostly from the small central core hot region of the plasma. The increase in core dimension in the presence of

magnetic field caused the reduction in intensity of ionic line up to 3.5 mm relatively slowly while it decreased rapidly beyond $z$ = 2.5 mm in the absence of magnetic field. For axial distance at $z$ = 3.5 mm and at $B$ = 0.3 T, the calculated excitation rate coefficient of Cu I (510.5 nm), Cu I (515.3 nm), and Cu I (521.8 nm) between upper and lower states of the transitions are, respectively, $2.1 \times 10^{-9}$, $231.0 \times 10^{-9}$, and $199.1 \times 10^{-9}$ $cm^3s^{-1}$. However, the intensity enhancement of Cu I (510.5 nm) in the presence of magnetic field was higher at $z$ = 3.5 mm than other two atomic lines. It is attributed to involvement of other populating process from the energy states other than the upper and lower states of the transitions. Further, in order to justify the energy loss due to reflection of laser from plasma in the presence of magnetic field, the plasma frequency ($\nu_p$) was calculated at $z$ = 0.5 mm from the target where the density is maximum using the relation $\nu_p = 8.9 \times 10^3 n_e^{1/2}$ Hz, where, $n_e$ is the electron density in $cm^{-3}$. At $B$ = 0.3 T, the electron density at $z$ = 0.5 mm is $10.90 \times 10^{16}$ $cm^{-3}$, therefore plasma frequency is $2.9 \times 10^{12}$ Hz which is less than the incident laser frequency ($5.6 \times 10^{14}$ Hz). This indicates the laser energy loss arises due to reflection form the plasma even in the presence of the magnetic field is not significant. The variation of intensity of Cu I (521.8 nm) and Cu II (508.8 nm) with electron temperature is shown in Fig. 4.17. As the electron temperature of plasma increased, the intensity of atomic line Cu I (521.8 nm) decreased while the intensity of ionic line Cu II (508.8 nm) was found to increase. It is attributed to increase in ionization of copper atom. In the presence of magnetic field, the temperature and density increased which favors ionization.

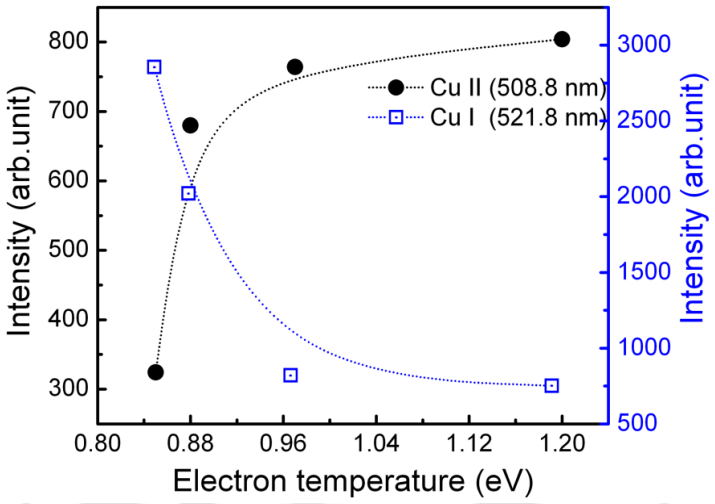


**Fig. 4.17.** Variation of Cu I (521.8 nm) and Cu II (508.8 nm) with electron temperature.

## 4.4. Effect of lens focusing distance on Cu plasma with magnetic field

### 4.4.1. *Time integrated optical emission spectroscopy*

Fig. 4.18(a) and (b) shows the Cu spectra in the absence and presence of 0.3 T magnetic field recorded in the wavelength range of 509 to 523 nm at different values of *d*. From the studies on the spatial behaviour of LPP along plasma expansion direction, the intensity of Cu I transition was observed to be pronounced at a distance of around 2.5 mm from the target surface.[132] Therefore, each spectrum in the absence and presence of magnetic field of 0.3 T was recorded at a distance of 2.5 mm from target. In order to study the variation of intensity of spectral lines, each spectrum was fitted with Voigt function as shown in Fig. 4.19. From the fitted profile (deconvoluted profile) the integrated intensity of Cu I and Cu II transitions is determined. Fig. 4.20 (a) and (b) shows the variation of Cu I transition intensity with *d* in the absence and presence of magnetic field, respectively. As *d* was increased from -10 to 0 mm via -5 mm, the intensity of Cu I line was quite weak and remained almost constant. On

further increase in *d* from 0 to 5 mm, the intensity of Cu I line increased and then decreased slightly at *d* = 10 mm. It was observed that the effect of magnetic field on Cu I transitions at the focusing condition *d* = -10 to 0 mm was not significant. However, the magnetic field effect on intensity enhancement was observed when the *d* increased from 0 to 10 mm.

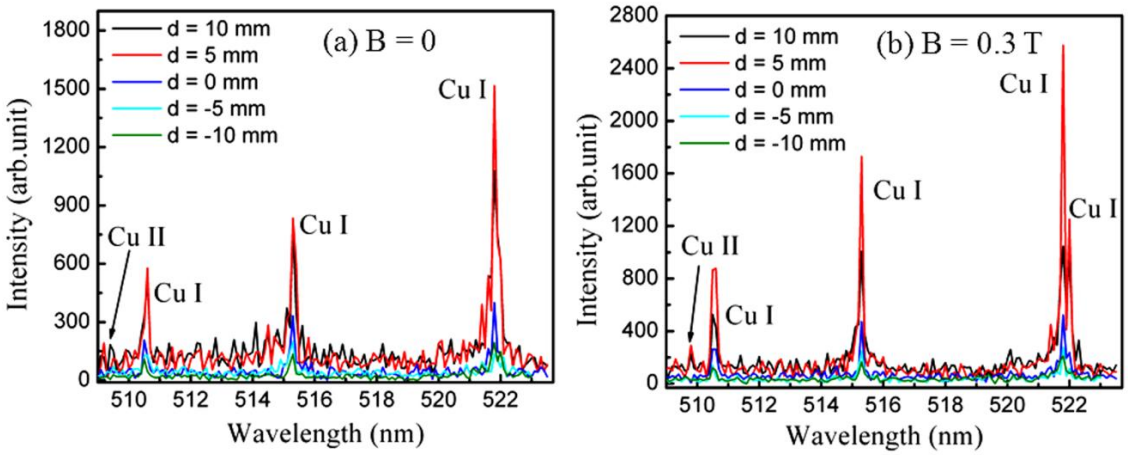


**Fig. 4.18.** Spectra of Cu plasma at different *d* = -10, -5, 0, 5, and 10 mm at (a) *B* = 0 and (b) *B* = 0.3 T.

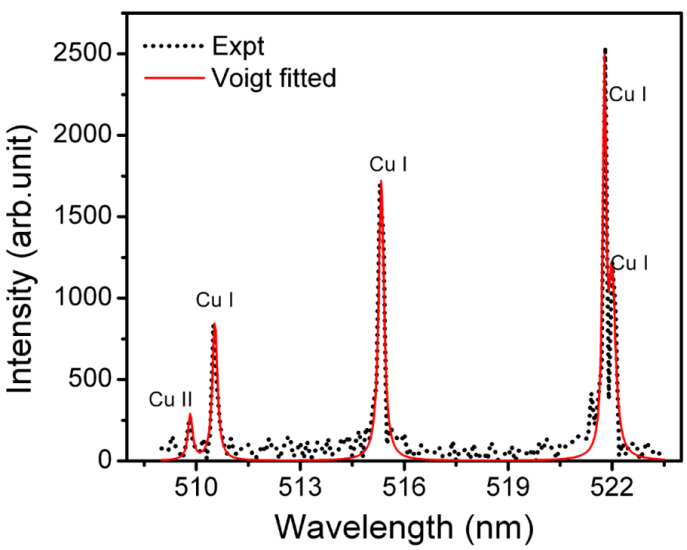


**Fig. 4.19.** Voigt fitted spectrum at *B* = 0.3 T and *d* = 5 mm.

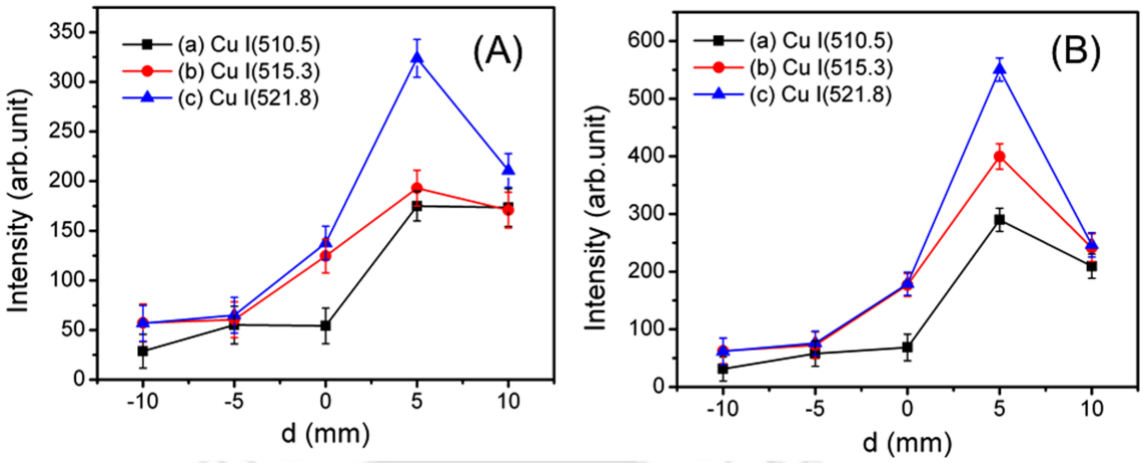


**Fig. 4.20.** Intensity variation of (a) Cu I (510.5 nm), (b) Cu I (515.3 nm), and (c) Cu I (521.8 nm) with focusing distance *d* at (A) *B* = 0 and (B) *B* = 0.3 T.

The intensity of Cu I line was more enhanced at *d* = 5 mm and found to decrease at *d* = 10 mm. More interestingly, another transition Cu I (522.0 nm) was observed separately in the presence of the magnetic field. This transition appeared as a hump in Cu I (521.8 nm) at $S_1$ in the absence of magnetic field. In the presence of magnetic field, this transition was observed at $S_1$ (*d* = 5 mm) and $S_2$ (*d* = 10 mm). The intensity of Cu I (522.0 nm) is more pronounced at $S_1$ than $S_2$. The upper energy states of the transitions at Cu I (521.8 nm) and Cu I (522.0 nm) are very close to each other. The oscillator strength of Cu I (521.8 nm) is almost ten times higher than that Cu I (522.0 nm). Therefore, the Cu I (521.8 nm) transition dominated over Cu I (522.0 nm). However, in the presence of magnetic field, the magnetic confinement resulted in more excitation of atom which led to the appearance of Cu I (522.0 nm) transition. At focusing location ($S_0$), the laser intensity was nearly 3 and 4 times higher than at $S_1$ and $S_2$, respectively. At $S_0$ with smaller spot size and higher intensity, the plasma expanded with higher axial velocity as observed in the

simulation results discussed in chapter 6. Li et al. studied the influence of spot size on the laser-produced Cu plasma dynamics at atmospheric pressure without magnetic field and showed that the dynamics of the plasma is independent of the position of the target if the spot size is the same.[32] They also observed that the high intensity region of the plasma lies near the plume front rather than near the target surface. It is attributed to the generation of more energetic plasma species which absorbs more laser energy. As a result of this, more energetic species with faster longitudinal velocity are produced. Bulatov et al. investigated the effect of focusing distance on laser plume dynamics using fast imaging photography and reported that the signal-to-noise ratio in LIBS is low when the sample is kept at focus. It is attributed to the formation of hot ring around the main plasma. The hot ring originated as a result of scattering of particles.[170] In this study, it was also observed that the intensity of Cu I transitions was low at $S_0$. The intensity of Cu I transitions in the presence of magnetic field of 0.3 T was higher than that in the absence of magnetic field, however, the enhancement was small at $S_0$. At $S_{-1}$, the laser intensity on the target was reduced to approximately one third than that at $S_0$. Above all, the air-breakdown occurred at the focal point of the focusing lens which further reduced the laser intensity reaching the target and hence the intensity of the spectral line. The air breakdown occurs when the laser beam focused is beyond the breakdown threshold of air. The air breakdown threshold intensity ($I_{th}$) of a radiation of wavelength $\lambda$ is related to air pressure ($P_{air}$) via the relation[171] $I_{th} \propto P_{air}^{-n} \lambda^{-2}$, where $n$ is a constant. For $\lambda$ = 532 nm, the pressure varies as $P_{air}^{0.2}$ with $n$ = - 0.2. In this present study, $P_{air} = 1.013 \times 10^5$ Nm$^{-2}$ and $\lambda$ = 532 nm, therefore, the breakdown threshold is of the order of $3.5 \times 10^9$ Wcm$^{-2}$. The

intensity of laser radiation at focal point is $7.2 \times 10^9$ $Wcm^{-2}$ which is greater than the breakdown threshold. This indicates that the air breakdown indeed occurred at focal point without target. At $S_{-2}$, the laser intensity on the target was considerably reduced. Therefore, the laser ablation produced low intensity plasma. At $S_1$, the laser intensity on the target was equal to that at $S_{-1}$. However, the occurrence of the air-break down was not observed at $S_1$. Therefore, there was no attenuation of laser energy due to air-breakdown.

At $S_{-1}$ and $S_{-2}$, the plasma density (charge species density) was low which led to insignificant plasma-magnetic field interaction in the presence of magnetic field. Since the magnetic field interacts with charged particles, the increase in electron density caused plasma to interact more with the magnetic field. At focusing condition, $S_1$ and $S_2$, there was no air breakdown which resulted in strong laser-target interaction and formed high density plasma. Eventually, the strong plasma-magnetic field interaction took place. Therefore, the confinement of plasma at this focusing geometry ($S_1$ and $S_2$) was more pronounced leading to an increase in the electron density and temperature which favoured electron impact excitation.[66] The increase in electron impact excitation resulted in the enhancement of Cu I line intensity. At higher value of *d* i.e. at 10 mm, the intensity of Cu I transition decreased slightly as the laser intensity was decreased due to defocussing of laser beam on Cu target. Fig. 4.21 shows the variation of enhancement factor of Cu I (510.5 nm), Cu I (515.3 nm), and Cu I (521.8 nm) with focusing distance.

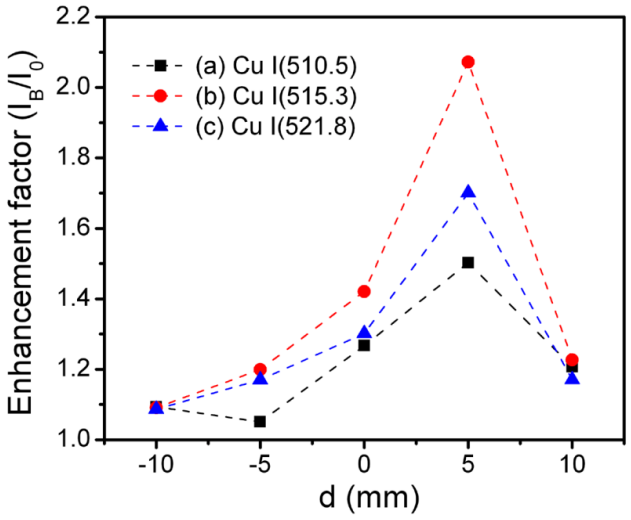


**Fig. 4.21.** Intensity enhancement factor as a function of *d*: (a) Cu I (510.5 nm), (b) Cu I (515.3 nm), and (c) Cu I (521.8 nm).

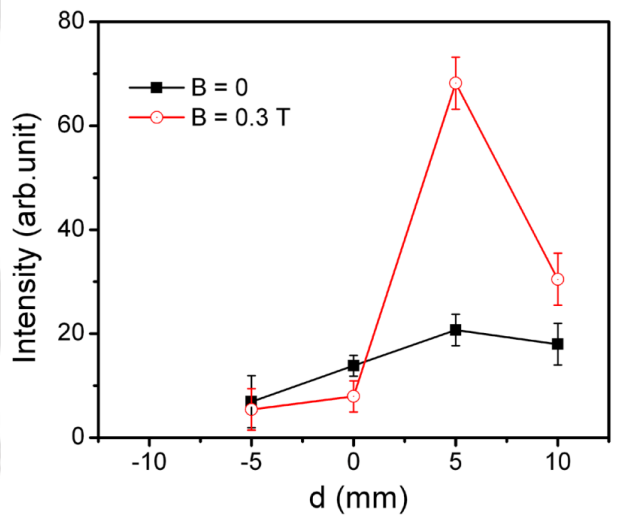


**Fig. 4.22.** Intensity variation of Cu II (509.4 nm) as a function of *d* at *B* = 0 and *B* = 0.3 T.

It is observed that the enhancement factor of all three Cu I transitions are different. The enhancement factor of Cu I (510.5 nm), Cu I (515.3 nm), and Cu I (521.8 nm) at *d* = 5 mm are, respectively 1.5, 2.1, and 1.7. The difference in enhancement factor is attributed to different electron impact excitation rate. The excitation rate coefficients of Cu I (510.5 nm), Cu I (515.3 nm), and Cu I (521.8 nm)

at $d$ = 5 mm in the absence of magnetic field are, respectively, $1.8 \times 10^{-9}$, $171.1 \times 10^{-9}$, and $165.4 \times 10^{-9}$ $cm^3$ $s^{-1}$. In the presence of magnetic field of 0.3 T, the corresponding excitation rate coefficients are $2.1 \times 10^{-9}$, $198.9 \times 10^{-9}$, and $192.2 \times 10^{-9}$ $cm^3$ $s^{-1}$. The excitation rate coefficient of Cu I (515.3 nm) transition is comparatively higher which resulted in highest enhancement factor among the three Cu I transitions. The variation of Cu II (509.4 nm) with $d$ was also analysed. Fig. 4.22 shows the intensity variation of Cu II as a function of $d$. The intensity of Cu II (509.4 nm) in the presence and absence of magnetic field was found to be highest at $S_1$. However, the intensity in the presence of the magnetic field was more pronounced (i.e. EF is highest at $S_1$). The EF of Cu II at $S_1$ is around 3.3. At $S_{-2}$ the intensity of Cu II is very weak and it cannot be fitted properly.

### 4.4.2. *Temporal evolution of Cu I and Cu II at different lens-to-target positions.*

Since the plasma is highly transient, the temporal evolution of spectral line transitions was also studied. Fig. 4.23(a) and (b) shows the temporal profile of Cu I (515.3 nm) in the absence and presence of magnetic field at different focusing distances, namely, at $S_{-2}$, $S_{-1}$, $S_0$, $S_1$, and $S_2$. The integrated intensity of each transition was determined by multiple-fitting of the temporal profile at each experimental condition as discussed in section 4.2.2. In the absence of magnetic field, the temporal profile width of the slower component at $S_1$ (47 ns) was larger than that at $S_0$ (44 ns). Grun et al.[172] showed that the distribution width is governed by a scaling factor, $R_S/c\tau$, where $R_S$ is the spot radius on the target surface, $c$ is the sound speed, and $\tau$ is the pulse duration. It was also observed in the simulation (discussed in chapter 6) that plasma species at $S_0$ moved faster than that at $S_1$ which was also confirmed from temporal profile.

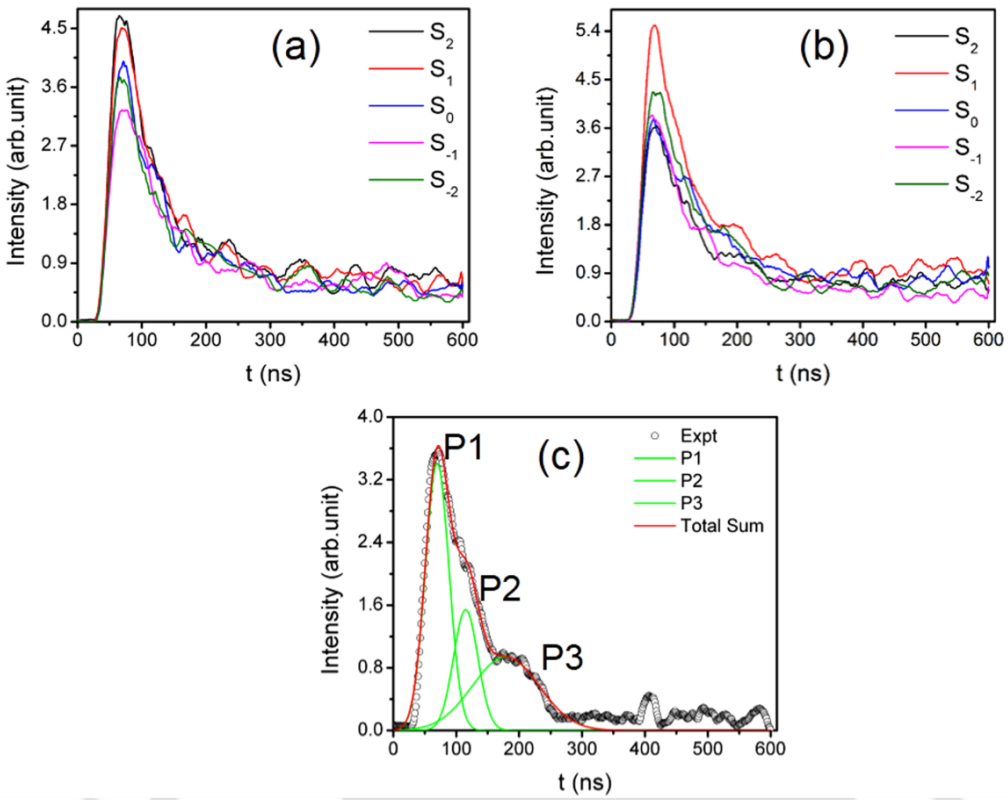


**Fig. 4.23.** Temporal behavior of Cu I (515.3 nm) at (a) $B$ = 0 and (b) $B$ = 0.3 T. (c) Multiple peaks fitted Cu I (515.3 nm) profile at $S_2$ and $B$ = 0.3 T.

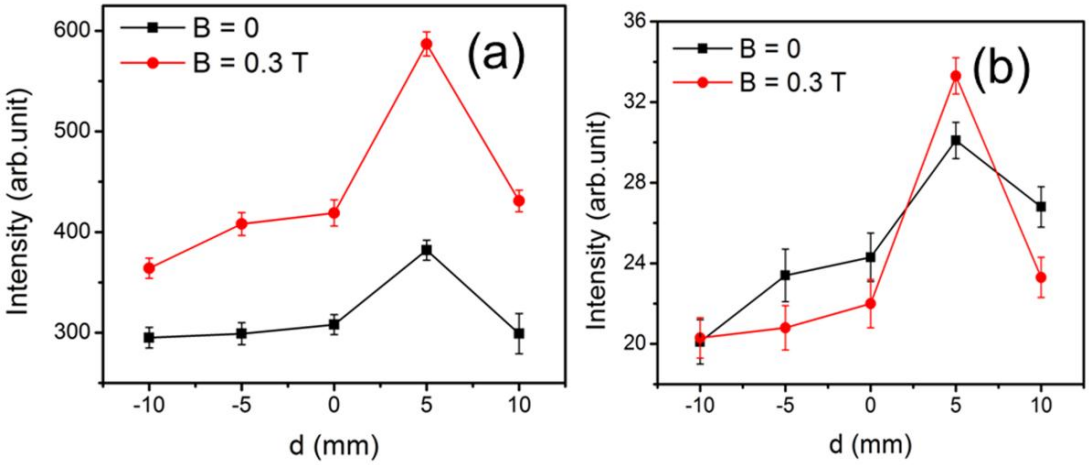


**Fig. 4.24.** Variation of intensity with focusing distance (a) Cu I (515.3 nm) and (b) Cu II (509.8 nm).

The slower component (P2) of Cu I (515.3 nm) at $S_0$ appeared at around 119 ns while the P2 at $S_1$ appeared at 128 ns after the laser pulse. The broadening was mainly caused by an increase in number density of slower components in the tailing region of the profile.[31,36] Therefore, the scaling factor is justified with the experimental results. In the presence of 0.3 T magnetic field, the appearance of a third component was observed. The variation of integrated intensity of atomic and ionic transitions with the focusing distances is shown in Fig. 4.24 (a) and (b). The intensity is found to be maximum at $S_1$. The ionic line also showed maximum intensity at $S_1$. In the presence of magnetic field, the intensity of both neutral atomic and ionic transitions is more pronounced. Increase in broadening at $S_1$ indicates an increase in number density of slower component which was due to deceleration of plasma around the distance from the target at which optical emission was recorded. Similarly, other atomic transitions studied at different sample locations in the absence and presence of magnetic field showed maximum intensity enhancement at $S_1$. Irrespective of transitions, the maximum intensity enhancement occurred at $S_1$.

### 4.4.3. *Determination of electron density and temperature*

The profile width was obtained from the Fourier transformed of the temporal profile. Fig. 4.25 shows the variation of the electron density as a function of *d*. As *d* increased from -10 to 0 mm, the electron density increased gradually from $(2.8 \pm 0.5) \times 10^{16}$ to $(4.8 \pm 0.2) \times 10^{16}$ $cm^{-3}$ in the absence of magnetic field. In the presence of magnetic field also, it varied from $(3.9 \pm 0.3) \times 10^{16}$ to $(5.5 \pm 0.2) \times 10^{16}$ $cm^{-3}$. The electron density of the plasma in this region has no significant difference in the absence and presence of magnetic field.

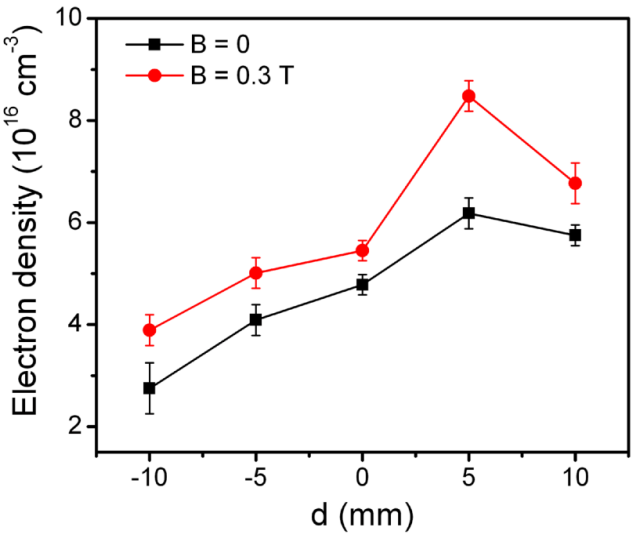


**Fig. 4.25.** Variation of electron density as a function of *d* at *B* = 0 and 0.3 T.

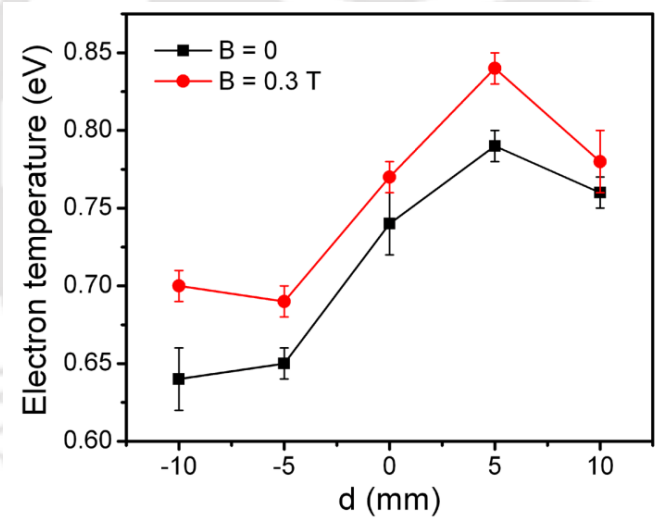


**Fig. 4.26.** Variation of electron temperature with *d* at *B* = 0 and 0.3 T.

It is attributed to the loss of laser energy due to air breakdown which resulted in small ablation rate. When *d* increased from 0 to 5 mm, the electron density increased from $(4.8 \pm 0.2) \times 10^{16}$ to $(6.2 \pm 0.1) \times 10^{16}$ $cm^{-3}$ and then decreased slightly to $(5.8 \pm 0.2) \times 10^{16}$ $cm^{-3}$ at $d$ = 10 mm. In the presence of magnetic field, it followed

the same trend but it increased drastically from $(5.5 \pm 0.2) \times 10^{16}$ to $(8.5 \pm 0.1) \times 10^{16}$ $cm^{-3}$ when $d$ increased from 0 to 5 mm in the presence of magnetic field. At $d = 0$, the spot size was small and laser fluence was highest. It may have created a deep and narrow crater which induced the confinement of plasma within the crater walls and re-deposition of melted material in the crater itself. As a result, less amount of mass was ablated from Cu.[173] The higher electron density was due to the magnetic confinement of plasma as discussed earlier.

Fig. 4.26 shows the variation of $T_e$ as a function of $d$ in the absence and presence of magnetic field. As $d$ increased from -10 to 5 mm, $T_e$ increased from (0.64 ± 0.02) to (0.79 ± 0.01) eV and then decreased slightly to (0.76 ± 0.01) eV when $d$ increased to 10 mm. In the presence of magnetic field, the $T_e$ was higher than that without magnetic field. At $d$ = 5 mm, the electron temperature was 0.84 eV and electron density was $8.73 \times 10^{16}$ $cm^{-3}$, the plasma thermal pressure was $8.2 \times 10^{3}$ $Nm^{-2}$ and the magnetic pressure exerted by 0.3 T magnetic field was $3.6 \times 10^{4}$ $Nm^{-2}$. By considering the effect of air ambient pressure, the value of $\beta$ was found to be nearly 0.1. $T_e$ was calculated by assuming the plasma is in local thermodynamic equilibrium (LTE). As mentioned in chapter 2, when LPP expands in the presence of magnetic field in the air ambient at atmospheric pressure, the plasma is decelerated by both air and magnetic pressure. The expansion continues until the total sum of work done by plasma to push out the magnetic field and work done against air pressure is equal to the total plasma energy. Further, the gyrated motion of electrons about the field causes more collisions with atoms and hence electron impact excitation rate. When the plasma is confined, the electron-ion interaction (electron-ion recombination) is also increased resulting in generation of atoms in excited state. Since, the radius of

gyration is proportional to mass, the electron gyro-radius is much smaller than that of ion. Therefore, the electron-atom collision rate is higher than that of ion-atom collision rate in the plasma plume in the presence of magnetic field.

Using fast imaging technique Li et al.[32] showed that the smaller the laser spot size the expansion of Cu plasma in air in the absence of magnetic field is more cylindrical at delayed time like 20 ns. When the spot size is increased, the plasma expansion is more spherical in ambient air. When the ns laser pulse interacts with the target, the leading part of the laser pulse creates plasma and the remaining part of the pulse interacts with the plasma. The plasma absorbs laser through IB process and heat up the plume resulting in increase in ionization. Depending on the spot size the extent of interaction is different. Therefore, at $S_0$ the plasma expansion was cylindrical and the cone of angle of laser beam was small. As a result of this, the absorption process was highly localized near the vicinity of plasma axis. In short, the plasma-laser interaction was weak that resulted in less ionization. The decrease in ionization made plasma of less charge particle number density and hence the plasma-magnetic field interaction as plasma interacts with magnetic field through the motion of charge particles. At $S_1$ the plasma expansion was spherical and due to larger cone angle of laser, the plasma interacted with remaining part of laser more efficiently resulting in more ionization and excitation. The increase in charge species density led to an increase in the plasma-magnetic field interaction. At $S_2$ though the cone of laser radiation was large, the laser intensity on copper target was decreased considerably. The plasma created by leading part of pulse consisted of lesser electron density and expanded with smaller velocity and hence less plasma-laser interaction. However, at

$S_{-1}$ and $S_{-2}$ the focal point was above the target and due to air breakdown at focal point the intensity of laser on target was decreased significantly resulting in less laser matter-interaction and hence plasma-magnetic field interaction.

### 4.5. Validity of local thermodynamic equilibrium

The electron temperature of the plasma was calculated by assuming the plasma in local thermodynamic equilibrium (LTE). In order to verify the LTE using McWhiter's criterion (eqn. (2.11)), the lower limit of the electron density ($n_e$) is calculated. To validate the LTE condition strictly, the transition with largest $\Delta E_{nm}$ must satisfy the above relation and the upper level of the transition should be close to ground state. Amongst the neutral transitions Cu I (510.5 nm) has largest $\Delta E_{nm}$ and its upper energy level is close to ground state, therefore, it is chosen to verify the LTE. The electron temperature in the presence of the magnetic field is 0.69 eV (8004 K). The $\Delta E_{nm}$ of Cu I (510.5 nm) is 2.43 eV. With these values, the lower limit of the electron density was calculated satisfying the LTE condition and found to be $2.0 \times 10^{15}$ $cm^{-3}$. The more precise condition obtained with quantum mechanical correction is given by the relation[109] $n_e > \frac{2.55\times10^{11}}{\langle g \rangle} T^{1/2} (\Delta E_{nm})^3$. In this case the lower limit is found to be $3.27 \times 10^{14}$ $cm^{-3}$. The experimentally observed values are order of $10^{16}$ $cm^{-3}$ which are higher than the lower limit of LTE conditions and hence satisfied the LTE condition. Since the plasma is transient, the electron density varies with time. If the variation of electron density is sufficiently slow, the above conditions are safely applicable to verify the LTE of plasma. However, if the evolution of plasma is too fast, the atoms and electrons would be unable to get time to attain LTE. In the presence of magnetic field and air ambient, the plasma is decelerated both by

magnetic field and air pressure. As a consequence of this, the electron density varies slowly. The plasma is strictly in LTE if the above two conditions and eqn. (2.12) are satisfied. By taking electron density and temperature at $B$ = 0.3 T, the relaxation time is calculated and it is found to be 6 ns. The electron density at delayed time $t$ = 58 ns (corresponding to P1 of Cu I (521.8 nm)) is 3.64 × $10^{16}$ $cm^{-3}$. Therefore, electron density at delayed time ($t$ + 6 ns) is given by 1.01× $10^{15}$ $cm^{-3}$ (since electron density varies as $n_e/t^2$) and hence $\frac{n_e(t+\tau_{rel})-n_e(t)}{n_e(t)}$ is 0.97 which is less than one. From overall considerations, though the plasma is transient it is in LTE. Here, only the variation of electron density of plasma was considered as the electron impact excitation rate is a weak function of temperature and mainly depends on electron collisions.[119]

## 4.6. Conclusion

Since the LPP is highly transient, the temporal evolution of Cu plasma was investigated and described in this chapter. As the magnetic field increased, the atomic Cu I temporal profiles exhibited multi-structured components. At $B$ = 0 and 0.1 T, the temporal profile consisted of two components P1 and P2. When the magnetic field was increased to 0.3 and 0.5, the appearance of third component P3 was observed. The reason is that the confinement of plasma is higher when the magnetic field is increased leading to enhancement of collision excitation. Eventually another component P3 is also generated at a later delayed time. The role of collapse of diamagnetic cavity and instability in the generation of multi-components in this study is ruled out. The integrated intensity enhancement was maximum at 0.3 T which is in good agreement with the spectral intensity discussed in chapter 3. The spatially resolved studies showed that the electron density and temperature of Cu plasma

decayed slowly with *z* in the presence of magnetic field. The dimension of core and tail of the plasma was estimated from the spatial evolution of electron density and temperature. The size of core was found to increase from 2.5 mm to 4.5 mm in the presence of magnetic field. It is ascribed to increase in ionization and thermal conductivity. The different response of spectral lines to magnetic field at different *z* is more likely due to difference in populating process (electron impact excitation and three body recombination process) of the excited energy state from which the transition occurs. Since the electron density and temperature evolve spatially, the populating process of the excited energy state also depends on *z* and hence the intensity of the spectral lines. The effect of LTSD on Cu plasma in the absence and presence of magnetic field was investigated using OES. The optical emission intensity enhancement in the presence of magnetic field is more pronounced when the target is at $S_1$ amongst the different positions of the target in this study. At $S_1$ there is no attenuation of laser energy as a result of air breakdown leading to more interaction of laser with target and hence maximum intensity enhancement at $S_1$ which is confirmed both from time integrated and temporal evolution optical emission studies. These studies discussed in this chapter may help to improve the sensitivity of LIBS in the presence of magnetic field. The present work may also be useful to study the PLD in the presence of magnetic field in air ambient by determining the target-substrate distance to reduce debris in thin film deposited on the substrate.

# Chapter 5

## *Experimental Studies on Effect of Magnetic Field on Laser Ablation of Cu and Deposited Particles*

It is reported in the literature that by application an external magnetic field, the depth of the laser ablated crater can be enhanced.[49,94,96,99] However, a very few studies on effect of magnetic field on laser ablation of Cu and Al in air are documented. The laser ablation of Cu is of particular interest to synthesise the Cu oxide nanoparticles for applications in solar cell, sensor, antifungal activity, etc.[105] Al with micro holes can be used in solar cell and it is also used as electrodes in biotechnology.[9] The application of magnetic field can alter the dynamical properties of plasma which in turn affect the plasma-target interaction. In this chapter, the magnetic field is varied to explore the effect of magnetic field on laser ablation/deposition of particles on the Cu target systematically.

### 5.1. Experimental details

The laser fluence was fixed at 14 $Jcm^{-2}$ and the magnetic field was varied from 0 to 0.5 T. The laser ablated craters were generated by impinging 50 laser shots on Cu and Al at $B$ = 0, 0.1, 0.3, and 0.5 T, respectively. The two metals (Cu and Al) of different thermo-physical properties were studied to justify the dependence of laser ablation on thermo-physical property of the metals. The surface of laser ablated Cu/Al was characterized using optical microscopy, surface profilometer, FESEM, EDX, XRD, Raman spectroscopy, and PL to investigate the effect of magnetic field on laser ablation/deposited particles. The effect of magnetic field on melt ejection was also

studied. In this study the craters were generated by impinging more laser shots (70) on Cu target as the melt ejection is dependent on the number of laser shots. It was also extended by introducing the non-uniform magnetic field during laser ablation.

## 5.2. Effect of variation of magnetic field on laser ablation of Cu and Al

It is well known that if the thermal diffusion length of the target is greater than the laser penetration depth, then the ablation mechanism is dominated by thermal process. The thermal diffusion length ($L_{th}$) of Cu and Al are calculated using the eqn. (2.1). The calculated $L_{th}$ of Cu and Al are, respectively, 2.15 and 1.97 $\mu$m. The thermal and optical properties of the Cu and Al (at $\lambda$ = 532 nm) are given in table 5.1.[165,174]

**Table 5.1.** Thermo-physical parameters of copper and aluminium.

| Property | Cu | Al |
|---|---|---|
| Density $\rho$ ($gcm^{-3}$) | 8.96 | 2.70 |
| Melting point $T_m$ (K) | 1356 | 933 |
| Boiling point $T_b$ (K) | 2840 | 2740 |
| Thermal conductivity $k$ ($Wm^{-1}K^{-1}$) | 401 | 238 |
| Thermal diffusivity $D_{th}$ ($cm^2s^{-1}$) | 1.16 | 0.97 |
| Optical penetration depth $L_{op}$ (nm) | 14 | 6.7 |
| Absorption coefficient $\alpha_{ab}$($10^5$ $cm^{-1}$) | 5.97 | 14.6 |
| Specific heat $C$ (J/kg K) | 386 | 917 |
| Reflectivity (at $\lambda$ = 532 nm) | 0.61 | 0.92 |

Since, $L_{th}$ is much larger than the optical penetration depth, therefore, the ablation process is dominated by thermal process. Fig. 5.1 shows the surface images and corresponding depth profiles of the laser ablated Al at $B$ = 0 and 0.3 T, respectively. The depth profiles were extracted along the line PQ (Fig. 5.1). The laser ablation was quantified by measuring depth, width, and ablated volume of the craters. The crater diameter (width) is defined as the distance between two diametrically opposite points in the peripheral rim formed around the crater. The diameter of all craters generated at different magnetic fields was measured from the line profile and optical microscopy image. Fig. 5.2 depicts the optical images of laser ablated Al at $B$ = 0 and 0.5 T, respectively.

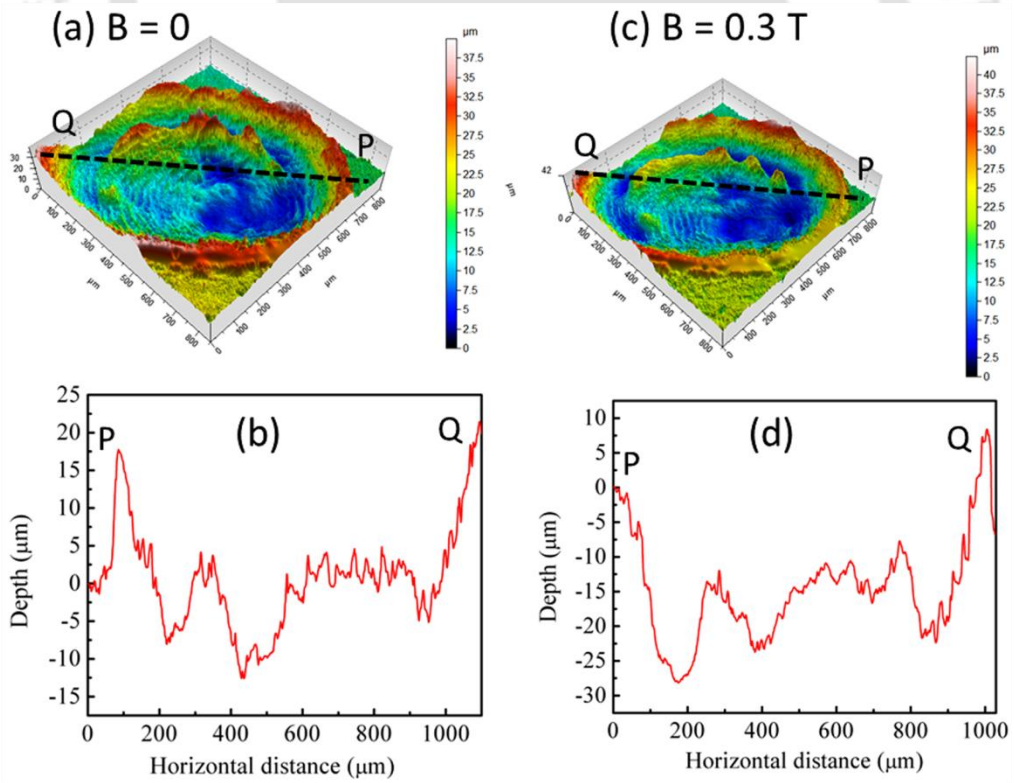


**Fig. 5.1.** Profilometer images of aluminium at (a) $B$ = 0, (b) $B$ = 0.3 T. (c) and (d) are corresponding depth profiles.

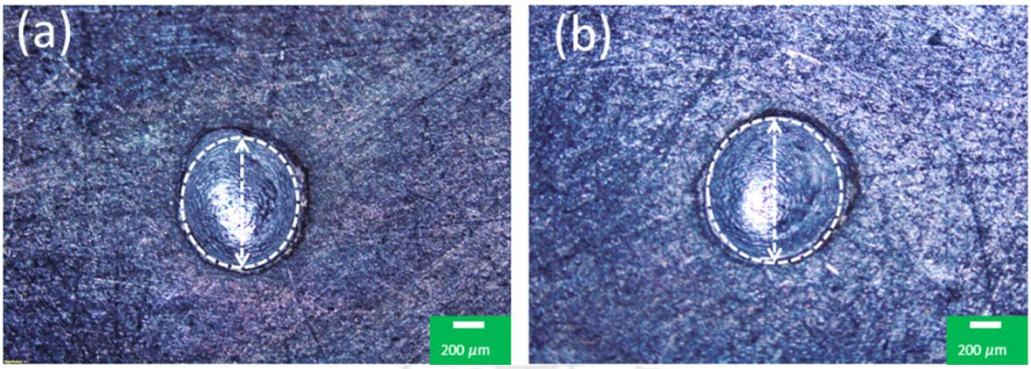


**Fig. 5.2.** Optical images of laser ablated aluminium at (a) $B = 0$ and (b) $B = 0.5$ T.

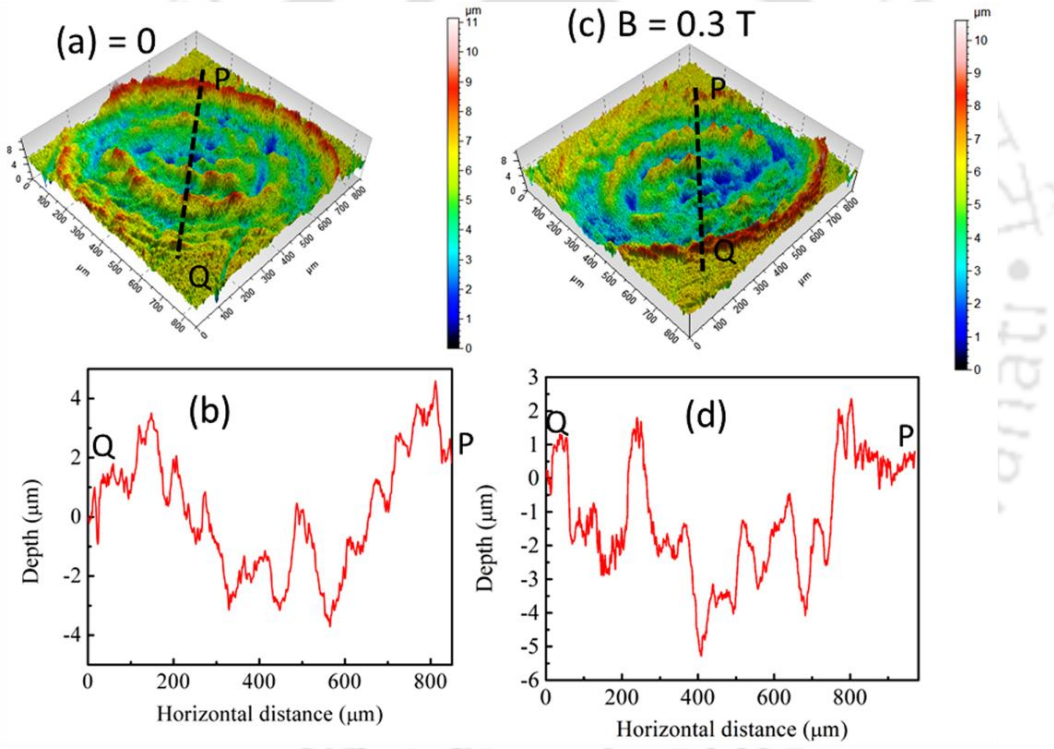


**Fig. 5.3.** Profilometer images of copper at (a) $B = 0$, (b) $B = 0.3$T. (c) and (d) are corresponding depth profiles.

The diameter obtained from the line profile at each condition is close to that obtained from the optical microscopy image. It was observed that the ablation is mainly due to melt ejection, therefore, the craters resulting from the violent expulsion

results in rough surface. It has been reported extensively in the literature that the crater surface ablated by nanosecond laser with intensity of the order of $10^9$ W/cm$^2$ in air shows rough surface due to the melt expulsion.[175–178]

Similarly, the laser ablated Cu surfaces induced at $B$ = 0 to 0.5 T were characterized from the surface profiles extracted along the line PQ. The profilometer images and their corresponding depth profiles at $B$ = 0 and 0.3 T are shown in Fig. 5.3. Fig. 5.4(a) shows the variation of crater diameter as a function of magnetic field. The crater diameter of Cu increased from (732 ± 20) to (886 ± 93) $\mu$m when the magnetic field increased from 0 to 0.1 T and then remained almost constant on further increase in the magnetic field. For Al, the crater diameter increased from (769 ± 15) to (915 ± 15) $\mu$m. The increase in crater width of Al is higher than that of Cu.

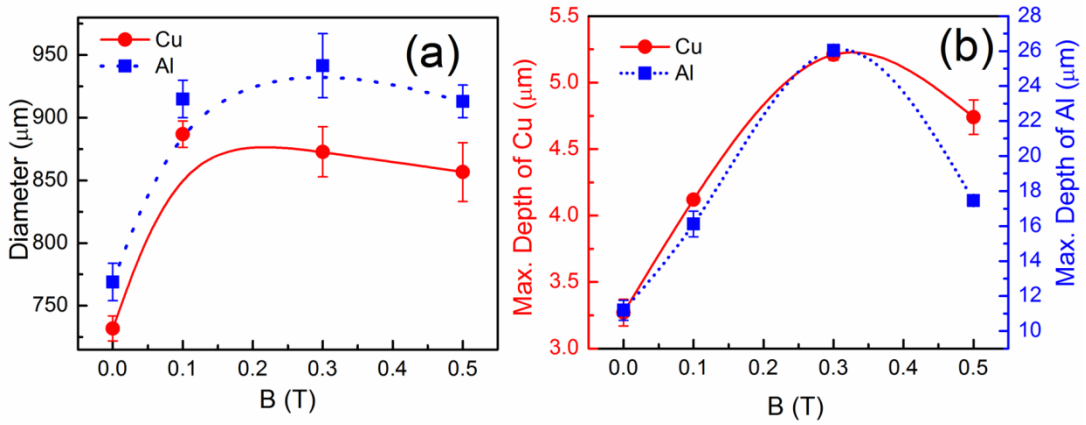


**Fig. 5.4.** Variation of (a) diameter and (b) depth of copper and aluminum as a function of magnetic field.

Using the experimental parameters $F$ = 14 Jcm$^{-2}$, $F_{th}$ = 4 Jcm$^{-2}$ and $C_f \approx 500$ $\mu$m in eqn. (2.23) the crater diameter was estimated to be $C_d$ = 791 $\mu$m in the absence of magnetic field which is close to the experimentally measured width of 732 $\mu$m. The

calculated width of the crater formed on the Al target was 950 $\mu$m whereas the experimental value was 769 $\mu$m. The difference in experimental width from the calculated value may be due to the large deposition of removed mass around the crater [Fig. 5.1 (a) and (c) at $B$ = 0 and Fig. 5.3(a) and (c) at $B$ = 0.3 T]. Fig. 5.4(b) shows the maximum depth variation as a function of magnetic field. The maximum depth is the distance of the lowest point in the crater with respect to un-ablated part of the target i.e. with respect to horizontal line PQ ( Fig. 5.5(a)). As the magnetic field increased from 0 to 0.3 T, the maximum depth of the crater increased from (3.3 ± 0.1) to (5.2 ± 0.1) $\mu$m and then slightly decreased to (4.7 ± 0.1) $\mu$m at a higher magnetic field of 0.5 T. The maximum depth of the crater with magnetic field is higher than without magnetic field. In the case of Al, the depth increased from (11.2 ± 0.6) to (26.1 ± 0.2) $\mu$m when the magnetic field increased from 0 to 0.3 T and then decreased considerably to (17.5 ± 0.1) $\mu$m at magnetic field of 0.5 T. The depth of the crater formed on the Al is found to be higher than that of Cu in the presence and absence of magnetic field.

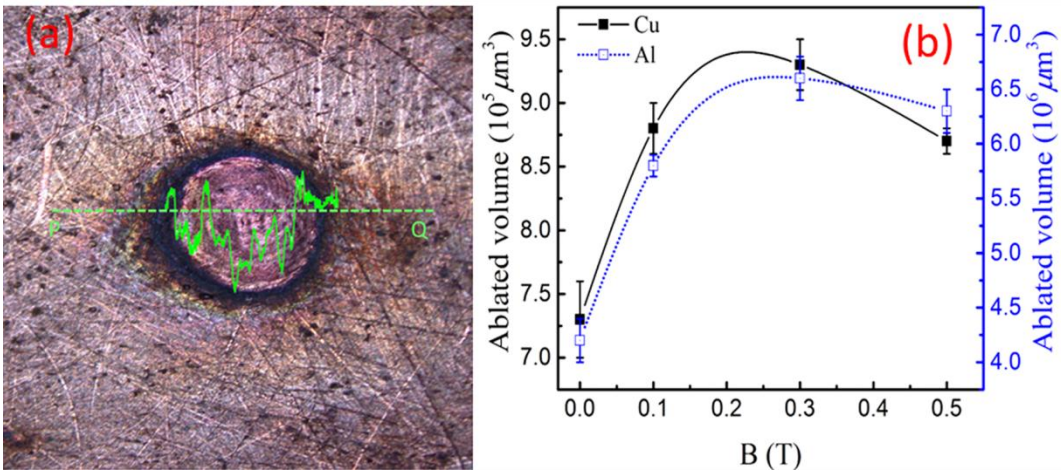


**Fig. 5.5.** (a) Optical image of laser ablated copper at $B$ = 0.3 T and surface profile. (b) Variation of laser ablated volume of aluminium and copper with magnetic field.

In order to get more insight on effect of magnetic field on laser ablation, the integrated ablated volume was measured from the profilometer analysis of the samples. The variation of the integrated volume of the ablated crater with magnetic field is shown in Fig. 5.5(b). As the magnetic field increased, the ablated volume of both Cu and Al increased and found to be maximum at $B$ = 0.3 T. The ablated volume of Al is higher than of Cu. The increase in volume is mainly due to increase in melt ejection with increase in magnetic field. Fig. 5.6(a) and (b) shows the optical images of the central portion of laser ablated crater of Cu with more resolution at $B$ = 0 and 0.3 T whereas 5.6(c) and (d) shows the corresponding images of Al, respectively. At $B$ = 0 the re-deposited mass at the centre of laser ablated Cu crater was not observed. When the magnetic field was increased to 0.1 T, the initiation of re-deposition of mass was observed. At $B$ = 0.1 T, the size of the mass deposited at the centre ranges from 30 to 88 $\mu$m. When the magnetic field was increased from $B$ = 0.1 to 0.3 T, the size of deposited mass at the crater centre decreased (8 to 12 $\mu$m) which is attributed to breaking of large droplets into smaller droplets due to increase in instability of molten layer at high recoil pressure. At the peripheral region beyond rim of crater, the size of mass was in the range of 16 to 70 $\mu$m. When the magnetic field was further increased to 0.5 T, the re-deposition of mass was not observed. The red circles in Fig. 5.6(b) encircle the ejected mass inside the centre. However, in the case of Al, the ripple structures in the absence and presence of magnetic field were observed. The ripple structure is due to the instability of molten layer. The other possibility may be due to the motion of molten aluminium as a result of radial pressure gradient between the high recoil pressure and ambient pressure. Yoo et al.[178] also observed the formation of

ripple structure in the absence of magnetic field. In the presence of 0.3 T magnetic field, more mass (in the form of ridge) is accumulated near the wall of the crater.

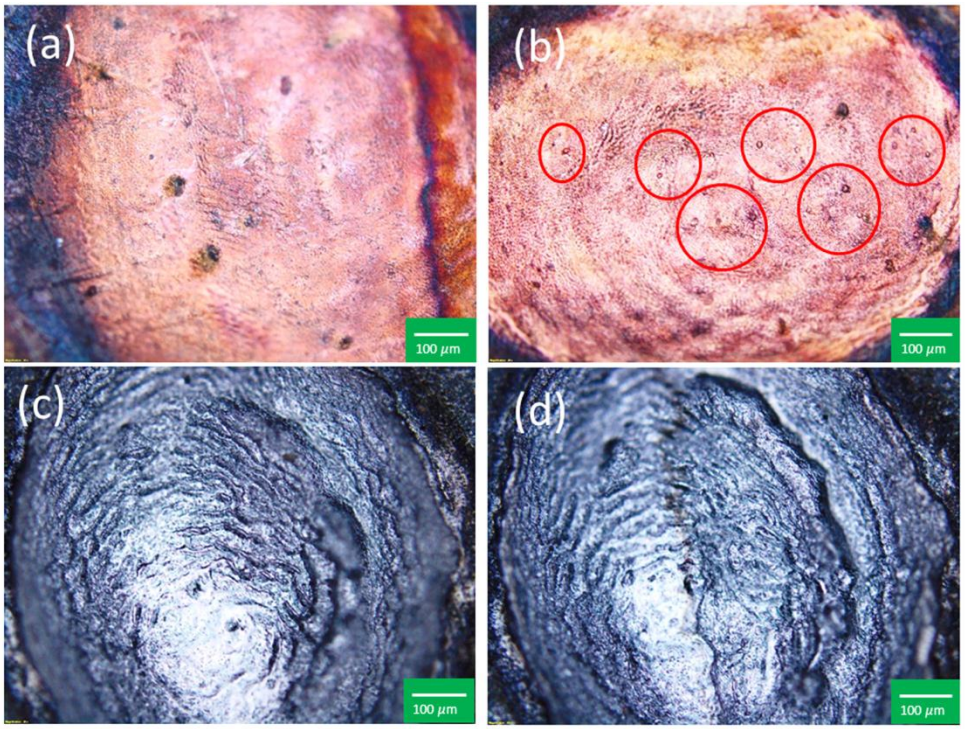


**Fig. 5.6.** Optical images of laser ablated crater centre (a) Cu with $B$ = 0 T, (b) Cu with $B$ = 0.3 T, (c) Al with $B$ = 0 T, and (d) Al with $B$ = 0.3 T.

Further, the crater structure formed is not quite smooth in both cases, with and without magnetic field. It could be due to instability formed in the molten layer during phase transformation.[176] Similar laser ablated crater structure obtained from brass in air atmosphere without magnetic field is also reported in the literature.[17] Thus, it shows that the depth profile depends on the thermo-physical properties of the material and the higher depth in Al is more likely due to low melting and boiling point of Al and high absorption coefficient (see table 5.1). The increase in depth of the profile is attributed to the following phenomena: increase in heat transfer from the magnetized

hot plasma to the target, increase in melt expulsion due to increase in vapour pressure, and increase in shock pressure which hammers the melted surface discussed as follows.

When LPP is confined by magnetic field, the average distance between the hot plasma and target surface is decreased. Ye et al.[49] reported that the average distance from laser produced plasma to target is reduced in the presence of magnetic field which enhances transfer of heat to target. The presence of magnetic field plasma size shrinks towards the target (confirmed from the snap shot of CCD images of plasma in the absence and presence of magnetic field) and hence the average distance from the plasma to target (Fig. 4.6.).[126] The thermal conductivity of the plasma in the absence and presence of magnetic field was determined using the relations discussed by Sudo et al.[168] The thermal conductivity at $B = 0$ is $k = 4.24 \times 10^{19}$ $cm^{-1}s^{-1}$ and at $B = 0.3$ T is $k_{mag} = 6.07 \times 10^{23}$ $cm^{-1}s^{-1}$. Thermal conductivity of LPP is increased in the presence of magnetic field. The increase in thermal conductivity may also result in more heat transfer to the target. Above all, more plasma species (electrons/ions) is back scattered towards target due to increase in collisions in magnetically confined plasma. In the presence of magnetic field, the plasma is compressed adiabatically at the interface between the plasma and ambient. Therefore, heating takes place at the outer surface of plasma. The electron back-scattered from the interface takes the heat and transfers to the target during collision with it. In the presence of magnetic field, due to gyration of ion about the magnetic field, collisions between ions and the target is increased resulting in more heating on the target. It was observed in previous studies that in the presence of the magnetic field, the temperature of the plasma is higher than that without magnetic field.[67] The overall consequence (i.e. increase in plasma

temperature and decrease in average distance between the plasma and the target) resulted in more heat transfer to the target from the plasma through thermal conduction[49] and some of energy is transferred from plasma to the target through other mechanisms including Nernst effect, Hall- effect and Leduc-Righi effect which in turn increased the ablation.[179] It is also reported that in addition to laser radiation, the other heating source on the target is the ion and electron bombardment.[133] Fig. 5.7(a) and (b) shows the optical images of Cu at $B$ = 0 and 0.3 T. At $B$ = 0, the ejected mass around the crater was not observed, however at $B$ = 0.3 T, more ejected mass was observed around the crater. The rim around the crater was formed due to melt displacement of melted layer formed in the crater surface due to piston effect. The thickness of the rim decreased as the magnetic field was increased. This radial material transport due to piston effect decreased when the magnetic field was increased.

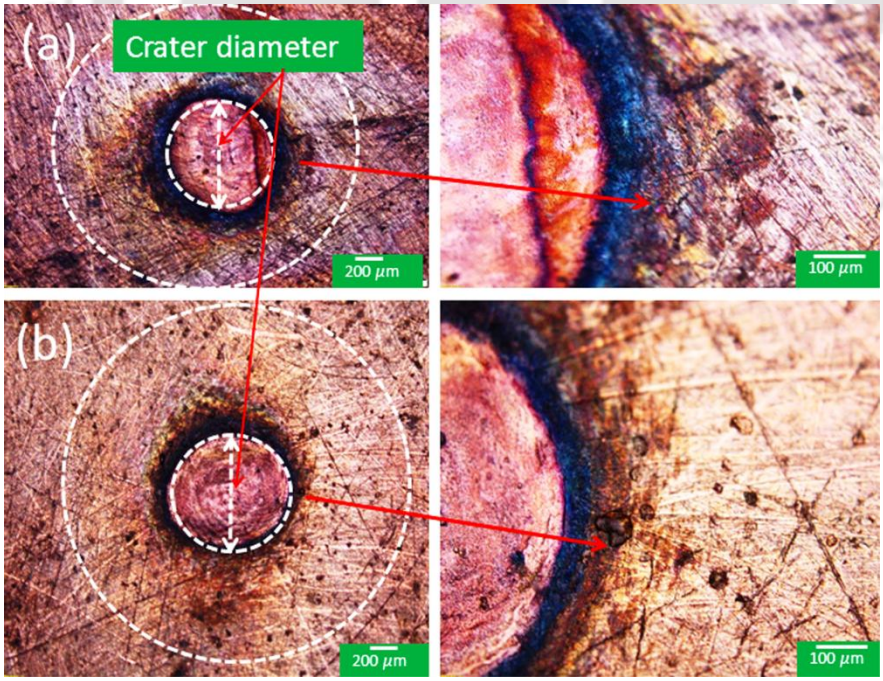


**Fig. 5.7.** Optical images of laser ablated Cu surface at (a) $B$ = 0 T and (b) $B$ = 0.3 T.

This can be seen as when the magnetic field was increased, the combined effect of magnetic pressure and air ambient was increased. It has been shown in the literature that the recoil pressure is higher in the presence of high ambient pressure.[180] When the magnetic field is introduced, the magnetic pressure comes into play in addition to air ambient pressure which leads to increase in pressure (due to recoil pressure) exerted on the irradiated surface. The increase in local recoil pressure enhances the instability in the molten layer and ejection of material in the form of droplets which leads to decrease in thickness of rim and to initiate the formation of droplets when the magnetic field is introduced during ablation. The decrease in rim thickness and formation of droplets beyond the rim and the crater centre was also observed in the presence of magnetic field of 0.3 T (Fig. 5.7). It is reported that the vapor pressure increases as temperature increases.[181] The radial expansion of LPP along magnetic field increased as the magnetic field increased.[182] The increase in radial expansion of plasma with magnetic field leads to decrease in temperature due to adiabatic cooling. The decrease in plasma temperature may result in decrease in vapour pressure which in turn decreases recoil pressure on the melted layer. As a consequence of this, the ablation due to melt ejection is decreased. Moreover, instead of displacing the melted mass around the crater it is accumulated inside the crater resulting in decrease in depth. Therefore, the ablation due to the vapor pressure is lowered at higher magnetic field of 0.5 T.

The shock pressure of Cu and Al plasma by taking air as ambient in each case was calculated using eqn. (2.3). The shock impedance for the surrounding and the target are: $Z_{air}$(shock) = 40 g/cm$^2$ s and $Z_{Cu}$(shock) = 5.46 × 10$^6$ g/cm$^2$ s.[108] The

calculated pressure of copper-air ambient system is, therefore, 47.33 Mpa. Similarly, the shock pressure of aluminum-air ambient system with $Z_{Al}$(shock) = $1.5 \times 10^6$ g/cm$^2$ s [13,108] is found to be 47.32 Mpa which is very close to that of Cu. The plasma experienced the combined effect of magnetic field confinement and spatial confinement of air. The plasma expansion is decelerated by magnetic field. Therefore, the action of shock impact on molten layer of the irradiated portion will be retained for duration longer than that without magnetic field. This may help to increase the ablation via melt ejection. Moreover, in the presence of magnetic field, due to the magnetic confinement of plasma, the temperature and pressure of the plasma is higher than in the absence of magnetic field which makes the molten layer of the metal less viscous. As a result of this, the intense shock wave is induced and eventually impulsive force acts on the target [13] resulting in more ablation rate and hence depth in the presence of magnetic field.

### 5.3. Surface characterization of deposited nanoparticles on Cu target

In order to explore the effect of magnetic field on NPs formation on Cu target due to IPLD, the laser-ablated Cu target surface was subjected to FESEM, XRD, photoluminescence, and laser Raman spectroscopy. The FESEM images of laser ablated target surface in the absence and presence of $B$ = 0.3 T are shown in Fig. 5.8. The surface consists of two parts: region A (around the crater at a distance of 1.6 mm from the center of the crater) and the crater region B (crater formed due to direct laser exposure). Region A was formed due to the re-deposition of the particles from laser-induced Cu plasma plume. The FESEM images reveal that more NPs were formed in the region A as compared with that in the crater. When the laser ablation takes place, the plasma plume expands perpendicular to the target surface. Owing to high ambient

pressure, a portion of the ablated plume returns back due to collisions between the target plasma particles and ambient gas.[117]

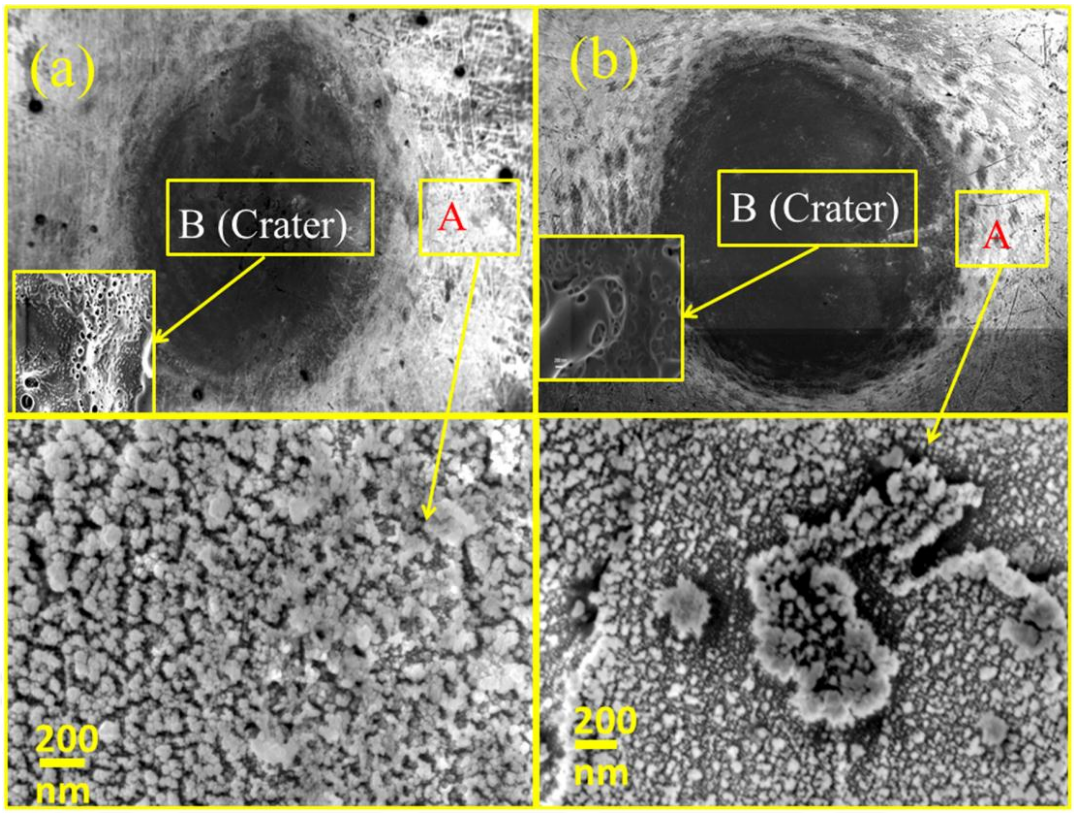


**Fig. 5.8.** FESEM images of nanostructured surface at (a) $B = 0$ and (b) $B = 0.3$ T.

The backward flux of the ablated mass is deposited on the target in the form of the nanostructure which is known as IPLD.[183] The role of $B$ in IPLD can be understood as follows. The presence of the external $B$ changes the plasma particle diffusion pattern. The particles diffuse along the $B$ direction due to their mobility but in the transverse direction in steps of Larmor gyro-radius.[48] Due to this confinement more particles undergo backscattering and redeposit on the target. The higher temperature of plasma in the presence of the $B$ results in large number of collisions and backscattering and eventually in turn increases inverse deposition. Above all, at a

later time of plasma expansion, the plume starts expanding mainly in radial direction. Therefore, the density of species becomes higher in the lateral plume front of the plasma. This high pressure gradient along the lateral direction and the viscosity effect result in the formation of two vortices at the plume periphery, viz., backscattering of ablated particles with circular motion. This phenomenon is observed at atmospheric air pressure.[90] In the presence of *B*, the diamagnetic drift arises due to the pressure gradient in the plasma. This drift is given by the relation[149] $V_d = -\frac{\nabla p \times \mathbf{B}}{q n_e B^2}$ where $q$ is charge of the plasma specie; $\nabla p$ is the pressure gradient. As the plasma expands, the density gradient arises along the expansion direction. It enhances more plasma species drifting to the lateral direction at a later time of plasma expansion. This overall phenomenon of high air pressure and *B* may cause the formation of different structures in the vicinity of the ablated crater on Cu target.

The crystallinity of the deposited region on Cu target was examined using XRD. Fig. 5.9 shows the XRD pattern of the laser ablated Cu target surface. The diffracted peaks obtained at $2\theta$ = 34.9° and 38.8° correspond to CuO nanoparticles which are attributed to miller indices[184] (002) and (111), and those peaks at 43.4° and 50.5° correspond to Cu nanoparticles (NPs) peaks[48] corresponding to the miller indices (111) and (200) of unirradiated Cu, respectively. The diffracted peak at $2\theta$ = 30° corresponds to (110) of $Cu_2O$ phase. The mean crystallite size and strain of crystal planes were estimated from eqn. (2.24) and (2.25). The calculated mean crystallite size in the absence of the *B* was 20.5 nm. However, in the presence of the *B*, it was found to be 22.9 nm. The two peaks at 43.4° and 50.6° of ablated target are shifted slightly due to strain produced in the lattice.

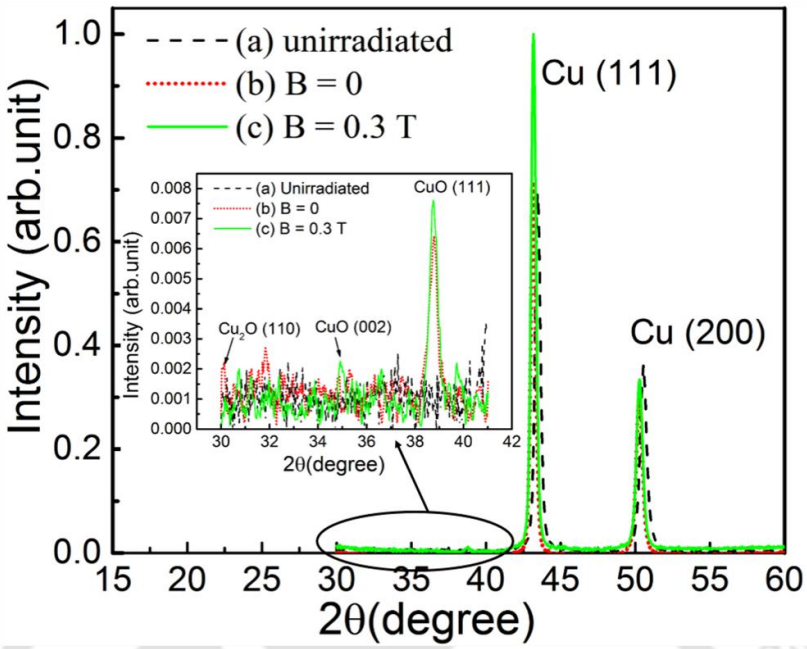


**Fig. 5.9.** XRD pattern of (a) unirradiated copper, laser ablated copper at (b) *B* = 0, and (c) 0.3 T.

The strain for the plane Cu (111) and Cu (200) of the laser-irradiated Cu surface in the absence of the *B* are, respectively, of the order of $10^{-3}$ and $10^{-2}$. It shows similar values in the presence of the *B* indicating that the *B* does not play any significant role in producing strain in re-deposited metal. In the case of the *B*, the XRD peak intensity of CuO at 38.8$^{o}$ and 34.9 was more pronounced as compared to that of without *B*. This is attributed to more crystallized CuO nanoparticles formation in the plane (111) in the presence of *B*. The diffracted peak intensity of $Cu_2O$ was lowered in the presence of *B* while the intensity of CuO increased which shows the transformation of $Cu_2O$ to CuO phase. This transformation mechanism is similar to the transformation of $Cu_2O$ to CuO when the substrate temperature is increased during PLD.[5] The oxidation of Cu can be seen as follows. $4Cu + O_2 = 2Cu_2O$ and $2Cu_2O + O_2 = 4CuO$. When the oxidation of Cu occurs, the major product is $Cu_2O$. The CuO

forms at high temperature through the second reaction.[185] In the presence of *B*, more heat is transferred to the target which increases the temperature of target and induces a high temperature environment around the target. As a result, the amount of $Cu_2O$ decreases while the CuO is increased. During laser ablation, the temperature of the region where the deposition occurred was around 391-755 °C.[140] The increase in temperature of Cu target that caused the transformation of $Cu_2O$ to CuO is also in agreement with the results obtained from photoluminescence and Raman spectrum. In the presence of *B*, the intensity of the Cu NP peak at 43.4$^o$ is higher which means more Cu NPs are formed in the lattice plane (111). In the laser ablation of Cu without *B*, more CuO nanoparticles are formed in the region A than in the crater region B.[19] The oxygen from air in the vicinity of high temperature plasma gets atomized and combines with the Cu atom and subsequently favors the formation of CuO. Lee et al. have reported the presence of Cu ions and atoms near the ablated Cu surface.[186] Misra et al. reported that the Cu atoms or ions could reach the edge of the crater and easily oxidize leading to the formation of Cu/CuO/$Cu_2O$ nanoparticles. The Cu oxide so formed gets deposited on the target itself.[187] The formation of the Cu oxide around the laser ablated crater was observed. This is attributed to the combined effect of high atmospheric pressure and magnetic confinement of plasma. More Cu atoms stay near the target surface due to magnetic confinement of plasma. The re-deposited Cu oxide nanostructure in the absence of *B* is found to be quite identical to the nanostructure obtained via laser ablation of Cu. [19]

Since, the X-ray peak of CuO was noisy, the Raman and photoluminescence spectroscopy of the deposited particles were also studied to confirm the formation of

copper oxide nanoparticles. The Raman spectra of the target surface in the absence and the presence of the *B* is shown in Fig. 5.10. The Raman spectra were recorded from region A. It depicts three Raman active modes ($A_g$ + 2 $B_g$) of CuO and three Raman peaks of $Cu_2O$. [188] The peak at 301.1 $cm^{-1}$ corresponds to $A_g$ mode while the remaining two peaks at 348.4 and 638.2 $cm^{-1}$ as $B_g$ modes of CuO in the absence of the *B*. However, in the presence of the *B*, the peak at 300.0 $cm^{-1}$ was assigned as $A_g$ and other two peaks at 348.4 and 647.3 $cm^{-1}$ as $B_g$ modes, respectively. The characteristic peaks of $Cu_2O$ were observed at 109.0, 149.5, and 219.8 $cm^{-1}$, respectively. The first peak of $Cu_2O$ corresponds to inactive Raman mode. The second peak is due to Raman scattering from phonons of symmetry.

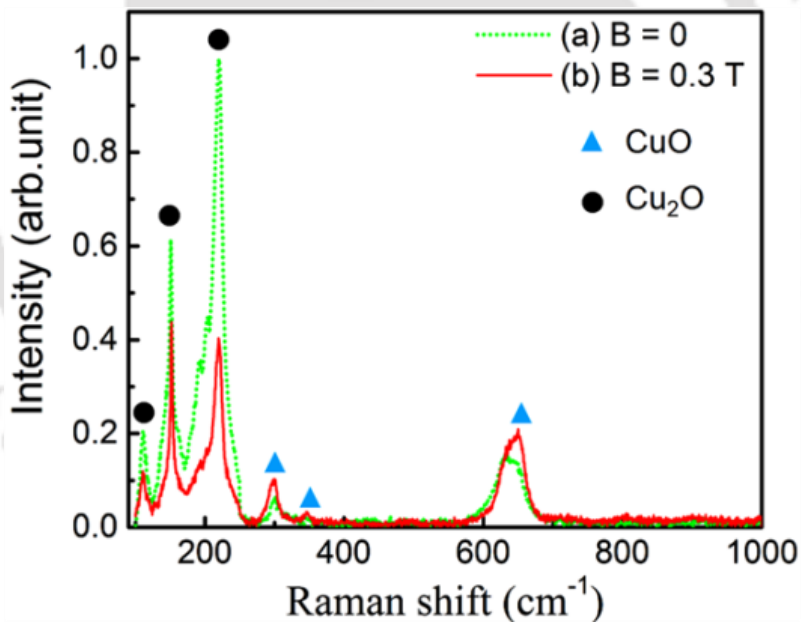


**Fig. 5.10.** Raman spectra of laser-ablated copper target surface at (a) *B* = 0 and (b) *B* = 0.3 T.

The third strongest peak is attributed to second-order Raman-allowed mode of the $Cu_2O$.[189] In the presence of *B*, the peak intensity (CuO) is higher than that of

without the *B*. However, the intensity of peaks ($Cu_2O$) is reduced significantly which is more likely due to phase transformation of Cu oxide from $Cu_2O$ to CuO. The intensity of Raman scattering depends on the number of scattering centers present in the volume of the sample where the laser beam illuminated. The increase in intensity of CuO peak signifies the increase in number of CuO particles. Therefore, by application of external *B* in LPP the crystallite size on the target can be controlled. It also can be used to transform $Cu_2O$ to CuO.

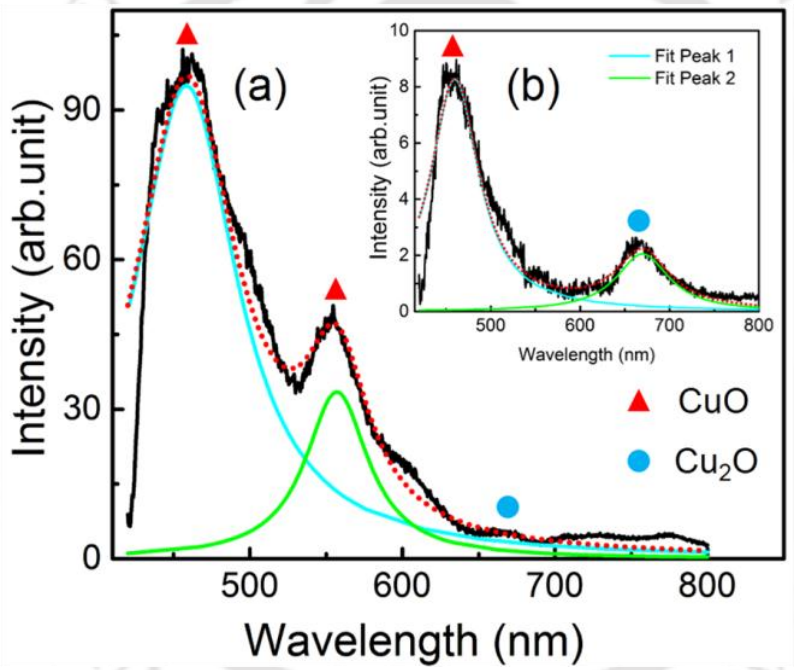


**Fig. 5.11.** Photoluminescence spectra at (a) *B* = 0.3 T and (b) *B* = 0 T (inset).

The ablated surface of Cu at *B* = 0 and 0.3 T was also analyzed using photoluminescence spectroscopy (PL). The excitation wavelength of laser used for PL studies was 405 nm. Fig. 5.11(a) and (b) show the PL spectra of the deposited nanoparticles in the presence and absence of *B* = 0.3 T. In the absence of the *B*, the PL spectrum shows two emission peaks at 459.9 (blue range emission) and 669.9 nm (red

range emission), respectively. These two peaks correspond to CuO and $Cu_2O$.[190] A broad red emission at 669.9 nm of $Cu_2O$ in PL spectrum is probably due to transitions between valence band and conduction band in $Cu_2O$ nano crystals.[191] It is more likely due to acceptor-related luminescence. The broad blue range emission centred at 459.9 is to the near-band-edge- emission. In the presence of *B*, in addition to above two peaks, the third peak appeared at 556.9 nm (green range emission) which is attributed to emission of CuO. It arises from singly ionized oxygen vacancy. It is due to the recombination of photo generated hole and electron in valence band. The intensity of first peak (CuO) is increased while that of $Cu_2O$ decreased considerably in the presence of magnetic field which is also in agreement with both XRD and Raman spectra.

### 5.4. Studies on melt ejection of Cu in the presence of uniform and non-uniform magnetic field.

The structure of the irradiated Cu surface (70 laser shots) in the absence and presence of uniform/non-uniform (NU) magnetic field in air was analyzed using FESEM and surface profilometer. Fig. 5.12(a) shows the FESEM image of crater in the presence of NU magnetic field. The irradiated region is divided into four regions as shown in Fig. 5.12(a): region I (crater center), region II (crater wall), region III (crater rim), and region IV (crater peripheral region). Fig. 5.12(b) shows the 2D depth profiles of the craters at $B$ = 0, 0.3 T, and NU magnetic field. The ablated volume was estimated from the crater surface profile and its variation at different magnetic field conditions is shown in Fig. 5.12(c). The ablated volume increased as the magnetic field changed from $B$ = 0 to non-uniform condition. The increase in melt ejection and instability caused the maximum ablated volume at NU magnetic field. Fig. 5.13

shows the FESEM image of the central portion (region I indicated in Fig. 5.12(a)) of the crater induced by laser at $B$ = 0, 0.3 T, and NU. The right column in Fig. 5.13 shows their corresponding EDX spectra. The generation of cracks and pores (red circles in Fig. 5.13(a)) were observed inside the crater at $B$ = 0. A lesser number of pores were observed in the presence of uniform (0.3 T) magnetic field. In the presence of NU magnetic field both cracks and pores were not observed.

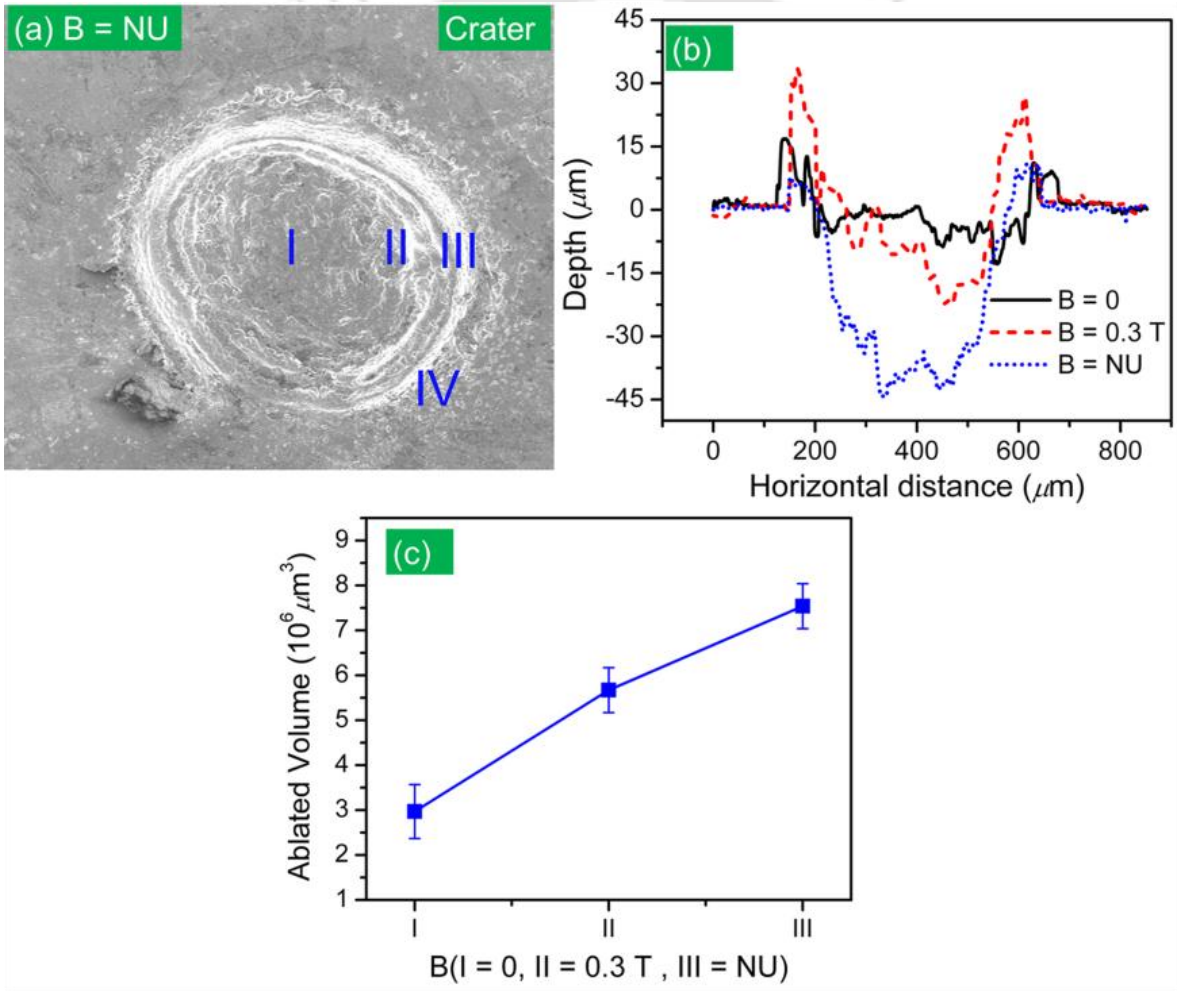


**Fig. 5.12**. (a) FESEM image of crater in the presence of NU magnetic field; (b) 2D depth profiles at $B$ = 0, 0.3 T, NU, and (c) variation of ablated volume at different magnetic field conditions.

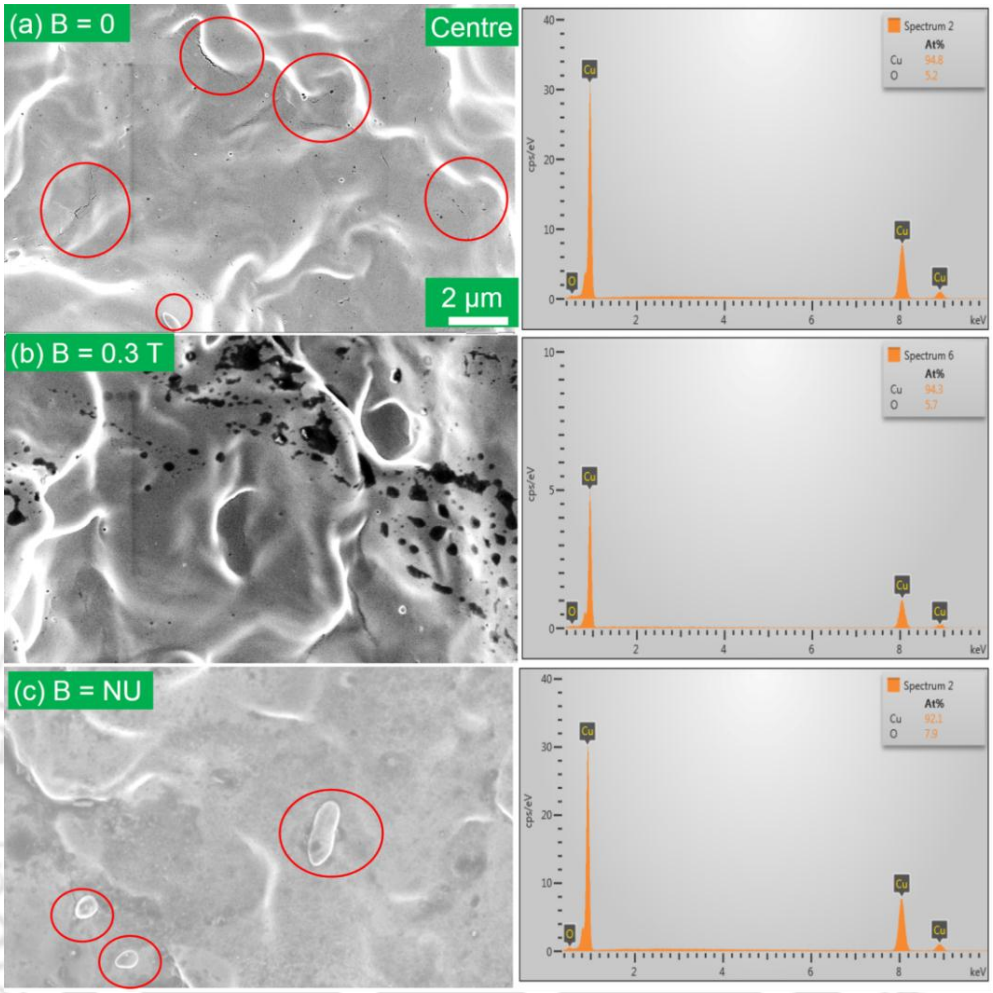


**Fig. 5.13.** FESEM images of crater center at (a) $B$ = 0, (b) $B$ = 0.3 T (uniform), (c) $B$ = NU, and their corresponding EDX spectra (right column).

The cracks observed in the crater surface are attributed to the thermal stress. The nanosecond laser ablation is mainly caused by melt ejection. The remaining melted layer is solidified in the surface of the crater. While cooling takes place, the upper surface of the melted layer condensates faster than the inner surface.[192] This difference in the cooling rates between inner and outer surfaces of the layer generates thermal stress. The thermal stress ($\sigma_{th}$) is directly proportional to the average change

in temperature ($\Delta T$) in the melted layer and is given by the relation[193] $\sigma_{th} = \left( \frac{Y \alpha_{th} \Delta T}{2(1-\nu_p)} \right)$

where $Y$ is the Young's modulus, $\alpha_{th}$ is the coefficient of thermal expansion, and $\nu_p$ is the Poisson ratio. In the absence of magnetic field, the plasma expands in air and eventually the electrons collide with the gas molecules of air resulting in rapid decrease in the plasma temperature. However, in the presence of magnetic field the plasma is decelerated and its temperature is also higher. As a result, more heat is transferred to the molten layer which minimizes the differences in cooling rates between inner and upper surfaces of the molten layer. These differences in cooling rates in the absence and presence of magnetic field are the main cause of generating cracks/no cracks on the solidified layer of the crater without/with magnetic field. The black spots observed in the crater surface in the presence of uniform magnetic field were not observed in the absence and presence of NU magnetic field. From the EDX analysis, it is observed that the percentage of oxygen at crater center is, respectively, 5.2, 5.7, and 7.9 % in the absence, presence of uniform and NU magnetic fields, respectively. As the distance increased from the crater center to the peripheral region, the percentage of oxygen increased in all the cases. More mass was deposited on the crater wall (region II) in the absence of magnetic field while lesser mass was deposited in the presence of uniform and NU magnetic field (Fig. 5.14). The mass deposited on the wall is attributed to the displacement of melt layer from the crater center towards its wall. The ablated vapor or plasma exerts recoil pressure on the melt layer.[114] This resulted in radial outflow of molten layer towards the wall and then deposited at the rim and the wall. The molten layer on the wall was solidified due to the cooling via conduction of heat into the wall. The ellipsoidal and pointed structures

(red circles in Fig. 5.14(a)) were formed on the crater wall in the absence of magnetic field. These structures were not observed in the presence of uniform and NU magnetic field.

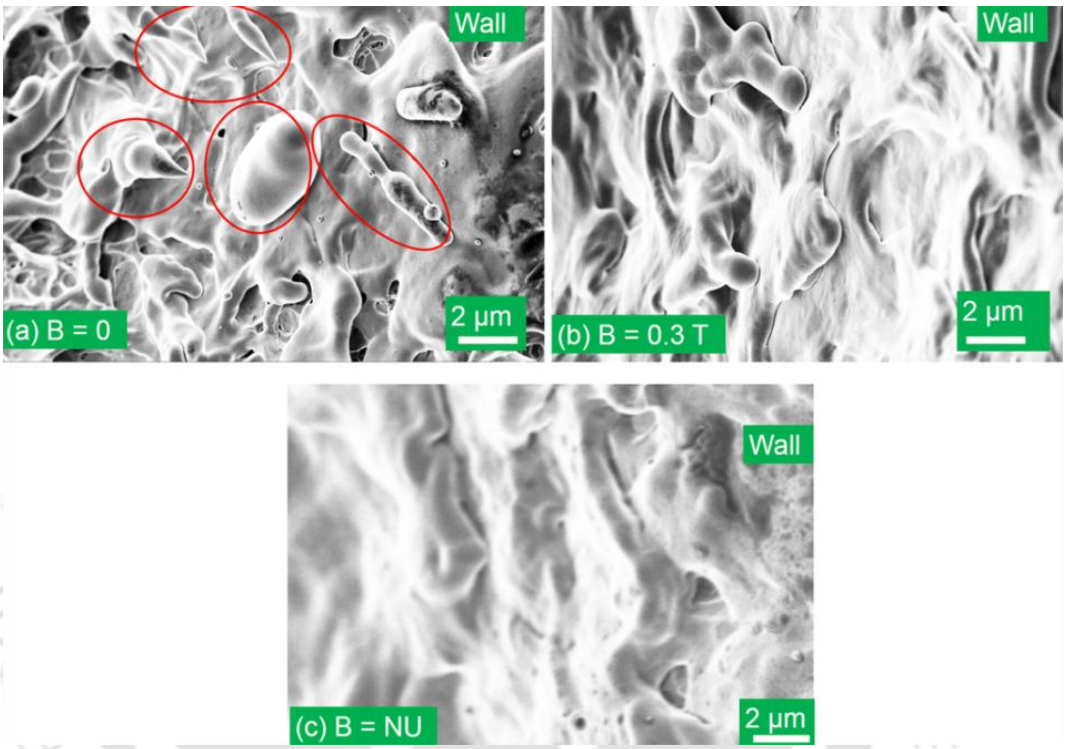


**Fig. 5.14.** FESEM images of crater wall at (a) $B$ = 0, (b) $B$ = 0.3 T, and (c) $B$ = NU.

The wall of the crater in the presence of NU magnetic field showed relatively smooth surface than that with uniform and without magnetic field. It is more likely due to the difference in the velocity of radial outflow of molten layer in the absence and presence of magnetic field. The recoil pressure of ablated mass/plasma is higher in the presence of magnetic field than that without magnetic field.[114] As a result, the radial outflow velocity is high in the presence of magnetic field and solidified at the rim instead of on the wall. The ripple structure was formed near the wall in the absence and presence of NU magnetic field. The ripple structures were created due to

the excitation of KH instability in the melted layer.[194] The FESEM images of the rim (region III) and peripheral (region IV) of laser-induced crater at $B$ = 0, 0.3 T, and NU are shown in Fig. 5.15 and 5.16, respectively. The corresponding EDX spectra are shown in the right column of the respective figures. The mass deposited at the rim was also more in the presence of NU magnetic field. The structure at the rim at $B$ = 0 was quite different compared with that in the presence of uniform and NU magnetic field (Fig. 5.15).

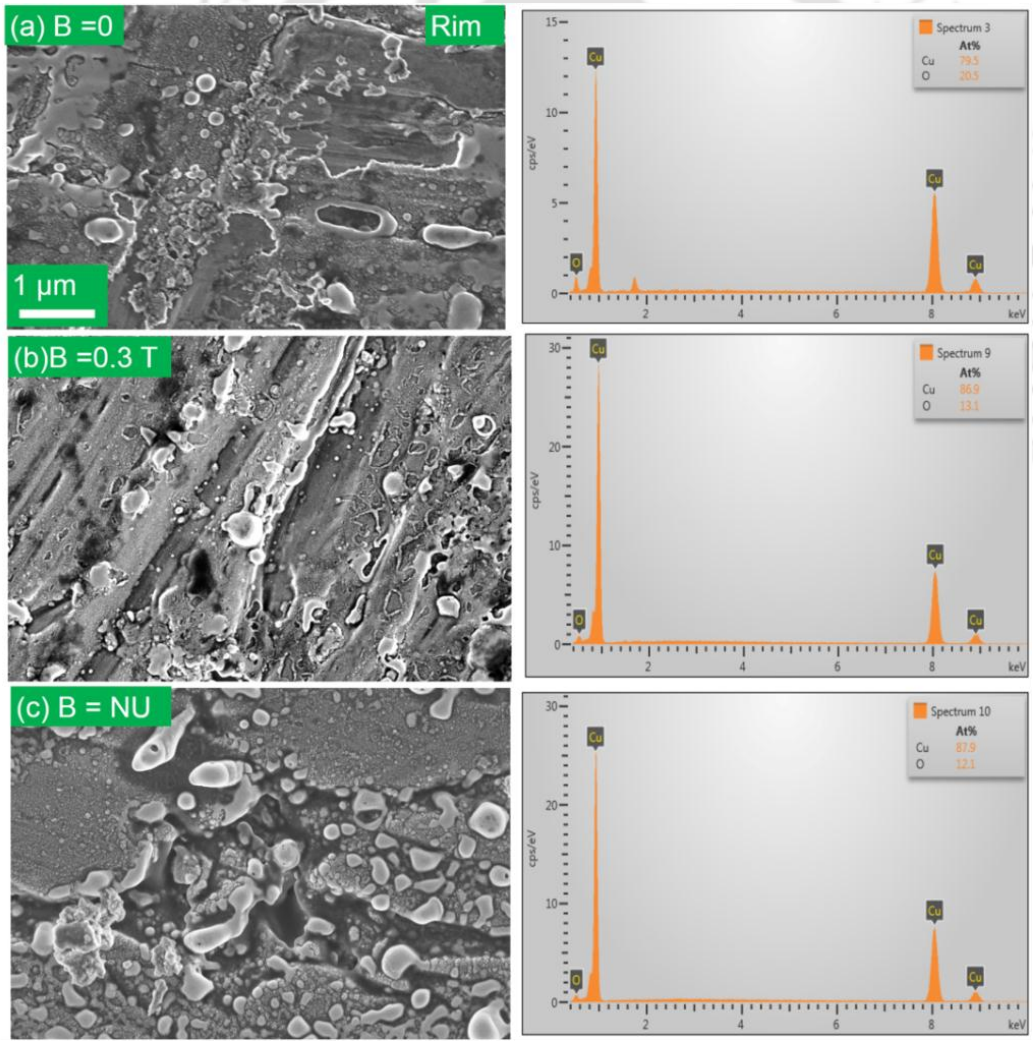


**Fig. 5.15.** FESEM images of crater rim at (a) $B$ = 0, (b) $B$ = 0.3 T (uniform), (c) $B$ = NU and their corresponding EDX spectra (right column).

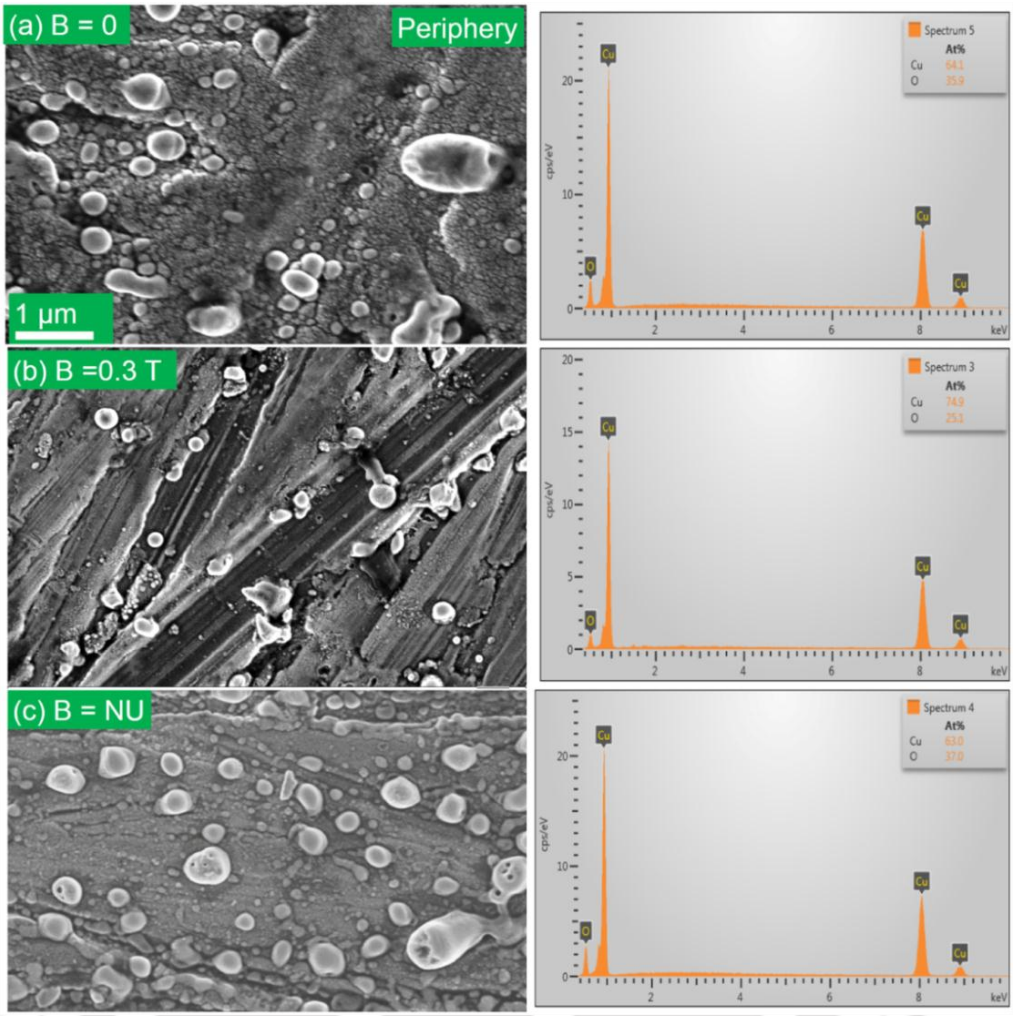


**Fig. 5.16.** FESEM images of crater periphery at (a) $B$ = 0, (b) $B$ = 0.3 T (uniform), (c) $B$ = NU and their corresponding EDX spectra (right column).

The spherical particles observed at the rim in the presence of magnetic field were not observed in the absence of magnetic field. In the peripheral region, the number of spherical particles increased in the presence of NU magnetic field. A large variation in particle size deposited at the peripheral region in the absence of magnetic field was observed compared to that in the presence of uniform and NU magnetic field. The formation of nanoparticles in nanosecond laser ablation is attributed to the condensation of ablated mass flux.[113,115]

The hydrodynamic sputtering and instability of the melted layer result in the formation of micro-particles.[88] The minimum size of droplets that can be generated by melt ejection and instability was determined using eqn. (2.21). Using $\alpha_{th}\Delta T$ = 0.033 K, $\Delta t$ = 7 ns, $\gamma$ = 1.3 $Jm^{-2}$, $\rho_s$= 8960 $kgm^{-3}$, $\rho_l$ = 8000 $kgm^{-3}$ the minimum size of the droplet to be expelled out is found to be around 0.68 $\mu$m. Based on this model, two fractions of particle distributions are created by two mechanisms: (i) smaller particles (< 0.68 $\mu$m) are produced due to condensation of ablated vapor or plasma and (ii) larger particles (≥ 0.68 $\mu$m) are generated by the hydrodynamic sputtering and instability. The maximum surface temperature was obtained from the laser heating simulation based on 2D heat conduction equation as discussed in chapter 6. The temporal evolution of surface temperature on target and vapor pressure is shown in Fig. 5.17. Using surface temperature, the evolution of vapor pressure in the absence and presence of magnetic field is calculated using Clausius-Clapyron equation and modified Clausius-Clapyron equation as discussed in chapter 6.[114] The vapor pressure in the presence of magnetic field is higher than that of without magnetic field.

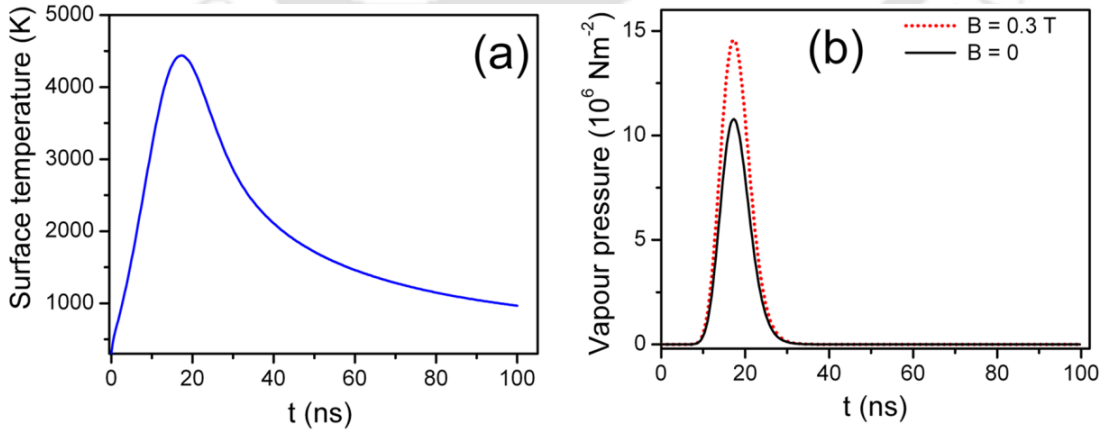


**Fig. 5.17.** Temporal evolution of (a) surface temperature (b) vapour pressure with and without magnetic field.

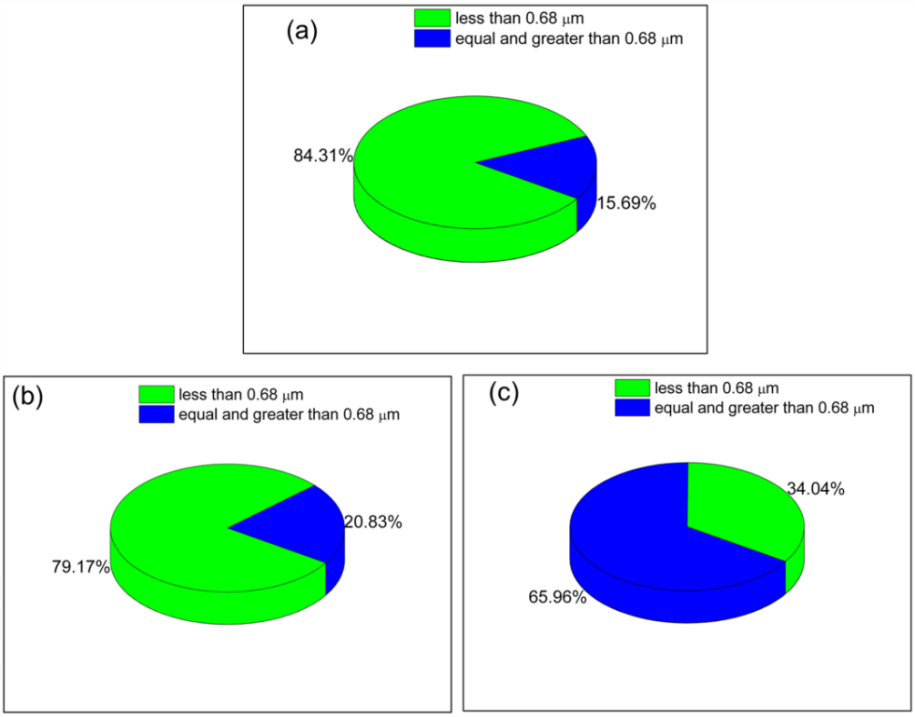


**Fig. 5.18.** Pie chart of percentage of number of particles of size less than 0.68 $\mu$m and $\geq$ 0.68 μm at (a) $B$ = 0 (b) $B$ = 0.3 T (c) $B$ = NU.

Using imageJ 1.14 software the particle/droplet size was measured from the FESEM images. The pie chart (Fig. 5.18) shows the percentage of particles (in peripheral region) with size less than as well as equal and greater than the minimum size of the droplet (i.e. 0.68 $\mu$m). In the presence of magnetic field of 0.3 T, the percentage of larger particles ($\geq$ 0.68 $\mu$m) was increased by 5.1 % while that of smaller particle (< 0.68 $\mu$m) decreased nearly by 5.1 %. However, in the presence of NU, the percentage of larger particle was increased significantly (50 %) while the smaller particle was decreased by 50 %. This indicates that in the presence of magnetic field, the recoil momentum onto the melted liquid surface is higher than that without magnetic field. As a result, more mass was expelled out in the presence of magnetic field. Laser ablation of Cu and Al targets in the presence of magnetic field

also showed that more mass is ablated in the presence of the magnetic field.[114] The other possibility is the excitation of KH and RT instability in the interface between the melted liquid surface and the ablated vapor or plasma. Ang et al. also showed that the ripple structure and large mass ejection is due to KH instability.[194] Depending on the different temperature and density of the ambient, the ejected droplets /mass present in the plasma may result in the formation of different forms of oxides.

The KH instability occurs when there is relative velocity between plasma and molten liquid provided the relative velocity is greater than a critical velocity given by eqn. (2.6). Using $\sigma$ = 1.315 $Nm^{-1}$, $\rho_l$ = 8000 kg $m^{-3}$, $\rho_v$ = 18.0 kg $m^{-3}$ at $B$ = 0 (estimated from vapor pressure and surface temperature of Cu using $\rho_v = \frac{P_{vap}}{k_B T_s}$) in eqn. (2.6), the critical velocity was found to be of around 5 m/s. The maximum vapor pressure and surface temperature in the absence of magnetic field were 1.08 × $10^7$ $Nm^{-2}$ and 4450 K, respectively. Therefore, the tangential velocity estimated from (2.7) in the absence and presence of magnetic field were, respectively, around 52 and 60 m/s which are greater than the critical velocity for KH instability which signifies the occurrence of KH instability. The estimated minimum size of the particle generated due to the KH instability is 0.681 $\mu$m which is in agreement with the proposal introduced by Kelly et al.[113] as well as the particle size obtained experimentally. However, in the presence of magnetic field the minimum particle size was found to be slightly less i.e. around 0.5 $\mu$m. From the FESEM images, it was observed that those large particles (1 $\mu$m) observed in the absence of magnetic field were not seen in the presence of magnetic field. It is more likely due to the breaking of large droplets as a result of high recoil pressure exerted on the liquid layer.

In the presence of magnetic field, the acceleration of perturbation growth due to RT instability (estimated from eqn. (2.10)) was around $6.8 \times 10^9$ cm/s$^2$ which is larger than that in the absence of magnetic field (i.e. $5.7 \times 10^9$ cm/s$^2$). The size of particles produced by RT instability was estimated from eqn. (2.9) and it was therefore found to be around 0.8 $\mu$m. Fig. 5.18 shows that when the magnetic field condition changes from uniform to NU magnetic field there was a drastic change in number of particles ($\geq$ 0.68 $\mu$m). This can be explained by considering the drift motion plasma species in the presence of magnetic field. In the presence of uniform magnetic field, the electrons and ions are separated in opposite direction inducing electric field ($E$). In this condition, the charge particles drift with a velocity equal to $E/B$ in the direction perpendicular to both fields. This drift velocity is independent of charge and therefore the electrons and ions move in the same direction. As a result of this, the electron and ion recombination is increased and hence the number of atoms.[58] This in turn enhances the intensity of atomic line which discusses in the OES later. In this case, the plasma is decelerated significantly across magnetic field whereas it continues along the magnetic field. The melted liquid layer also traverses along the wall. Therefore, there is a relative motion between the vaporized mass or plasma and liquid layer which may excite the KH instability. In the presence of NU magnetic field, there is an additional drift due to curvature and gradient of the magnetic field.[149] This additional drift along the radial direction enhances the relative motion of plasma over the liquid which may intensify the KH instability leading to an increase in number of large particles in the presence of uniform and NU magnetic field. Further, the vapor pressure in the presence of magnetic field is higher resulting in more recoil

pressure. The increase in recoil pressure enhanced tangential velocity of the liquid and ejection/splashing of melted mass.

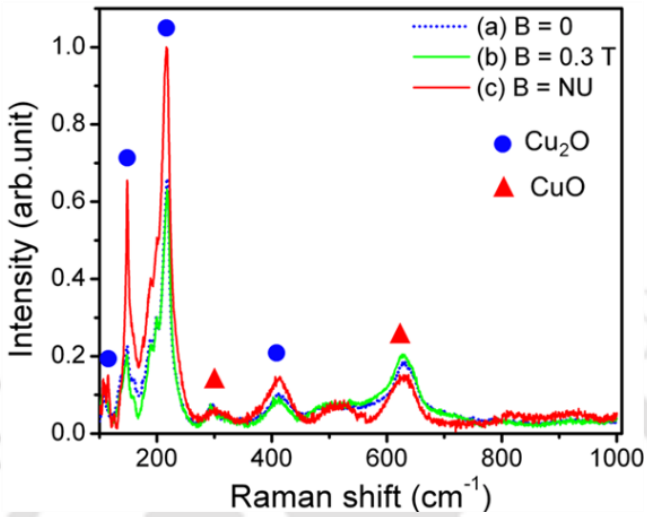


**Fig. 5.19.** Raman spectra of periphery region of crater at (a) *B* = 0 T, (b) *B* = 0.3 T, and (c) *B* = NU.

The ablated surface (peripheral region) was also studied using Raman spectroscopy. Fig. 5.19 depicts the Raman spectra of rim of the laser ablated crater. From the Raman spectra it was observed that the deposited region consists of CuO and $Cu_2O$ nanoparticles. The characteristic peaks of $Cu_2O$ at 109.0, 149.5, and 219.8 $cm^{-1}$, respectively, were observed. The another peak at around 413 $cm^{-1}$ was also observed. The origin of this peak is not known but it is more likely due to $Cu_2O$.[195] The peaks at 301.1, 348.4 and 638.2 $cm^{-1}$ correspond to CuO. The intensity of $Cu_2O$ peaks changes quite significantly in the presence of the magnetic field. This could be due to an increase in the number of $Cu_2O$ particles which also confirmed from the FESEM images and EDX.

OES of plasma was also studied and an attempt was made to correlate plasma parameters with the ablation studies. Fig. 5.20(a) shows the spectra of Cu atomic and

ionic transitions at $B$ = 0, 0.3 T, and NU magnetic field. The intensity of Cu I transitions enhanced in the presence of magnetic field. However, the enhancement is more pronounced in the presence of uniform magnetic field of 0.3 T than in the NU field. The electron density of LPP was estimated using eqn. (2.15). Fig. 5.20(b) shows the variation of electron density at $B$ = 0, 0.3 T, and NU. The electron density at $B$ = 0, 0.3 T and NU magnetic field are, respectively, $(5.5 \pm 0.2) \times 10^{16}$, $(7.4 \pm 0.2) \times 10^{16}$, and $(6.3 \pm 0.2) \times 10^{16}$ $cm^{-3}$. The electron density in the presence of NU magnetic field was lower than that in the presence of uniform magnetic field of 0.3 T. However, it was higher than that without magnetic field. The decrease in electron density in the presence of NU magnetic field could be due to the increase in ejection of droplets in the presence of NU magnetic field as discussed above. The incident laser radiation scattered from these droplets present in plasma in turn reduced the laser-target and laser-plasma coupling efficiency. The reduction in laser-target and laser-plasma interaction leads to a decrease in electron density. In the presence of uniform magnetic field, the increase in collisional excitation rate of atom leads to an intensity enhancement of Cu I. However, in the presence of NU magnetic field, the decrease in electron density and temperature caused lowering in electron impact excitation of atom and hence the intensity of atomic transition which is in good agreement with the recorded spectrum. The electron temperature was calculated using eqn. (2.13) Fig. 5.20(c) shows the variation of electron temperature with magnetic field. The electron temperature of Cu plasma in the absence and presence of uniform and non-uniform magnetic field are, respectively, (0.76 ± 0.01), (0.88 ± 0.01), and (0.71 ± 0.02) eV. The drastic decrease in electron temperature in the presence of NU magnetic field may be due to scattering of laser light from the ejected mass. In the presence of

magnetic field, the gyration of electrons and ions make collisions with the ablated mass resulting in a decrease in the electron temperature.

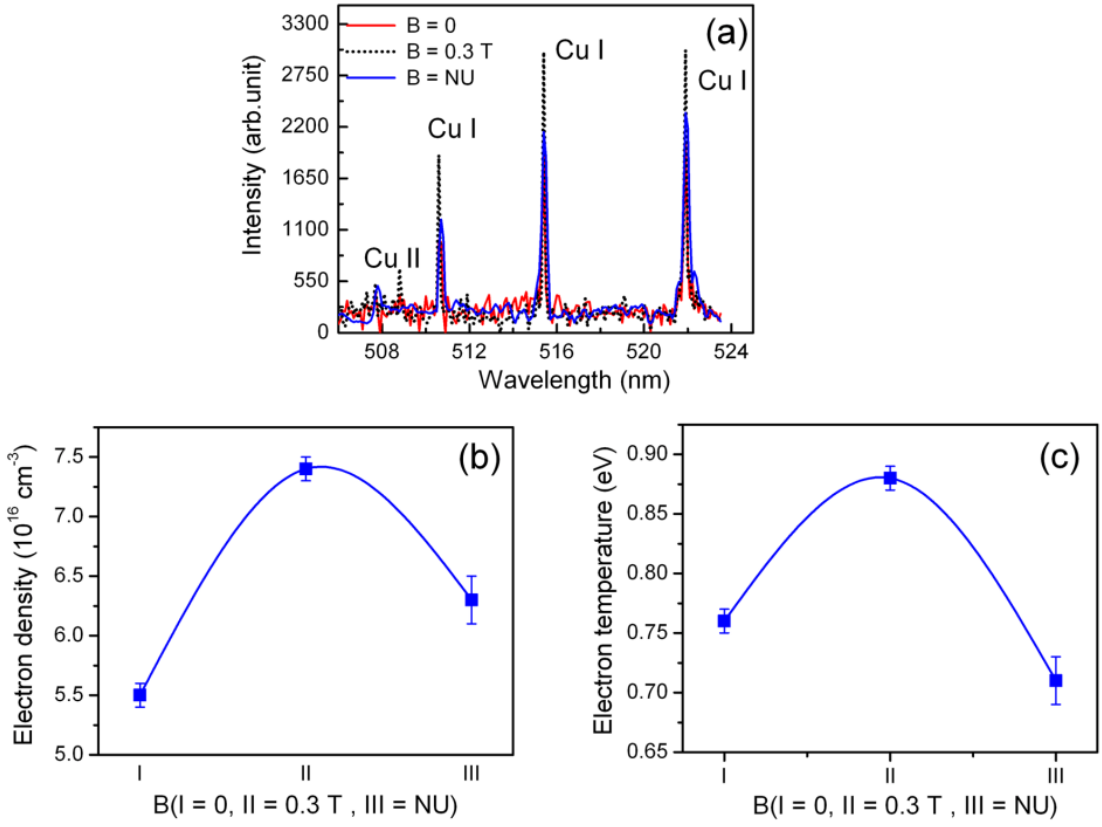


**Fig. 5.20.** (a) Spectra of copper plasma, (b) electron density, (c) electron temperature at $B$ = 0, 0.3 T, and non-unifrom magnetic field.

## 5.5. Conclusion

In this chapter the effect of static magnetic field on laser ablation of Cu and Al was discussed by varying the strength of magnetic field from 0 to 0.5 T. The ablated volume of the laser ablated crater increased with an increase in the magnetic field and then decreased on further increase in the magnetic field. However, it was more pronounced in the case of Al indicating the dependent of laser ablation on thermo-

physical parameters of the target. The increase in ablation in the presence of magnetic field is attributed to an increase in recoil pressure exerted on the melted liquid layer and heat transfer from confined plasma to target. The characterization of deposited particles at the peripheral region of the crater revealed the formation of Cu/$Cu_2O$ and CuO nanoparticles. The presence of magnetic field led to the transformation of $Cu_2O$ into CuO due to creation of a relatively hot environment of plasma. The generation of larger size droplets was also observed in the presence of non-uniform magnetic field. It is ascribed to the increase in melt ejection and instability. The cracks observed in crater surface were not observed in the presence of magnetic field due to the decrease in thermal stress. From the EDX analysis it was observed that $Cu_2O$ particles were generated at higher number of laser shots. The presence of non-uniform magnetic field enhanced the Raman peak of $Cu_2O$. The OES of Cu plasma in the absence and presence of magnetic field (uniform and non-uniform) showed that the optical emission enhancement was pronounced in the presence of uniform magnetic field compared with non-uniform magnetic field. In non-uniform magnetic field, the electron temperature reduced drastically as compared to that in the presence of magnetic field due to the scattering from the ejected particulates formed in the ablated plasma. From these studies, the application of an external magnetic field enhances the laser ablation and it may be useful in controlling the phase of nanoparticles deposited due to laser ablation.

# Chapter 6

## *Numerical Simulation on Laser Ablation of Cu in the Presence of Magnetic Field*

Laser ablation and its subsequent plasma formation are complex processes. In order to explore the complex processes involved in laser ablation, the FEM has been used. The numerical simulation on laser ablation in the presence of magnetic field is not documented in the literature. In this chapter the simulation on laser heating is described and compared with the experimental results. The laser heating was simulated by taking two different metals (Cu and Al) of different thermo-physical parameters to justify the dependent of laser ablation on thermo-physical parameters which is also observed in experimental studies. From the temporal evolution of the simulated surface temperature, the plasma expansion velocity was determined. Using this expansion velocity in the conservation of energy, the stopping radius of plasma at different lens focusing distances was also estimated.

### 6.1. Simulation parameters

The detailed procedure of the FEM and mathematical formulation on laser heating is described in section 2.3. The basis of the simulation is the 2D thermal conduction equation. The temperature dependent thermo-physical parameter is considered to take into account the effect of phase transition during laser heating. The target was modeled as square in shape with dimension of 20 × 20 $mm^2$ (which is approximate dimension used in the experiment). The element type used is PLANE55. The PLANE55 is a 2D element of 4 nodes, temperature as degree of freedom, and

quadrilateral in shape. The whole domain was discretized with an element size of 0.2 mm using meshing tool. All the elements within the region where the laser beam is focused were further refined to get accurate result. The boundary and initial conditions were taken as room temperature (300 K). The intensity of laser is taken as the same as that used in the experiment i.e. $1.4 \times 10^9$ $Wcm^{-2}$. The heat conduction equation was solved over a time period of 100 ns with total number of 300 steps. To determine the stopping radius for different lens focusing distances (i.e. at $S_{-2}$, $S_{-1}$, $S_0$, $S_1$, $S_2$ as shown in Fig. 2.5(b)), the temporal evolution of surface temperature was simulated using the laser radiation with intensities of $0.7 \times 10^9$, $1.0 \times 10^9$, $2.8 \times 10^9$, $1.0 \times 10^9$, and $0.7 \times 10^9$ $Wcm^{-2}$.

## 6.2. Estimation of laser ablated depth

The laser ablation on Cu and Al was simulated by taking the same laser parameters as mentioned in chapter 5. Fig. 6.1 shows the simulated temporal evolution of surface temperature of Cu and Al, respectively, in the absence of magnetic field. The target surface temperature of Cu observed in the present work is in the temperature range reported in the literature.[141] The simulated result revealed that the surface temperature is higher than the vaporization of the Cu and Al (table 5.1) and it indicates that the laser ablation occurs at the laser intensity of $1.4 \times 10^9$ $Wcm^{-2}$. The maximum surface temperature of the Cu (at $t$ = 17.67 ns) is less than the corresponding temperature of Al (at $t$ = 16.33 ns). It is attributed to high thermal conductivity of Cu which drains out heat into the body from the target surface. The temperature dependent enthalpy of Cu and Al used in this simulation is available in the literature[174,196] and is shown in table 6.1. The laser ablation is

mainly due to the direct vaporization and splashing/melt ejection as discussed in chapter 5.

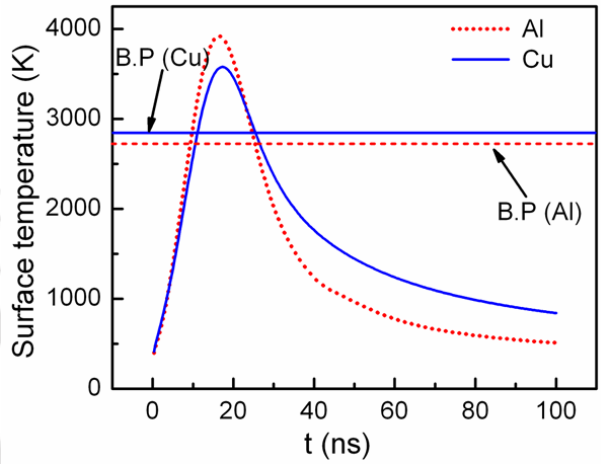


**Fig. 6.1.** Temporal evolution of surface temperature of aluminum (dotted line) and copper (smooth line).

**Table 6.1.** Temperature dependent enthalpy (*H*).

| Temperature (K) | Entahalpy $H_{Cu}$ ($10^3$ J/mol) | Temperature (K) | Entahalpy $H_{Al}$ (J/mol) |
|---|---|---|---|
| 1356 | 671 | 1081.0 | 33356.40 |
| 2000 | 1013 | 1097.8 | 34075.36 |
| 2500 | 1282 | 1208.4 | 37732.86 |
| 2750 | 1411 | 1244.9 | 38652.46 |
| 3000 | 1536 | 1384.2 | 43045.64 |
| 3500 | 1774 | 1512.1 | 47041.72 |
| 4000 | 1996 | 1647.2 | 51531.04 |

It is also reported that the profile depth is mainly due to melt ejection.[139] Further, the vaporization rate decreases with the increase in ambient pressure.[137] In

the present work, since the ablation takes place at high air pressure (760 Torr), the ablation is expected to be mainly due to the melt ejection. Therefore, only the laser ablation rate contributed by melt ejection or splashing was mainly considered. The increase in ablation depth in the presence of magnetic field is discussed as follows. The vaporization rate can be estimated from vapour pressure using eqn. (2.28). Using maximum vapour pressure obtained from the simulation, the maximum vaporization rate of Al at $B$ = 0 was 3.76 m/s. Therefore, the calculated maximum ablation depth due to vaporization for 50 pulses impinging on Al target in the absence of magnetic field was found to be 1.88 $\mu$m. In the presence of magnetic field of 0.3 T, the vaporization rate of Al was around 5.13 m/s which resulted in 2.57$\mu$m depth for 50 shots. However, the experimental depth of Al was found to be (11.9 ± 0.6) $\mu$m and (26.1 ± 0.2) $\mu$m in the absence and presence of magnetic field, respectively. For Cu, the maximum vaporization rate was 0.44 m/s and 0.61 m/s at $B$ = 0 and 0.3 T, respectively. The calculated maximum ablation depth of Cu at $B$ = 0 and 0.3 T was 0.22 and 0.30 $\mu$m, respectively. The experimentally obtained ablation depth of Cu in the absence and presence of magnetic field was (3.3 ± 0.1) and (5.2 ± 0.1) $\mu$m, respectively. Therefore, the nanosecond ablation is not mainly due to evaporation only. The ambient pressure is high air pressure and so the rate of vaporization is lowered due to high effective ambient pressure. The increase in ablation is attributed to melt ejection due to an increase in recoil pressure.

Fig. 6.2(a) and (b) shows the temperature contour of Al and Cu, respectively, at $t$ = 17.67 and $t$ = 16.33 ns after the laser pulse falls on the target during laser heating. The spatial scale embedded is taken with respect of whole target domain. The inset in Fig. 6.2 shows the zooming image of the circled region. From this contour

plot also, it is observed that the heat penetrates deeper in Al than Cu which results in more ablation. The depth due to melt expulsion can be discussed using a simple model known as ideal fluid piston effect related to the vapor pressure. The vapour pressure in the absence of magnetic field was determined using the Clausius-Clapeyron eqn. (2.29). However, in the presence of magnetic field the vapour pressure was obtained by introducing the magnetic pressure in Clausius-Clapeyron equation. The modified Clausius-Clapeyron equation is discussed in chapter 2 and is given by eqn. (2.30). Fig. 6.3(a) and (b) shows the temporal evolution of vapor pressure of Cu and Al in the absence and presence of 0.3 T magnetic field, respectively. The vapor pressure in the presence of magnetic field was 1.4 times higher than the absence of magnetic field of 0.3 T. The vapor pressure of Al is two times higher than Cu. This could be one of the reasons for observing higher laser ablation depth of Al than Cu. The maximum vapour pressure for Al at $B$ = 0 and 0.3 T were $3.8 \times 10^6$ and $5.2 \times 10^6$ $Nm^{-2}$, respectively.

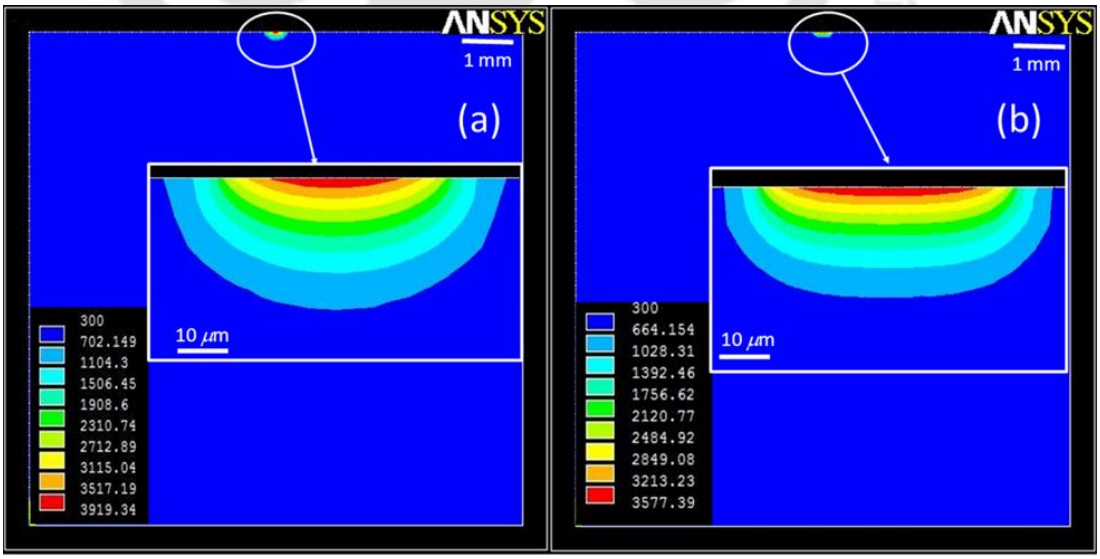


**Fig. 6.2.** Temperature contour on laser heating (a) aluminum and (b) copper.

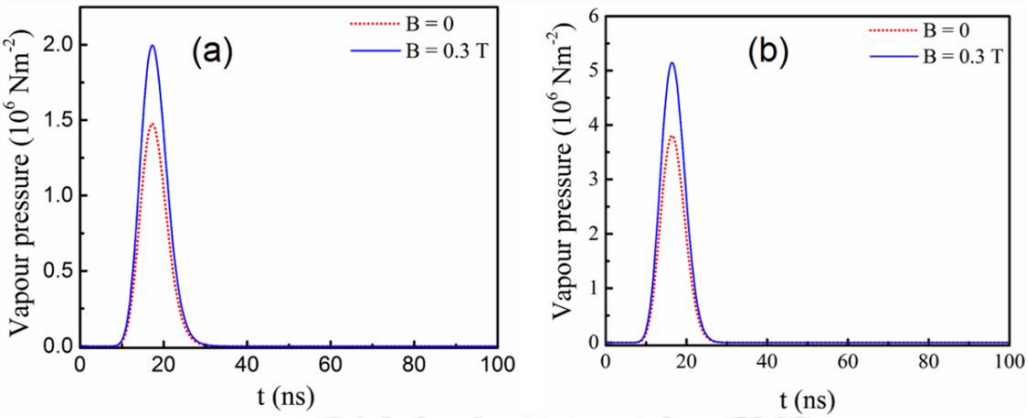


**Fig. 6.3.** Temporal evolution of vapor pressure of (a) copper and (b) aluminum.

The corresponding impulses exerted during pulse duration were, respectively, $5.1 \times 10^{10}$ and $7.0 \times 10^{10}$ $Ns^{-1}$. In the case of Cu the impulses experienced by target at $B$ = 0 and 0.3 T were $2 \times 10^{10}$ and $2.7 \times 10^{10}$ $Ns^{-.1}$ The impulse on target in the presence of magnetic field is higher than in the absence of magnetic field which results in more melt ejection i.e. due to displacement of melted mass around the crater and splashing of melted mass from the crater in the presence of magnetic field. The impulse on Al target is nearly 3 times the impulse on Cu. This could be the reason for higher ablation depth in the case of Al. The melt ejection rate was calculated from eqn. (2.7). The melt ejection rate of Cu due to piston effect in the absence and presence of magnetic field of 0.3 T was, respectively, 17.6 and 20.6 m/s and that of Al was 52.4 and 61.5 m/s. The calculated maximum ablation depth of Al for 50 laser shots in the absence and presence of magnetic field of 0.3 T was 20.9 and 24.5 $\mu$m. The ratio of ablation depth of Cu due to melt ejection and evaporation for 50 laser shots at $B$ = 0 to that at 0.3 T was 1.2. The corresponding experimental ratio was 1.5 which is close to the calculated value. For the case of Al, this experimental ratio was 2 whereas calculated value was 1.2. From the optical images of laser ablated targets

(Fig. 5.7), it was observed that at $B$ = 0 T, the thickness of rim was large and there was no ejected mass around and the centre of the crater. At $B$ = 0 T, the laser ablation is mainly due to the vaporization and melt displacement due to the piston effect. As the magnetic field was increased to 0.1 T, the mass was not only deposited around the crater but it was also scattered around the crater and centre. This indicates that increase in splashing mass in the presence of magnetic field leads to increase in recoil pressure. The calculated melt ejection ablation depth of the crater created on Cu and Al target surface in the absence and presence of 0.3 T magnetic field is listed in table 6.2. It was observed that the calculated profile depth of Al is higher than that of Cu which also shows similar trend in the experimentally observed value. The difference between the calculated value and the experimental value is due to the assumption of constant vapor pressure during the laser pulse. The other possibility is due to the re-deposition of the ablated material into the crater area as well as around the crater which is not taken into account in the case of theoretical calculation.

**Table 6.2.** Ablation depth of copper and aluminum.

| $B$ (T) | Cu ($h_{exp}$)* | Cu ($h_{th}$)** | Al ($h_{exp}$)* | Al ($h_{th}$)** |
|---|---|---|---|---|
| 0 | 3.3 ± 0.1 | 7.0 | 11.9 ± 0.6 | 20.0 |
| 0.3 | 5.2 ± 0.1 | 8.2 | 26.1 ± 0.2 | 25.0 |

* $h_{exp}$ = experimental value; **$h_{th}$ = simulated value

### 6.3. Determination of stopping radius at different lens focusing distances

The temporal evolution of surface temperature was simulated at different lens focusing distances. The different focusing conditions are depicted in Fig. 2.3(b). Fig.

6.4 shows the contour plots of temperature field at 13.7 ns after the laser pulse impinges on the Cu and the temporal evolution of surface temperature obtained from simulation.

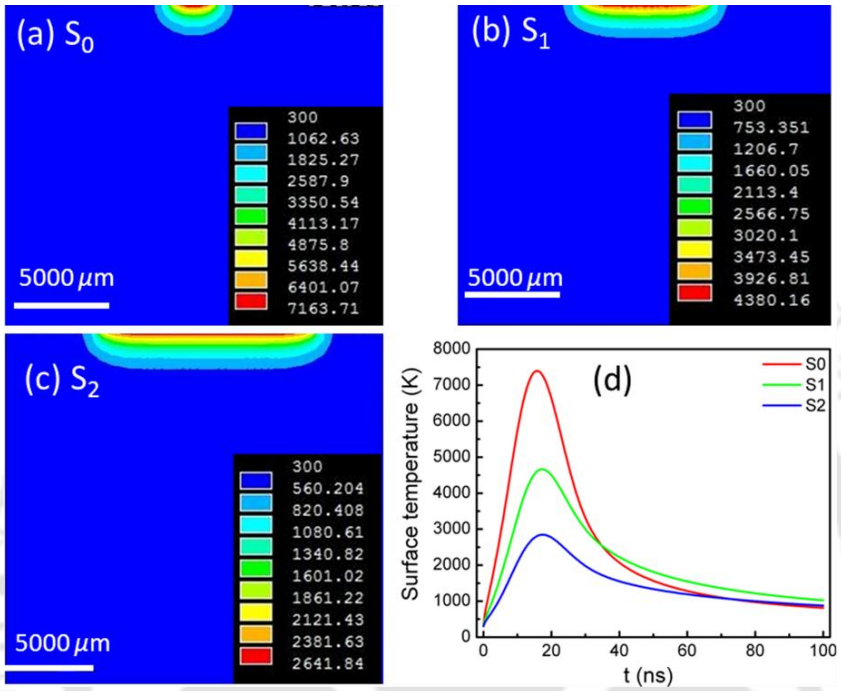


**Fig. 6.4.** Contour plot of target surface temperature (a) $S_0$ (b) $S_1$, (c) $S_2$, and (d) temporal evolution of surface temperature in the absence of magnetic field.

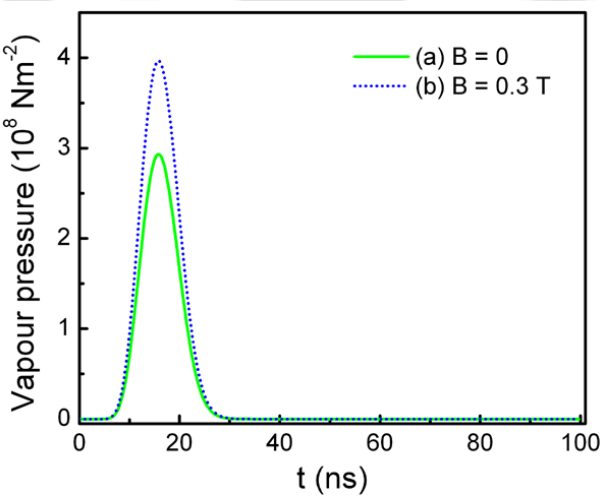


**Fig. 6.5.** Temporal evolution of vapor pressure at (a) $B$ = 0 and (b) $B$ = 0.3 T at focusing condition $S_0$.

The contour plot shows that the temperature along the depth was higher in the case of $S_0$ and therefore the depth of laser ablation was higher in the case of $S_0$. From the temporal evolution of surface temperature (Fig. 6.4(d)), it is seen that at focusing $S_0$, the target surface temperature reached up to around 7400 K (maximum) which was much higher than the melting temperature (1356 K) and vaporization temperature (2840 K) of copper. In order to calculate the total ablated mass, vaporization and melt ejection rates were determined. The vaporization and melt ejection rates depend on the vapour pressure and ambient condition. The vapour pressure at focusing condition $S_0$ in the absence and presence of magnetic field of 0.3 T is shown in Fig. 6.5. The plasma temperature ($T$) is approximately related to surface temperature ($T_s$) by the relation $T = 0.65\ T_s$. Using maximum $P_{vap}$ i.e. $3.9 \times 10^8$ Nm$^{-2}$ and $T_s$ = 7396.7 K (i.e. $T = 0.65T_s$ = 4807.9 K), $P_0 = P_{air} + P_{mag} = 1.4 \times 10^5$ Nm$^{-2}$, the vaporization and melt ejection rate in the presence of magnetic field are, respectively, 88.4 m/s and 297.6 m/s. By assuming the crater as paraboloid, the total ablated mass was estimated and it was found to be $3.1\times 10^{-8}$ kg. The plasma expansion velocity ($v$) is given by the relation[197], $v = \left(\frac{5/3k_BT}{m}\right)^{1/2}$ where $m$ is the atomic mass and $k_B$ is the Boltzmann constant. At the focusing condition $S_0$, the velocity of expansion was $1 \times 10^3$ m/s. Therefore, the total kinetic energy ($E_0$) carried by ablated mass was 15.5 mJ. At stopping radius ($R_b$), the expansion velocity was zero and from eqn. (2.22), the stopping radius becomes $R_b = \left(\frac{3E_0}{2\pi(B^2/2\mu_0 + P_{air})}\right)^{1/3}$. The stopping radius at $S_0$ was found to be 5.4 mm. Similarly, the stopping radius at focusing conditions $S_1$ and $S_2$ was determined and was found to be 2.8 and 2.1 mm, respectively. This indicates that $R_b$

depends on the focusing condition. The deceleration at focusing conditions $S_0$, $S_1$, and $S_2$ was, respectively, $9.6 \times 10^9$, $1.2 \times 10^{10}$, and $1.0 \times 10^{10}$ cm/s$^2$. The motion of neutral atom was not affected directly by magnetic field. It was decelerated due to increase in electron-neutral atom and electron-ion collision.[45]

## 6.4. Simulation on laser ablation of Cu at different fluences

The simulation was also extended at different laser fluences to investigate the effect of variation of laser fluence on laser ablation in the presence of static 0.5 T magnetic field. The main objective of this study is to justify the optimized laser fluence obtained in chapter 3. The optimization of laser fluence can be done by investigating the effect of laser fluence on ablation as well as intensity of plasma. The laser fluence is considered as optimized laser fluence at which the ablation and intensity is maximum. Fig. 6.6 shows the temporal evolution of surface temperature at different laser fluences. The surface temperature (maximum) was found to increase with laser fluence.

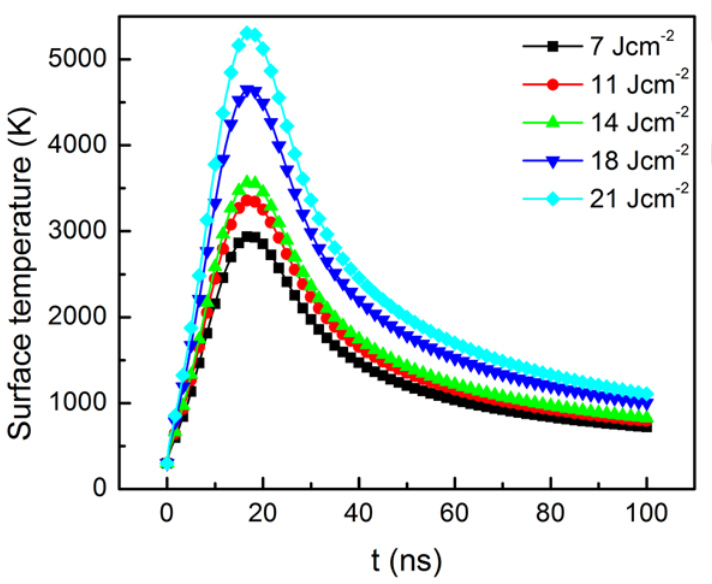


**Fig. 6.6.** Variation of simulated surface temperature with laser fluence.

It is shown in chapter 5 that the vapour pressure in the presence of magnetic field is higher than that without magnetic field and the ablation is mainly due to melt ejection. At 14 $Jcm^{-2}$ the calculated ablation rate due to vaporization in the absence and presence of magnetic field was, 0.44 and 0.85 m/s and corresponding melt ejection rate was, respectively, 17 m/s and 25 m/s. This shows that the ablation is mainly due to melt ejection. By assuming the crater as paraboloid with radius equal to spot radius (≈ 190 $\mu$m) and height (≈ total ablation rate times pulse duration), the estimated crater volume in the absence and presence of magnetic field was $4.82 \times 10^5$ and $7.33 \times 10^5$ $\mu m^3$, respectively. The experimentally estimated values was around $3 \times 10^5$ and $7.81 \times 10^5$ $\mu m^3$ which are close to simulated values validating the simulation. In experimental study, the craters were generated on copper target in the absence and presence of magnetic field by impinging 50 laser shots at laser fluences 7, 11, 14, 18, and 21 $Jcm^{-2}$ to calculate the ablation rate.

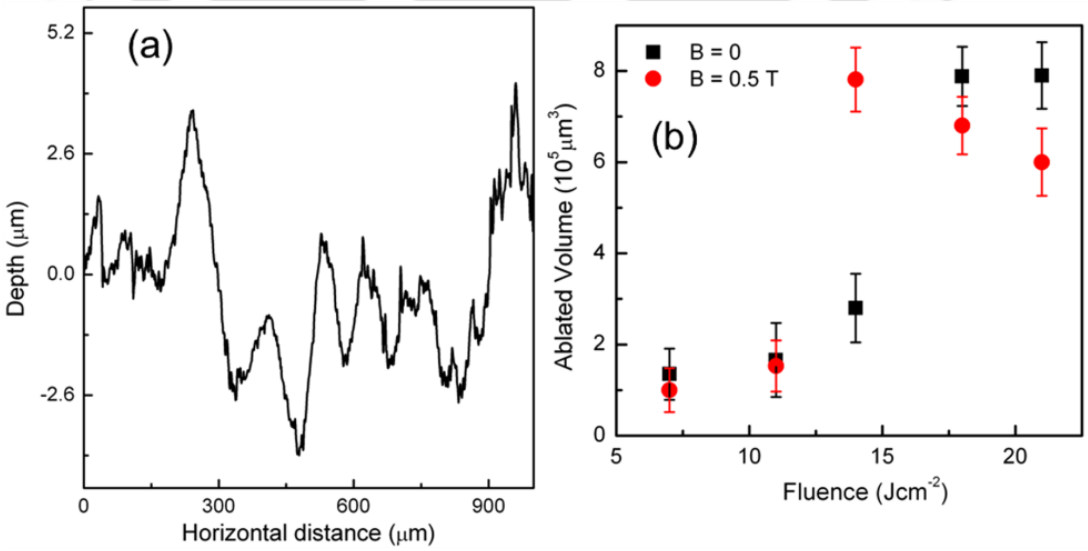


**Fig. 6.7.** (a) Laser induced crater profile at 21 $Jcm^{-2}$ and 0.5 T magnetic field and (b) variation of experimental ablated volume in the absence and presence magnetic field.

Fig. 6.7(a) shows the laser ablated crater profile at 21 $Jcm^{-2}$ in the presence of magnetic field of 0.5 T and Fig. 6.7(b) shows the variation of ablated volume with laser fluence. The ablated volume at lower laser fluence of 7 and 11 $Jcm^{-2}$ is not very significant in the presence of magnetic field. At the laser fluence of 14 $Jcm^{-2}$, the ablated volume increased both in the presence and in absence of magnetic field. However, it increased drastically in the presence of magnetic field. On further increase in laser fluence, the ablated volume was slightly lower than that without magnetic field. The ablated volume in the absence of magnetic field increased drastically when the laser fluence increased from 14 to 18 $Jcm^{-2}$ and then remained constant on further increase in laser fluence. From the crater profile volume, the ablated rate was calculated. In the absence of magnetic field, the ablation rate per 50 shots at 14 $Jcm^{-2}$ was 2.5 $\mu$g and its corresponding value in the presence of magnetic field was 7.0 $\mu$g. The ablation rate in the presence of magnetic field is around 2 times that of without magnetic field. In the presence of magnetic field, the ablation is more pronounced at 14 $Jcm^{-2}$ and it is taken as optimized laser fluence.

## 6.5. Conclusion

FEM was used to simulate laser heating on Cu and Al targets using the 2D heat conduction equation. The vapor pressure in the presence of magnetic field was estimated by adding magnetic pressure term in the Clausius-Clayperon equation. The ablation rate estimated based on this modified equation was found to be in close agreement with that obtained from the experimental results as discussed in chapter 5. The dependence of laser ablation on thermo-physical parameters was also in good

agreement with the experimental results. The ablated volume estimated experimentally was very close to the volume estimated from simulated result. The stopping radius of plasma was also estimated for different LTSD and found to be dependent on it. Therefore the reported model will be very useful to better understand the nanosecond laser ablation and laser plasma in the presence of magnetic field in air.

# Chapter 7

## *Conclusion*

In the present thesis, laser produced Cu plasma in air in the absence and presence of magnetic field was studied using OES. A high power Nd: YAG pulsed laser (operated at 532 nm, 10 Hz repetition rate, and 10 ns pulse duration) was focused onto a copper target to generate LPP in air. LPP expanded in an external magnetic field generated by an electromagnet. The optical emission spectra of Cu were recorded using a monochromator coupled with PMT. The temporal profiles of Cu transitions were recorded using an oscilloscope triggered with the laser pulse. Cu plasma was studied by varying the laser intensity to better understand the effect of laser fluence on LPP in the presence of magnetic field. As most of the previous studies on laser ablation were at fixed magnetic field, therefore, the investigation here was carried out by varying the magnetic field. Laser ablation of Al was also studied along with Cu to compare the dependence of laser ablation on thermo-physical properties of the targets. The properties of the particles deposited on target using IPLD depend on the ambient condition. The post ablation structure of the target was characterized to reveal the role of magnetic field on IPLD. The particles deposited on the Cu target during laser ablation with and without magnetic field were characterized using many techniques such as FESEM, EDX, Optical microscopy, high resolution non-contact surface profilometer, laser Raman spectroscopy, and PL spectroscopy. Since laser ablation is a complex process and therefore, the numerical method is really useful for investigating such complex

process. Simulation on laser ablation of Cu and Al was performed using FEM (ANSYS code) and compared with the experimentally estimated ablation rate.

The first part of the study is the effect of variation of laser fluence on copper plasma at fixed 0.5 T magnetic field. The laser fluence was varied from 7 to 21 $Jcm^{-2}$ in both with and without magnetic field. When the laser fluence was increased from 7 to 18 $Jcm^{-2}$ the electron density increased from $(0.28 \pm 0.09) \times 10^{17}$ to $(1.32 \pm 0.41) \times 10^{17}$ $cm^{-3}$. It increased rapidly to $(3.08 \pm 0.33) \times 10^{17}$ $cm^{-3}$ when the laser fluence was further increased from 18 to 21 $Jcm^{-2}$. Owing to an increase in the laser ablation and ionization with the laser fluence the electron density also increased. In the presence of magnetic field, the electron density was higher than that without magnetic field. It is due to the confinement of plasma. The other possibility is the increase in ionization. The electron density at 14 $Jcm^{-2}$ was 3.5 times higher than in the absence of magnetic field. The electron temperature increased from $(0.87 \pm 0.02)$ to $(0.93 \pm 0.01)$ eV when the laser fluence was increased from 7 to 21 $Jcm^{-2}$ in the absence of the magnetic field. However, in the presence of magnetic field the electron temperature is pronounced due to two possible reasons: (i) Joule's Heating and (ii) adiabatic compression of plasma. In the presence of magnetic field, the intensity of Cu I transitions enhanced with laser fluence and it was found to be dependent on it. The intensity enhancement of Cu I transitions was maximum at 14 $Jcm^{-2}$ at which the electron density and temperature was high. The EF ranged from 1.8 to 2.5 for different transitions. The difference in EF is more likely due to difference in electron impact excitation rate of atom. The weak ionic Cu II transition was also enhanced at 14 $Jcm^{-2}$ in the presence of magnetic field. It is attributed to an increase in the ionization as a result of increase in temperature. The other possibility is the lowering

in ionization potential. The second part of the investigation is the study on the effect of variation of magnetic field on Cu plasma generated at laser fluence of 14 $Jcm^{-2}$ at which the transition lines intensity enhancement was maximum. The electron density and temperature was maximum at 0.3 T. Therefore, the values of optimized laser fluence and magnetic field were taken as 14 $Jcm^{-2}$ and 0.3 T for subsequent studies.

Since, the plasma is highly transient and it also changes with spatial positions Cu plasma was investigated using temporal and spatially-resolved OES. The temporal evolution of the most prominent Cu I transitions (510.5 nm, 515.3 nm, and 521.8 nm) was investigated by varying the strength of magnetic field from 0 to 0.5 T. The Cu I temporal profiles showed multi-components structure. At $B$ = 0 and 0.1 T magnetic field, the temporal profile consisted of only two peaks P1 and P2. However, the increase in magnetic field to 0.3 and 0.5 T resulted in the generation of third component P3. The generation of multi-components is due to the electron impact excitation at a later delay time and it also justified that the collapse of diamagnetic cavity and instability is ruled out for the generation of multi-components in the present work. The integrated intensity of temporal profile showed maximum at 0.3 T which is in good agreement with the results obtained from the time integrated optical emission spectroscopy.

The spatial evolution of Cu plasma along the direction of plasma expansion was investigated by varying $z$ from 0.5 to 6.5 mm from the target surface. In the absence of magnetic field, the electron density varied as $n_e = 9.2z^{-0.33}$ and in the presence of 0.3 T magnetic field, it varied as $n_e = 7.9z^{-0.27}$ which showed that it decayed slowly than without magnetic field. It is attributed to the magnetic

confinement of plasma which decelerates the expansion of the plasma. At larger distance ($z$) from the target, the increase in the electron-ion recombination decreases the electron density. Within $z$ from 4.5 to 6.5 mm, the electron density was more or less the same. The electron temperature near the target was higher. The reason is that the plasma absorbs laser energy during the laser pulse through inverse Bremsstrahlung process near the target surface. Due to the expansion of plasma, the electron temperature decreased with $z$ and it followed the power law. The electron temperature varied as $T_e = 1.1z^{-0.23}$ in the absence of magnetic field whereas it varied as $T_e = 0.9z^{-0.18}$ in the presence of the magnetic field. The adiabatic compression of plasma and Joule's heating led to an increase in the electron temperature. From the spatial evolution of electron density and temperature, the dimension of core of plasma was estimated and was found to increase in the presence of magnetic field. It is more likely due to an increase in electron temperature thereby more ionization occurs in plasma.

The effect of LTSD of plasma in the presence of magnetic field (0.3 T) was also studied. By changing the target position from $d$ = -10 to 10 mm the intensity enhancement was more pronounced at $d$ = 5 mm. The significant enhancement at $d$ = 5 mm is due to non-occurrence of air breakdown resulting in an efficient laser- target interaction which in turn enhanced plasma-magnetic field interaction. The increase in plasma-magnetic field interaction led to more confinement of the plasma. As a result, there was an increase in collisional excitation of the atom and hence the intensity.

In the investigation of laser ablation in the presence of magnetic field, it was observed that the ablated volume/depth was higher in the presence of magnetic field. The study on the effect of variation of magnetic field on laser ablation of Cu and Al

revealed that the laser ablation rate of Al was much higher than that of Cu. It is due to lower melting/vaporization temperature and higher absorption of coefficient of Al for laser wavelength at 532 nm compared with that of Cu. The ablation was mainly due to the melt ejection. The melt ejection was enhanced by an increase in recoil pressure in the presence of magnetic field. The other possibility is the improvement of heat transfer from plasma to target. The increase in melt ejection observed from optical microscopy was supported by the formation of large droplets at the rim of the crater. The XRD characterization of deposited particles on the copper target revealed the formation of $Cu_2O$ nanoparticles. However, in the presence of hot temperature environment of confined plasma, the transformation of $Cu_2O$ to CuO was observed as Cu oxidized to form CuO at high temperature. This observation is also in good agreement with the Raman and PL spectroscopy results.

In order to study the melt ejection, craters were generated on Cu target by impinging 70 laser shots. The cracks formed in the crater surface in the absence of magnetic field were not observed in the presence of magnetic field. It was also observed that the number of droplets generated due to the melt ejection was increased in the presence of magnetic field (uniform and non-uniform magnetic field). The minimum size of droplets generated due to melt ejection and instability was 0.68 $\mu$m. The particles of size less than 0.68 $\mu$m were produced due to the condensation of vaporized mass. The number of droplets of size $\geq$ 0.68 $\mu$m in the presence of non-uniform magnetic field was higher than with uniform magnetic field. In the presence of magnetic field, due to the increase in KH instability, more large droplets were generated. The integrated intensity of Cu I transitions was enhanced more in the presence of uniform magnetic field. The presence of more droplets in the presence of

non-uniform magnetic field caused less laser-matter interaction due to the scattering of laser radiation from the droplets. The low intensity enhancement observed in the presence of non-uniform magnetic field was attributed to the decrease in laser-matter interaction.

In order to better understand the effect of magnetic field on laser ablation it was also simulated using FEM. The simulation was performed by taking two different elements Cu and Al to justify the dependence of laser ablation on thermo-physical parameters. From the simulation it was observed that the presence of magnetic field enhanced the ablation process by increasing the melt ejection. This is due to the fact that the vapor pressure was found to increase in the presence of magnetic field which in turn increased the recoil pressure. A very few studies available in the literature, showed the enhancement of laser ablation in the presence of magnetic field but the detailed process was not discussed. In the present work, the need of modification of Clausisus-Clapeyron equation in the presence of magnetic field was discussed to the best of our knowledge, for the first time and it was modified by adding the magnetic pressure to the ambient air pressure to take into account the effect of magnetic field pressure. The estimated ablation rate based on the modified Clausisus-Clapeyron equation was found to be very close to the experimental results. The ablation was more pronounced in Al due to low melting and vaporization point, and high absorption coefficient which justify the dependent of laser ablation on target properties. The ablated volume estimated from simulation was in good agreement with the experimentally measured value. The stopping radius was also estimated at different lens focusing distance by estimating the ablated mass and expansion kinetic energy of the plasma. The stopping radius was found to be dependent on LTSD.

To sum up, the studies on the temporal evolution of atomic line at variable magnetic field revealed that magnetic field can be used to make laser-produced plasma as a controllable neutral beam source. The spatial resolved OES may be useful in determining the optimized distance from the target surface to enhance the intensity of optical emission spectroscopy and to determine the optimized target-substrate distance in PLD in the presence of magnetic field. The investigations on laser ablation showed that the laser ablation depth can be increased by application of external magnetic field which may be used to improve the aspect ratio in laser micro-machining. It also showed that the morphological structure generated by laser ablation can be altered by application of magnetic field.

**Future Scope of the work**

It is well known that the laser-matter interaction not only depends on the laser laser fluence but it also strongly depends on the laser parameters like wavelength of the incident laser radiation, pulse duration, and repetition rate. Therefore, the present work can be extended to investigate the effect of variation of wavelength of laser radiation on the laser ablation and LPP in the absence and presence of magnetic field. These comparative studies may be useful to better understand the dependence of plasma-magnetic field interaction on the wavelength of the laser. The present work can be employed to study the effect of magnetic field on film deposition using PLD and IPLD, especially, in the presence of high pressure ambient. The present investigations can be used to design the portable LIBS setup to improve the sensitivity of the signal for real world application by using small sized magnetic source like bar magnet. It has been shown in the literature that the dynamical behavior of LPP

generated by ultrafast laser is quite different from that of generated by nanosecond laser. However, the comparative studies on effect of magnetic field on LPP generated by ultrafast and nanosecond laser is not available in the literature and this gap can be investigated using sub-nanosecond and sub-picosecond laser pulses. The FEM simulation can be extended to model the plasma plume expansion in ambient gas in the presence of uniform magnetic field and non-uniform magnetic as well. In this modeling, a set of fluid dynamic equations can be solved using computational fluid dynamics to explore the detailed dynamical behavior of plasma in the magnetic field.

## ***Bibliography***


[1] J.P. Singh. S.N.Thakur, *Laser Induced Breakdown Spectroscopy* (Elsevier, Amsterdam, 2007).

[2] S.B. Ogale, P.G. Bilurkar, N. Mate, S.M. Kanetkar, N. Parikh, and B. Patnaik, J. Appl. Phys. **72**, 3765 (1992).

[3] H. Guo, W. Chen, Y. Shan, W. Wang, Z. Zhang, and J. Jia, Appl. Surf. Sci. **357**, 473 (2015).

[4] J. Hermann, A.L. Thomann, C. Boulmer-Leborgne, B. Dubreuil, M.L. De Giorgi, A. Perrone, A. Luches, and I.N. Mihailescu, J. Appl. Phys. **77**, 2928 (1995).

[5] M.F. Jawad, R.A. Ismail, and K.Z. Yahea, J. Mater. Sci. Mater. Electron. **22**, 1244 (2011).

[6] L. Égerházi, Z. Geretovszky, T. Szörényi, and F. Bari, Appl. Surf. Sci. **257**, 5324 (2011).

[7] L. Egerhazi, Z. Geretovszky, and T. Szorenyi, Appl. Surf. Sci. **247**, 182 (2005).

[8] T. Szorenyi and Z. Geretovszky, Thin Solid Films **484**, 165 (2005).

[9] L. Tunna, W. O'Neill, A. Khan, and C. Sutcliffe, Opt. Lasers Eng. **43**, 937 (2005).

[10] H. Zhang, J. Di, M. Zhou, and Y. Yan, Chinese J. Mech. Eng. **27**, 972 (2014).

[11] C.J. Moorhouse, F.J. Villarreal, H.J. Baker, and D.R. Hall, IEEE Trans. Components Packag. Technol. **30**, 254 (2007).

[12] X.D. Wang, A. Michalowski, D. Walter, S. Sommer, M. Kraus, J.S. Liu, and F. Dausinger, Opt. Laser Technol. **41**, 148 (2009).

[13] D.N. Patel, R.P. Singh, and R.K. Thareja, Appl. Surf. Sci. **288**, 550 (2014).

[14] S. Ibrahimkutty, P. Wagener, T. dos Santos Rolo, D. Karpov, A. Menzel, T. Baumbach, S. Barcikowski, and A. Plech, Sci. Rep. **5**, 16313 (2015).

[15] B. Kumar and R.K. Thareja, Phys. Plasmas **20**, 053503 (2013).

[16] M. Boutinguiza, R. Comesaña, F. Lusquiños, A. Riveiro, J. del Val, and J. Pou, Appl. Surf. Sci. **336**, 108 (2014).

[17] D.N. Patel, P.K. Pandey, and R.K. Thareja, Appl. Opt. **52**, 7592 (2013).

[18] A. Pereira, A. Cros, P. Delaporte, S. Georgiou, A. Manousaki, W. Marine, and M. Sentis, Appl. Phys. A **79**, 1433 (2004).

[19] D.W. Zeng, K.C. Yung, and C.S. Xie, Appl. Surf. Sci. **217**, 170 (2003).

[20] X. Zhou, K. Imasaki, H. Furukawa, H. Umino, K. Sakagishi, S. Nakai, and C. Yamanaka, Surf. Coatings Technol. **137**, 170 (2001).

[21] X. Zhou, K. Imasaki, H. Furukawa, H. Umino, K. Sakagishi, S. Nakai, and C. Yamanaka, Opt. Laser Technol. **33**, 189 (2001).

[22] A. De Giacomo, M. Dell'Aglio, O. De Pascale, R. Gaudiuso, A. Santagata, and R. Teghil, Spectrochim. Acta Part B **63**, 585 (2008).

[23] J.M. Vadillo and J.J. Laserna, Spectrochim. Acta Part B. **59**, 147 (2004).

[24] N.M. Shaikh, S. Hafeez, B. Rashid, and M.A. Baig, Eur. Phys. J. D **44**, 371 (2007).

[25] Z.-X. Lin, L.-M. Liu, and L.-W. Liu, Opt. Laser Technol. **83**, 13 (2016).

[26] M. Akram, S. Bashir, M.S. Rafique, A. Hayat, K. Mahmood, A. Dawood, and M.F. Bashir, Appl. Phys. A **119**, 859 (2015).

[27] M.Z. Butt, D. Ali, M.U. Tanveer, and S. Naseem, Appl. Surf. Sci. **305**, 466 (2014).

[28] D.B. Chrisey and G.K. Hubler, *Pulsed Laser Deposition of Thin Films* (Wiley, New York, 1994).

[29] A. De Giacomo, M. Dell'Aglio, R. Gaudiuso, S. Amoruso, and O. De Pascale, Spectrochim. Acta Part B **78**, 1 (2012).

[30] S.S. Harilal, C. V. Bindhu, M. S. Tillack, F. Najmabadi, and A.C. Gaeris, J. Appl. Phys. **93**, 2380 (2003).

[31] S.S. Harilal, J. Appl. Phys. **102**, 123306 (2007).

[32] X. Li, W. Wei, J. Wu, S. Jia, and A. Qiu, J. Appl. Phys. **113**, 243304 (2013).

[33] R. Fang, D. Zhang, Z. Li, F. Yang, L. Li, X. Tan, and M. Sun, Solid State Commun. **145**, 556 (2008).

[34] A.K. Sharma and R.K. Thareja, Appl. Surf. Sci. **253**, 3113 (2007).

[35] M.A. Hafez, M.A. Khedr, F.F. Elaksher, and Y.E. Gamal, Plasma Sources Sci. Technol. **12**, 185 (2003).

[36] S.S. Harilal, R.W. Coons, P. Hough, and A. Hassanein, Appl. Phys. Lett. **95**, 221501 (2009).

[37] W.Lochte-Holtgreven, *Plasma Diagnostics* (AIP Press, USA, 1995).

[38] G. Cristoforetti, G. Lorenzetti, S. Legnaioli, and V. Palleschi, Spectrochim. Acta Part B **65**, 787 (2010).

[39] Y.I. Lee, K. Song, H.K. Cha, J.M. Lee, M.C. Park, G.H. Lee, and J. Sneddon, Appl. Spectrosc. **51**, 959 (1997).

[40] M.H. Hong, Y.F. Lu, and S.K. Bong, Appl. Surf. Sci. **154**, 196 (2000).

[41] A. De Giacomo, M. Dell'Aglio, O. De Pascale, R. Gaudiuso, V. Palleschi, C. Parigger, and A. Woods, Spectrochim. Acta Part B **100**, 180 (2014).

[42] V.N. Rai, A.K. Rai, F.Y. Yueh, and J.P. Singh, Appl. Opt. **42**, 2085 (2003).

[43] P.K. Pandey and R.K. Thareja, Phys. Plasmas **20**, 022117 (2013).

[44] A. Neogi and R.K.Thareja, Appl. Phys. B **72**, 231 (2001).

[45] S.S. Harilal, M.S. Tillack, B. O'Shay, C. V Bindhu, and F. Najmabadi, Phys. Rev. E **69**, 26413 (2004).

[46] T. Kobayashi, H. Akiyoshi, and M. Tachiki, Appl. Surf. Sci. **197**, 294 (2002).

[47] S.S. Harilal, B. O'Shay, and M.S. Tillack, J. Appl. Phys. **98**, 036102 (2005).

[48] P.K. Pandey and R.K. Tharejaa, Phys. Plasmas **18**, 033505 (2011).

[49] C. Ye, G.J. Cheng, S. Tao, and B.X. Wu, J. Manuf. Sci. Eng. Asme **135**, 061020 (2013).

[50] P.K. Pandey, S.L. Gupta, and R.K. Thareja, Phys. Plasmas **22**, 073301 (2015).

[51] Y. Li, C.H. Hu, H.Z. Zhang, Z.K. Jiang, and Z.S. Li, Appl. Opt. **48**, B105 (2009).

[52] L.B. Guo, W. Hu, B.Y. Zhang, X.N. He, C.M. Li, Y.S. Zhou, Z.X. Cai, X.Y. Zeng, and Y.F. Lu, Opt. Express **19**, 14067 (2011).

[53] X.K. Shen, Y.F. Lu, T. Gebre, H. Ling, and Y.X. Han, J .Appl .Phys. **100**, 053303 (2006).

[54] D.H. Kim, Y.H. Kihm, S.J. Choi, J.J. Choi, and J.J. Yoh, Spectrochim. Acta Part B **110**, 7 (2015).

[55] M.S. Raju, R.K. Singh, P. Gopinath, and A. Kumar, J. Appl. Phys. **116**, 153301 (2014).

[56] N. Behera, R.K. Singh, and A. Kumar, Phys. Lett. A **379**, 2215 (2015).

[57] M.S. Raju, R.K. Singh, A. Kumar, and P. Gopinath, Opt. Lett. **40**, 2185 (2015).

[58] P.K. Pandey and R.K. Thareja, J. Appl. Phys. **109**, 074901 (2011).

[59] D.N. Patel, P.K. Pandey, and R.K. Thareja, Phys. Plasmas **20**, 103503 (2013).

[60] A. Neogi and R.K. Thareja, J. Appl. Phys. **85**, 1131 (1999).

[61] A.N. Mostovych, B.H. Ripin, and J.A. Stamper, Phys. Rev. Lett. **62**, 2837 (1989).

[62] P. Gu, S.B. Liu, S. Liu, and H.-Y. Song, Appl. Surf. Sci. **293**, 80 (2014).

[63] S.S. Harilal, Appl. Surf. Sci. **172**, 103 (2001).

[64] S.S. Harilal, R.C. Issac, C. V. Bindhu, V.P.N. Nampoori, and C.P.G. Vallabhan, J .Appl .Phys. **81**, 3637 (1998).

[65] D. Yadav and R.K. Thareja, Phys. Plasmas **17**, 103104 (2010).

[66] H.C. Joshi, A. Kumar, R.K. Singh, and V. Prahlad, Spectrochim. Acta Part B **65**, 415 (2010).

[67] A. Kumar, H.C. Joshi, V. Prahlad, and R.K. Singh, Phys. Lett. A **374**, 2555 (2010).

[68] A. Kumar, R.K. Singh, and H. Joshi, Spectrochim. Acta Part B **66**, 444 (2011).

[69] R. Qindeel, N.B. Bidin, and Y.M. Daud, J. Phys. Conf. Ser. **142**, 012069 (2008).

[70] R. Qindeel, N. Bidin, R. Zia, and Y.M. Daud, Optoelectron. Adv. Mater. **5**, 331 (2011).

[71] M. Hanif, M. Salik, and M.A. Baig, Opt. Lasers Eng. **49**, 1456 (2011).

[72] D.H. Kim, Y.H. Kihm, S.J. Choi, J.J. Choi, and J.J. Yoh, Spectrochim. Acta Part B **110**, 7 (2015).

[73] A. Alkhawwam, K. Alnama, A. Jazmati, and M.D. Zidan, Opt. Int. J. Light Electron Opt. **125**, 2327 (2014).

[74] W.F. Luo, X.X. Zhao, Q.B. Sun, C.X. Gao, J. Tang, and W. Zhao, Nucl. Instruments Methods Phys. Res. Sect. A Accel. Spectrometers, Detect. Assoc. Equip. **637**, S158 (2011).

[75] N.M. Shaikh, S. Hafeez, M.A. Kalyar, R. Ali, and M.A. Baig, J. Appl. Phys. **104**, 103108 (1 (2008).

[76] J. Aguilera and C. Aragón, Spectrochim. Acta Part B **59**, 1861 (2004).

[77] M. Chen, X. Liu, X. Yang, M. Zhao, Y. Sun, H. Qi, X. Chen, and X. Xu, Phys. Lett. A **372**, 5891 (2008).

[78] A. De Giacomo, V.A. Shakhatov, G.S. Senesi, and S. Orlando, Spectrochim. Acta Part B At. Spectrosc. **56**, 1459 (2001).

[79] R.A. Multari, L.E. Foster, D.A. Cremers, and M.J. Ferris, Appl. Spectrosc. **50**, 1483 (1996).

[80] J.A. Aguilera and C. Aragón, Spectrochim. Acta Part B **63**, 793 (2008).

[81] D. Diego-Vallejo, D. Ashkenasi, and H.J. Eichler, Phys. Procedia **41**, 911 (2013).

[82] J.A. Aguilera, J. Bengoechea, and C. Aragón, Spectrochim. Acta Part B **59**, 461 (2004).

[83] M. Chen, Y.H. Liu, X.D. Liu, and M.W. Zhao, Laser Phys. Lett. **9**, 730 (2012).

[84] P. Schaaf, *Laser Processing of Materials* (Springer, 2010).

[85] N. Nedyalkov, A. Nikolov, P. Atanasov, M. Alexandrov, M. Terakawa, H. Shimizu, Opt. Laser Technol. **64**, 41 (2014).

[86] Y. Jing, H. Wang, J. Zhao, H. Yi, and X. Wang, Appl. Surf. Sci. **347**, 499 (2015).

[87] G. Papadimitropoulos, N. Vourdas, V.E. Vamvakas, D. Davazoglou, J. Phys. Conf. Ser. **10**, 182 (2005).

[88] A.B. Brailovsky, S. V. Gaponov, and V.I. Luchin, Appl. Phys. A Mater. Sci. Process. **61**, 81 (1995).

[89] T. Szörényi and Z. Geretovszky, Thin Solid Films **484**, 165 (2005).

[90] A. Pereira, P. Delaporte, M. Sentis, W. Marine, A.L. Thomann, and C. Boulmer-Leborgne, J. Appl. Phys. **98**, 064902 (2005).

[91] T.H. Kim, S.H. Nam, H.S. Park, J. K. Song, S.M. Parek, Appl. Surf. Sci. **253**, 8054 (2007).

[92] S.S. Harilal, B. O'Shay, and M.S. Tillack, J. Appl. Phys. **98**, 036102 (2005).

[93] O.R. Musaev, E.A. Sutter, J.M. Wrobel, and M.B. Kruger, Appl. Phys. A **122**, 95 (2016).

[94] H.C. Tse, H.C. Man, and T.M. Yue, Opt. Lasers Eng. **32**, 55 (1999).

[95] S. Wolff and I. Saxena, Manuf. Lett. **2**, 54 (2014).

[96] H. Farrokhi, V. Gruzdev, H.Y. Zheng, R.S. Rawat, and W. Zhou, Appl. Phys. Lett. **108**, 254103 (2016).

[97] Y. Lu, G.F. Sun, D.P. Wen, Y.K. Zhang, and A.X. Feng, Int. J. Adv. Manuf. Technol. **84**, 2293 (2015).

[98] C.C. Ho, G.R. Tseng, Y.J. Chang, J.C. Hsu, and C.L. Kuo, Int. J. Adv. Manuf. Technol. **73**, 329 (2014).

[99] Y.J. Chang, C.L. Kuo, and N.Y. Wang, J. Laser Micro Nanoeng. **7**, 254 (2012).

[100] J.. Conde, F. Lusquiños, P. González, J. Serra, B. León, A. Dima, L. Cultrera, D. Guido, A. Zocco, and A. Perrone, Thin Solid Films **453**, 323 (2004).

[101] V. Oliveira, R. Colaço, and R. Vilar, Appl. Surf. Sci. **253**, 7585 (2007).

[102] J. H. Lau and R. S. Lee, *Microvias for Low Cost, High Density Interconnects* (McGraw-Hill, New York, 2001).

[103] A.S. Mahmood, K. Venkatakrishnan, and B. Tan, Nanoscale Res. Lett. **8**, 477

(2013).

[104] J.S. Sekhon, in *Renew. Energy Environ.* (OSA, Washington, D.C., 2011), p. JWE22.

[105] K. Suzuki, N. Tanaka, A. Ando, and H. Takagi, J. Nanoparticle Res. **14**, 863 (2012).

[106] J.A. Aguilera and C. Aragón, Spectrochim. Acta Part B **97**, 86 (2014).

[107] R.K. Thareja and A.K. Sharma, Laser Part. Beams **24**, 311 (2006).

[108] D. Devaux, R. Fabbro, L. Tollier, and E. Bartnicki, J. Appl. Phys. **74**, 2268 (1993).

[109] J.D. Hey, J. Quant. Spectrosc. Radiat. Transf. **16**, 69 (1976).

[110] H.J. Kunze, *Introduction to Plasma Spectroscopy* (Springer, Heidelberg, 2009).

[111] A.K. Sharma and R.K.Thareja, Appl. Surf. Sci. **243**, 68 (2005).

[112] J.H. Yoo, S.H. Jeong, X.L. Mao, R. Greif, and R.E. Russo, Appl. Phys. Lett. **76**, 783 (2000).

[113] R. Kelly and J.E. Rothenberg, Nucl. Instruments Methods Phys. Res. Sect. B Beam Interact. with Mater. Atoms **7-8**, 755 (1985).

[114] K.S. Singh and A.K. Sharma, J. Appl. Phys. **119**, 183301 (2016).

[115] R. Hergenröder, Spectrochim. Acta Part B **61**, 284 (2006).

[116] D. Bauerle, *Laser Processing and Chemistry* (Springer - Verlag, Berlin, 2000).

[117] C. Illgner, P. Schaaf, K.P. Lieb, R. Queitsch, and J. Barnikel, J. Appl. Phys. **83**, 2907 (1998).

[118] R. Hergenröder, J. Anal. At. Spectrom. **21**, 517 (2006).

[119] H.R. Griem, *Plasma Spectroscopy* (McGraw Hill Book Company, USA, 1964).

[120] G. Cristoforetti, A. De Giacomo, M. Dell'Aglio, S. Legnaioli, E. Tognoni, V. Palleschi, and N. Omenetto, Spectrochim. Acta Part B **65**, 86 (2010).

[121] H.R. Griem, Phys. Rev. **131**, 1170 (1963).

[122] P.K. Diwakar, S.S. Harilal, J.R. Freeman, and A. Hassanein, Spectrochim. Acta - Part B **87**, 65 (2013).

[123] Z. Wang, T.B. Yuan, S.L. Lui, Z.Y. Hou, X.W. Li, Z. Li, and W.D. Ni, Front. Phys. **7**, 708 (2012).

[124] www.nist.gov. for NIST Atomic Spectra Database (version 5).

[125] B. Zmerli, N. Ben Nessib, M.S. Dimitrijevic, and S. Sahal-Brechot, Phys. Scr. **82**, 055301 (2010).

[126] K.S. Singh. and A.K. Sharma, Phys. Plasmas **23**, 013304 (2016).

[127] A.H. Galmed and M.A. Harith, Appl. Phys. B **91**, 651 (2008).

[128] N. Konjevic, Phys.Rep. **316**, 339 (1999).

[129] B.Y. Man, Q.L. Dong, A.H. Liu, X.Q. Wei, Q.G. Zhang, J.L. He, and X.T. Wang, J. Opt. A Pure Appl. Opt. **6**, 17 (2004).

[130] E. Gudimenko, V. Milosavljević, and S. Daniels, Opt. Express **20**, 12699 (2012).

[131] J.A. Bittencourt, *Fundamentals of Plasma Physics* (Springer, New York, 2004).

[132] K.S. Singh and A.K. Sharma, Phys. Plasmas **23**, 122104 (2016).

[133] I.I. Beilis, Appl. Phys. Lett. **89**, 091503 (2006).

[134] B.Cullity, *Elements of X-Ray Diffraction* (Addison-Wesley Publishing Company, 1956).

[135] S. Moaveni, *Finite Element Analysis Theory And Application With ANSYS* (2011).

[136] D. Marla, U. V. Bhandarkar, and S.S. Joshi, J. Appl. Phys. **109**, 021101 (2011).

[137] F.P. Mezzapesa, L.L. Columbo, M. Brambilla, M. Dabbicco, A. Ancona, T. Sibillano, and G. Scamarcio, Appl. Phys. Lett. **101**, 011103 (2012).

[138] M.V. Allmen, *Laser Beam Interactions with Materials* (Springer-Verlag Heidelberg, 1987).

[139] J. Gold, B. Kasemo, D. Chakarov, and H. Reimers, Appl. Phys. A Mater. Sci. Process. **77**, 491 (2003).

[140] K.S. Singh and A.K. Sharma, J. Appl. Phys. **119**, 183301 (2016).

[141] A.K. Aitoumeziane, A. Sari, B. Liani, and J.-D. Parisse, J. Opt. Soc. Am. B **31**, 53 (2013).

[142] N.A. Vasantgadkar, U. V. Bhandarkar, and S.S. Joshi, Thin Solid Films **519**, 1421 (2010).

[143]www.ansys.stuba.sk/html/realtoc.html. in (2009).

[144] www.cfa.harvard.edu. for Atomic spectral line database from CD-ROM 23 of R. L. Kurucz.

[145] G. Ecker and W. Kröll, Phys. Fluids **8**, 354 (1965).

[146] A. Neogi, V. Narayanan, and R.K. Thareja, Phys. Lett. A **258**, 135 (1999).

[147] S.S. Harilal, C.V. Bindhu, V.P.N. Nampoori, and C.P.G. Vallabhan, Appl. Phys. Lett. **72**, 167 (1998).

[148] X. Xu, Appl. Surf. Sci. **197**, 61 (2002).

[149] F. F.Chen, *Introduction to Plasma Physics and Controlled Fusion* (Springer, New York, 2011).

[150] R.K. Singh, A. Kumar, B.G. Patel, and K.P. Subramanian, J. Appl. Phys. **101**, 103301 (2007).

[151] M. VanZeeland and W. Gekelman, Phys. Plasmas **11**, 320 (2004).

[152] M. VanZeeland, W. Gekelman, S. Vincena, and G. Dimonte, Phys. Rev. Lett. **87**, 105001 (2001).

[153] B.H. Ripin, J.D. Huba, E.A. McLean, C.K. Manka, T. Peyser, H.R. Burris, and J. Grun, Phys. Fluids B Plasma Phys. **5**, 3491 (1993).

[154] H.C. Pant, V.N. Rai, and M. Shukla, Phys. Scr. **T75**, 104 (1998).

[155] A. Neogi and R.K. Thareja, Phys. Plasmas **6**, 365 (1999).

[156] B. Ripin, E. McLean, C. Manka, C. Pawley, J. Stamper, T. Peyser, A. Mostovych, J. Grun, A. Hassam, and J. Huba, Phys. Rev. Lett. **59**, 2299 (1987).

[157] A. Kumar, S. George, R.K. Singh, H. Joshi, and V.P.N. Nampoori, Laser Part. Beams **29**, 241 (2011).

[158] J. Grun, M. Emery, C. Manka, T. Lee, E. Mclean, A. Mostovych, J. Stamper, S. Bodner, S. Obenschain, and B. Ripin, Phys. Rev. Lett. **58**, 2672 (1987).

[159] V.N. Rai, M. Shukla, and H.C. Pant, Pramana **55**, 773 (2000).

[160] T.A. Peyser, C.K. Manka, B.H. Ripin, and G. Ganguli, Phys. Fluids B Plasma Phys. **4**, 2448 (1992).

[161] R. Kumar, R.K. Singh, and A. Kumar, Phys. Lett. A **377**, 93 (2012).

[162] A.A. Harms, D.R. Kingdon. K. F. Schoepf, and G. H. Miley, *Principles of Fusion Energy* (World Scientific, Singapore, 2000).

[163] R. Kumar, R.K. Singh, and A. Kumar, Phys. Lett. A **377**, 93 (2012).

[164] J.D. Wu, Q. Pan, and S.C. Chen, Appl. Spectrosc. **51**, 883 (1997).

[165] L.M. Cabalin and J.J. Laserna, Spectrochim. Acta Part B **53**, 723 (1998).

[166] N.M. Shaikh, B. Rashid, S. Hafeez, Y. Jamil, and M.A. Baig, J. Phys. D. Appl. Phys. **39**, 1384 (2006).

[167] N.M. Shaikh, B. Rashid, S. Hafeez, S. Mahmood, M. Saleem, and M.A. Baig, J

.Appl .Phys. **100**, 073102 (2006).

[168] S. Sudo, T. Sekiguchi, and K.N. Sato, J. Phys. D. Appl. Phys. **11**, 389 (1978).

[169] A. Bogaerts, R. Gijbels, and R.J. Carman, Spectrochim. Acta Part B **53**, 1679 (1998).

[170] V. Bulatov, L. Xu, and I. Schechter, Anal. Chem. **68**, 2966 (1996).

[171] E. Schwarz, S. Gross, B. Fischer, I. Muri, J. Tauer, H. Kofler, and E. Wintner, Laser Part. Beams **28**, 109 119 (2010).

[172] J. Grun, R. Stellingwerf, and B.H. Ripin, Phys. Fluids **29**, 3390 (1986).

[173] L.M. Cabalín, D. Romero, J.M. Baena, and J.J. Laserna, Fresenius. J. Anal. Chem. **365**, 404 (1999).

[174] Z.H. Shen, S.Y. Zhang, J. Lu, and X.W. Ni, Opt. Laser Technol. **33**, 533 (2001).

[175] J.M. Fishburn, M.J. Withford, D.W. Coutts, and J.A. Piper, Appl. Surf. Sci. **252**, 5182 (2006).

[176] M. Bass, M.A. Nassar, and R.T. Swimm, J. Appl. Phys. **61**, 1137 (1987).

[177] A.B. Gojani, J.J. Yoh, and J.H. Yoo, Appl. Surf. Sci. **255**, 2777 (2008).

[178] J.H. Yoo, S.H. Jeong, R. Greif, and R.E. Russo, J. Appl. Phys. **88**, 1638 (2000).

[179] Y.T. Lee and R.M. More, Phys. Fluids **27**, 1273 (1984).

[180] X. Zhang, S.S. Chu, J.R. Ho, and C.P. Grigoropoulos, Appl. Phys. A Mater. Sci. Process. **64**, 545 (1997).

[181] A.M. Turdukozhaeva, Russ. J. Phys. Chem. A **86**, 702 (2012).

[182] R. Qindeel, N. B. Bidin, and Y. M. Daud, J. Phys. Conf. Ser. **142**, 012069 (2008).

[183] T. Szorenyi and Z. Geretovszky, Thin Solid Films **453**, 431 (2004).

[184] M. Rashad, M. Rüsing, G. Berth, K. Lischka, and A. Pawlis, J. Nanomater. **2013**, 714853 (1 (2013).

[185] K. Muthe, J.Vyas, S.N. Narang, D. Aswal, S. Gupta, D. Bhattacharya, R. Pinto, G. Kothiyal, and S. Sabharwal, Thin Solid Films **324**, 37 (1998).

[186] Y.I. Lee, K. Song, H.K. Cha, J.M. Lee, M.C. Park, G.H. Lee, and J. Sneddon, Appl. Spectrosc. **51**, 959 (1997).

[187] A. Misra, A. Mitra, and R.K. Thareja, Appl. Phys. Lett. **74**, 929 (1999).

[188] K. Mageshwari and R. Sathyamoorthy, J. Mater. Sci. Technol. **29**, 909 (2013).

[189] Y. Mao, J. He, X. Sun, W. Li, X. Lu, J. Gan, Z. Liu, L. Gong, J. Chen, P. Liu, and

Y. Tong, Electrochim. Acta **62**, 1 (2012).

[190] S.S. Chang, H.J. Lee, and H.J. Park, Ceram. Int. **31**, 411 (2005).

[191] S S. Shanmugan and D. Mutharasu, in *IEEE-ICSE2012 Proc.* (2012), p. 132.

[192] I.N. Mihailescu, E. Gyorgy, V.S. Teodorescu, G. Steinbrecher, J. Neamtu, A. Perrone, and A. Luches, J. Appl. Phys. **86**, 7123 (1999).

[193] N.T. Goodfriend, S. V. Starinskiy, O.A. Nerushev, N.M. Bulgakova, A. V. Bulgakov, and E.E.B. Campbell, Appl. Phys. A **122**, 154 (2016).

[194] L.K. Ang, Y.Y. Lau, R.M. Gilgenbach, H.L. Spindler, J.S. Lash, and S.D. Kovaleski, J. Appl. Phys. **83**, 4466 (1998).

[195] A. Bhaumik, A. Haque, P. Karnati, M.F.N. Taufique, R. Patel, and K. Ghosh, Thin Solid Films **572**, 126 (2014).

[196] V.Y. Chekhovskoi, V.D. Tarasov, and Y. V. Gusev, High Temp. **38**, 394 (2007).

[197] M. Stafe, C. Negutu, and I.M. Popescu, Appl. Surf. Sci. **253**, 6353 (2007).

## ***List of Publications***

### (a) Peer reviewed Journals (Published)

1. **Khwairakpam Shantakumar Singh**, Alika Khare, and Ashwini Kumar Sharma *"Effect of uniform magnetic field on laser-produced Cu plasma and the deposited particles on the target surface"* Laser Part. Beams **35,** 352 (2017)

2. **Khwairakpam Shantakumar Singh** and Ashwini Kumar Sharma *"Time-integrated optical emission studies on laser-produced copper plasma in the presence of magnetic field in air ambient at atmospheric pressure"* Appl. Phys. A **123**, 325 (2017).

3. **Khwairakpam Shantakumar Singh** and Ashwini Kumar Sharma "*Melt ejection from copper target in air in the presence of magnetic field using nanosecond pulsed laser ablation*." J. Vac. Sci. Technol. A **35**, 031305 (2017)

4. **Khwairakpam Shantakumar Singh** and Ashwini Kumar Sharma *"Effect of lens focusing distance on laser-produced copper plasma in air in the presence of static transverse magnetic field."* Phys. Plasmas **23**, 123514 (2016).

5. **Khwairakpam Shantakumar Singh** and Ashwini Kumar Sharma "*Spatially-resolved behavior of laser-produced copper plasma along expansion direction in the presence of static uniform magnetic field*." Phys. Plasmas **23**, 122104 (2016).

6. **Khwairakpam Shantakumar Singh** and Ashwini Kumar Sharma "*Effect of variation of magnetic field on laser ablation depth of copper and aluminum targets in air atmosphere*" J. Appl. Phys. **119**, 183301 (2016).

7. **Khwairakpam Shantakumar Singh** and Ashwini Kumar Sharma "*Multi-structured temporal behaviour of neutral copper transitions in laser-produced*

*plasma in the presence of variable transverse static magnetic field"* Phys. Plasmas **23**, 013304 (2016).

**(b) <u>Under preparation</u>**

1. **Khwairakpam Shantakumar Singh** and Ashwini Kumar Sharma "*Simulation on laser ablation of copper in the presence of magnetic field in air at atmospheric pressure*", ms under preparation

2. **Khwairakpam Shantakumar Singh** and Ashwini Kumar Sharma, "*Stark width measurement of copper atomic lines in the presence of the magnetic field using optical emission spectroscopy*" ms under preparation

**<u>Conference/workshop/School Attended</u>**

**(a) <u>International conferences</u>**

1. **Kh Shantakumar Singh** and Ashwini Kumar Sharma *"Effect of magnetic field on laser ablation during plasma formation: Experimental and finite element model study"***,** XXVII IUPAP Conference on Computational Physics (2015), IIT Guwahati.

2. **Kh Shantakumar Singh** and Ashwini Kumar Sharma *"Nanostructuring on copper target surface via pulsed laser ablation in the presence and absence of magnetic field in air"*, 4th International Conference on Advanced Nanomaterial and Nanotechnology (ICANN), 8 - 11th Dec, 2015, IIT Guwahati

3. **Kh Shantakumar Singh** and Ashwini Kumar Sharma *"Effect of uniform magnetic field on nanostructuring by laser ablation of copper at atmospheric pressure"*, 4$^{th}$ International conference on current Developments in atomic, molecular, optical and nano-physics with applications, (CDAMOP), 2015, DRDO and Delhi University, Delhi.

4. **Kh Shantakumar Singh** and Ashwini Kumar Sharma *"Effect of uniform transverse magnetic field on the life-time of laser- produced copper plasma")*, 29th National Symposium on plasma science and technology & International conference on plasma and nanotechnology, 2014, PSSI and M.K. University, Kottayam.

5. Prahlad K. Baruah, **Kh Shantakumar Singh**, Ashwini K. Sharma, and Alika Khare *"Effect of laser energy on nanoparticles produced by laser ablation of copper in distilled water"*, 29th National Symposium on plasma science and technology & International conference on plasma and nanotechnology, 2014, PSSI and M. K. University, Kottayam.

6. Sanasam Sunderlal Singh**, Kh. Shantakumar**, Alika Khare and S.N. Joshi *"Fabrication of micro-channels on mild steel using laser induced micro-machining"* 5th International & 26th All India Manufacturing Technology, Design and Research Conference (AIMTDR 2014) December 12th–14th, 2014, IIT Guwahati.

**(b) <u>National conferences</u>**

1. **Kh Shantakumar Singh** and Ashwini Kumar Sharma *"A 2D finite element model to simulate temperature field and ablation depth during laser ablation"* 2nd National symposium on non-linear and complex phenomena, 2015, CPP-IPR, ACNCP and IASST, Guwahati.

2. **Kh Shantakumar Singh** and Ashwini Kumar Sharma*"Laser ablation depth enhancement of copper in the presence of external magnetic field"* DAE-BRNS National Laser Symposium-24, 2015, ILA and RRCAT, Indore.

3. **Kh Shantakumar Singh** and Ashwini Kumar Sharma *"Effect of laser focusing distance on laser – produced copper plasma in the absence and presence of uniform transverse magnetic field",* 30th National Symposium on plasma science and technology, 1-4 December, 2015 PSSI and SINP, Kolkata

4. **Kh Shantakumar Singh**, Eshita Mal, Alika Khare and Ashwini Kumar Sharma "*Laser-induced breakdown spectroscopy (LIBS): principle, instrumentation, and applications"*, TEQIP symposium to celebrate the 2015 International year of light, IIT Guwahati.

5. Sanasam Sunderlal Singh, **Kh Shantakumar**, Prahlad Kr Baruah, A K Sharma, S N Joshi, Alika Khare "*Laser micromachining of 316L stainless steel"* TEQIP symposium to celebrate the 2015 International year of light, IIT Guwahati.

6. Eshita Mal, **Kh. Shantakumar Singh**, Prahlad K.Baruah, Arjun Biswas, Ashwini Kumar Sharma and Alika Khare *" Characterization of Copper Plasma using Laser Induced Breakdown Spectroscopy in air*", 4th PSSI Plasma Scholar's Colloqium 2015, Jadavpur University, Jadavpur

7. **Kh. Shantakumar Singh**, Prahlad K. Baruah and Ashwini K. Sharma *"Spectroscopic studies on laser induced copper plasma in presence of external magnetic field"*, DAE-BRNS National Laser Symposium-22, 2014, ILA and MIT, Manipal

8. **Kh. Shantakumar Singh**, Alika Khare and Ashwini Kumar Sharma, *"Spectroscopic study of laser-produced copper plasma in uniform magnetic field"* DAE-BRNS National Laser Symposium-23, 2014, ILA and S.V. University, Tirupati

9. **Kh. Shantakumar Singh**, Prahlad Kumar Baruah, Eshita Mal, Alika Khare and Ashwini Kumar Sharma *"Effect of uniform magnetic field on laser ablation"*, DAE-BRNS National Laser Symposium-23, 2014, ILA and S.V. University, Tirupati

10. **Kh. Shantakumar Singh** and Ashwini K. Sharma *"Measurement of Stark width in laser produced copper plasma in the presence of magnetic field"*, 28th National Symposium on Plasma Science & Technology, Plasma 2013, PSSI & KIIT university, Bhubneswar

11. A. T. T. Mostako, G. P. Bharti, **Kh. Shantakumar Singh**, A. K. Sharma and Alika Khare *Determination of Electron Density in Laser Induced Molybdenum Plasma"* (Oral), 27th National Conference on Plasma Science & Technology (Plasma-2012), Pondicherry University, Puducherry.

**(c) <u>Workshop/ School attended</u>**

1. *"Computational Technique in Physics"* QIP, Department of Physics, IIT Guwahati (2013)
2. " *MATLAB workshop*" IEEE Student branch, IIT Guwahati (2013)
3. " *Compressive Sensing and Technical Writing*" IEEE Student branch, IIT Guwahati (2013)
4. " *IVCr workshop on X-ray diffraction systems and related applications*", PANalytical and Department of Mechanical Engineering, IIT Guwahati (2014)
5. *"Laser produced plasmas: Physics and Applications"* 4th SERC (Science and engineering council) school (2012), RRCAT, Indore
6. "Research conclave-2015 and 2016" *organized by PhD council IIT Guwahati*
7. "Departmental Day – 2016" *organized by Department of Physics, IIT Guwahati*
8. "Science Exhibition on National Science Day-2015" *organized by IASST and Cotton college, Guwahati*